Modeling and Control of Transient Mixing Flow for Direct Ink Write Additive Manufacturing

by

Matthew Hildner

A dissertation submitted in partial fulfillment
of the requirements for the degree of
Doctor of Philosophy
(Mechanical Engineering)
in the University of Michigan
2021

Doctoral Committee:

Professor Albert Shih, Chair
Assistant Professor Nima Fazeli
Research Investigator Miguel A. Funes-Lora
Professor Ronald G. Larson
Dr. Bizhong Zhu, Dow Chemical Company

Matthew Hildner

mhildner@umich.edu

ORCID iD: 0000-0003-0845-2311

Dedication

I would like to thank my parents, fiancé Megan, brothers, and my extended family for their support and love over the years. Without them I would not have had the passion or ability to continue my academic education.

I would like to thank my lab mates, Christian Argenti, Dian-Ru Li, James Lorenz, Jeffrey Plott, Jingxuan Lyu, Ketut Priambada, Lei Chen, Miguel Angel Funes Lora, Robert Chisena, Tianshu Dong, William Van den Bogert, Yang Liu, and Yihao Zhen for the help and support that they have provided to me throughout my time at Michigan.

I would like to thank my undergraduate student, James Lorenz, for his help in my research. Many printing improvements and experimental results came from his efforts on this project.

I would like to thank my committee members, Professor Ronald G. Larson, Professor Nima Fazeli, Dr. Bizhong Zhu, and Dr. Miguel A. Funes-Lora. Each member worked with me to improve and refine my research topic, and I am grateful for the insights they have provided to me.

I would like to thank all the Mechanical Engineering faculty that I have interacted with and that have made my education at the University of Michigan a wonderful experience.

I would like to thank the Mechanical Engineering admin and financial staff who worked with me to get all the random materials, equipment, and “stuff” I needed for my research.

Finally, I would like to thank my advisor Professor Albert Shih for his guidance and support through my entire PhD journey. He is tireless in his efforts to support all his students throughout their time at Michigan and he never stops pushing them to improve. When we first met, I was a new graduate student looking for some advice, after three minutes he had convinced me to double my class load and to work in his lab. This first encounter then led to countless late night paper revisions, discussions about football, discussions about 3D printing, and more. Professor Shih has pushed me to improve myself and learn as much as I can in ways, I never thought possible. I hope that in the future I can give others half the dedication and help he has given me.

Acknowledgements

I would like to thank Glenn Gordon, James Casey, and Stanley Yee from Dow inc for their support in this research. Glenn Gordon provided the rheological data for the alkoxysilicone used in Chapters 2, 3, and 4. James Casey provided the acoustic wave speed data for the alkoxysilicone used in Chapters 3 and 4. Stanley Yee provided the alkoxysilicone used in all experiments performed in Chapters 2, 3, and 4.

I would like to thank Xing Tian for providing the progressive cavity pump used in Chapter 2.

Table of Contents

List of Tables

List of Figures

Nomenclature

Symbol	Meaning
A	Cross sectional area
a	Acoustic wave speed
$\boldsymbol{a_c}$	Cartesian acceleration vector
$\boldsymbol{a_e}$	Extrusion acceleration vector
a_g	Gompertz asymptote
b	Width of bulge in U-turn
b_g	Gompertz displacement
C_x	Corner swell X deviation
C_y	Corner swell Y deviation
$CoVr$	Coefficient of variation
c_g	Gompertz growth rate
D	Pipe diameter
D_{exp}	Experimental corner swell
D_h	Hydraulic diameter
D_{in}	Inlet diameter
D_{out}	Outlet diameter
D_{swell}	Corner swell diameter
D_{taper}	Taper diameter
E	Extrusion axis
E_y	Youngs modulus
e	Pipe wall thickness
F	Frictional term
f	Darcy friction factor
f_{mod}	Modified darcy friction factor
$\boldsymbol{G}$	iLQR error factor matrix
G'	Shear rate
g	Gravity
h	Layer height
$\boldsymbol{I}$	Identify matrix
J	Jerk in the Cartesian coordinate
J_e	Jerk in the extrusion coordinate
K	Bulk modulus
K_G	Shear parameter
K_i	Blending parameter
K_l	Length parameter

Symbol	Meaning
k	Fluid consistency index
L	Total length
L_{taper}	Total length of tapered nozzle
l	Steady-state length
l_h	Helix length
n	Flow behavior index
P	Pressure
P_c	Cross-sectional perimeter
$\boldsymbol{P_r}$	Input pressure vector
P_{pipe}	Pipe pressure
P_{sm}	Static mixer pressure
P_{taper}	Tapered pipe pressure
$\boldsymbol{p}$	Point
p_h	Helix pitch
Q	Volumetric flowrate
$\boldsymbol{Q_c}$	Control flowrate vector
$\boldsymbol{Q_e}$	Flowrate error vector
$\boldsymbol{Q_m}$	Machine learning model flowrate vector
$\boldsymbol{Q_r}$	Reference flowrate vector
$\boldsymbol{Q_o}$	Output flowrate vector
$\boldsymbol{S}$	Tool path segment
$\boldsymbol{S_c}$	Cartesian segment
S_e	Extrusion path segment
$\dot{\boldsymbol{S}}_{\boldsymbol{c}}$	Cartesian segment velocity
$\dot{\boldsymbol{S}}_{\boldsymbol{e}}$	Extrusion segment velocity
T	Total time to traverse a tool path segment
t	Time
t_f	Feedforward time
t_r	Helix thickness
t_r	Step response time
u	Fluid velocity
$\boldsymbol{R}$	iLQR control factor matrix
$\boldsymbol{v}$	Cartesian velocity target
$\boldsymbol{v_c}$	Cartesian velocity target
$\boldsymbol{v_e}$	Extrusion velocity target
w	DIW line width
X	X axis
x	Location on a central axis in fluid model
Y	Y axis
Z	Z axis
Δt	Timestep
Δx	Length step
α	Taper angle

Symbol	Meaning
β	Release angle
γ	Attack angle
ρ	Density
$\boldsymbol{\Lambda}$	Cartesian objective value
$\boldsymbol{\Lambda_e}$	Extrusion objective value
λ	FECC segmentation length
μ	Viscosity
μ_{eff}	Effective viscosity
ν	Poisson ratio
$\boldsymbol{\Upsilon}$	Tool path
$\boldsymbol{\Upsilon_{new}}$	New tool path
φ	Pipe parameter

Abstract

Direct ink write (DIW) additive manufacturing (AM) is a material extrusion process characterized by depositing viscous liquids through fine nozzle tips. The process is used to make three-dimensional objects with a wide range of materials. In this dissertation, a new impeller spiral static mixer (SSM) is designed and tested, and a transient fluid model and control method for DIW of two-part silicone with mixing is developed.

An important aspect of the DIW of two-part silicone is in-situ mixing using static mixing, that enables continuous printing mixed silicone. A new SSM design, called the Impeller SSM (ISSM), inspired by centrifugal pump impeller blades and fabricated by AM is presented. The pressure drop reduction and mixing of an ISSM is compared to the standard SSM, both are measured experimentally and validated by computational fluid dynamics analysis. Compared to a standard SSM of the same size, the ISSM demonstrated a pressure drop and power reduction up to 18.2%. Experimental results also show the ability of AM to fabricate the custom ISSM without using costly fabrication techniques.

Using an understanding of the in-situ mixing from the ISSM, the transient flow inside a DIW system is characterized using the continuity and momentum equations. New frictional models describing fluid flow for a viscous non-Newtonian fluid through the combined ISSM and tapered nozzle are created for the momentum equation. The continuity and momentum equations describing a DIW system are numerically solved using the CM. The transient response of the DIW output volumetric flowrate in the CM model is validated using a doppler volumetric flow

sensor and two pressure sensors. CM is also used to predict the corner swelling of a 90-degree corner DIW tool path with accelerations of 100, 250, 500, 1000, 1500, and 2000 mm/s^2. The predicted corner swelling is matched with the actual corner swelling found using image processing of a 90-degree corner. Across the tested accelerations the corner swell ranged from 0.76 to 0.37 mm, matching CM predictions. Demonstrating that the CM can accurately predict the transient response of the DIW volumetric flowrate.

With the validated CM model, the transient fluid deposition for DIW is controlled using feedforward error correction control (FECC). FECC combines the trapezoidal motion planning, CM, machine learning, and iterative linear quadratic regulator (iLQR) controller to create new extrusion flow paths to improve the deposition accuracy for DIW. FECC is applied to two tool paths: a 90-degree corner and a U-turn. With FECC, the 2-norm error between the output volumetric flow rate and desired volumetric flow rate of the 90-degree turn is reduced from 0.32 to 0.16 mL/min, while the measured size of the 90-degree corner swell was reduced from 0.63±0.03 mm to 0.48±0.03 mm. For the U-turn, the 2-norm error between the output volumetric flow rate and desired volumetric flow rate is reduced from 0.43 to 0.18 mL/min and the measured width was reduced from 0.98±0.04 mm to 0.82±0.03 mm. The total reduction in the deposition error was 25-40%. The FECC tool paths were used with a test part containing 5000 90-degree turns and 8500 U-turns. With FECC, the test part had significant improvements to reduce bulging at the corners, material build up at the edges of infill, and gaps in the infill. This study demonstrates that FECC can correct errors in DIW deposition and be applied to improve the part quality.

Chapter 1. Introduction

Material extrusion (MEX) is a type of additive manufacturing (AM) defined by ASTM as a process where the material is selectively dispensed through a nozzle or orifice and is one of the most common forms of AM [1,2]. Direct ink write (DIW) is a type of MEX characterized by depositing a viscous liquid through a fine nozzle to 3D-print shapes layer-by-layer [3]. DIW can use a wide range of materials, including silicones, epoxies, urethanes, bio-inks, and ceramic pastes to produce AM parts [4–9]. MEX machines typically consist of a gantry system that moves a print head with a fine tip nozzle delivering high-viscosity fluid line-by-line and layer-by-layer on a build plate [10]. For DIW, there are two main types of extrusion systems used to deposit viscous liquid: syringes and positive displacement pumps (PDP). Syringes use a plunger driven by pneumatics or pistons to force the viscous fluid through a fine tip nozzle [11]. PDPs use fixed cavities to transform a motor or piston's cyclic motion into a precise volumetric flow and are preferred for accurate delivery of the fluid at desired locations [12–14].

In 2004 the first major DIW paper was published by Lewis and Gratson, though earlier examples of DIW can be traced back to the 1990's [3,15]. Despite almost two decades of research there are significant gaps in how the mechanics 3D printing with fluids works[15]. When developing a DIW process, the current best practice is to determine printing parameters using experimental trial and error [15–19]. Some limited examples of work developing an analytical methodology to DIW parameter generation can be seen in Plott et al. [20] and Yuk and Zhao [16]. Plott et al. [20] conducted experiments designed to measure the forces applied during

DIW, quantify their effect, and relate them to volumetric flowrate, print height, and layer width. The results showed that forces created by DIW are dependent on the interaction between the printing material and nozzle. Using these insights Plott et al. demonstrated how tall objects could be printed by minimizing tangential forces [20]. Yuk and Zhao [16] demonstrated how there are multiple behaviors of viscoelastic materials being deposited during DIW based on the ratio of nozzle speed, print height, and volumetric flow rate. With a normalized print height and print speed Yuk and Zhao [16] were able to predict the shape viscoelastic materials will take during deposition.

This dissertation will focus on another problem that affects DIW, transient fluid flow. The extrusion nozzle movement used to build the DIW parts can be split into two phases; 1) steady-state: when the extrusion nozzle is moved at a constant velocity, and 2) transient state: when the extrusion nozzle is experiencing acceleration or deceleration [10]. During the steady-state, the volumetric flowrate of syringes and PDPs can be finely controlled through pressure or pump speed adjustments respectively, to achieve the desired deposition rate [21]. During the transient state, material extrusion is nonlinear and cannot be assumed to match the gantry dynamics using linear control [22]. As a result, geometric defects occur from the excess fluid deposited during the transient state of DIW. Figure 1.1(a) for a 90-degree turn and Figure 1.1(b) for the bulging corner of a thin wall part are examples of defects created by this behavior.

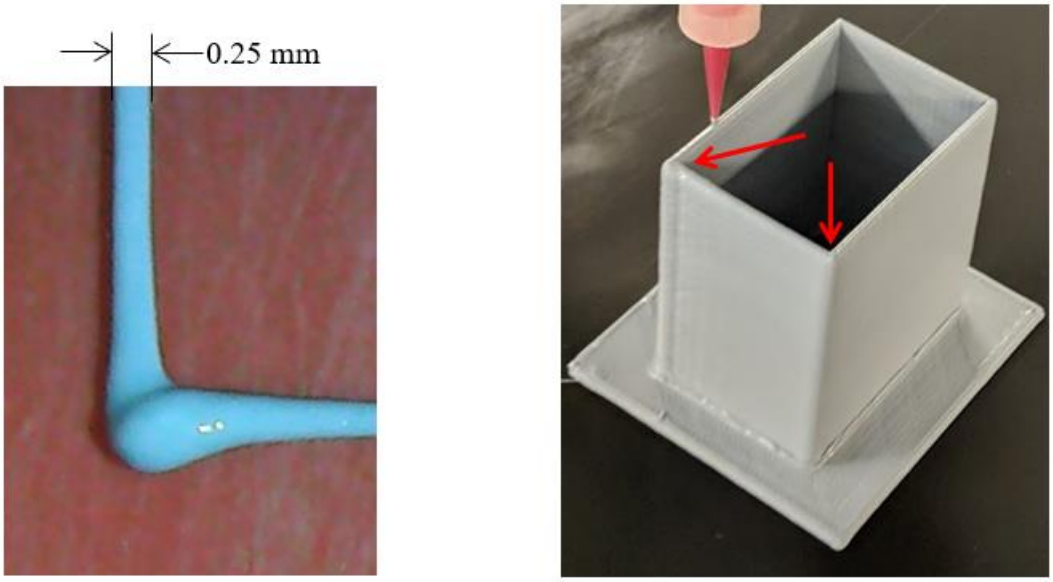

Figure 1.1:(a) Excess material deposition at a 90-degree corner produced by DIW where the material deposition was not matched with machine dynamics and (b) bulging corners on a DIW part.

The solution transient fluid flow put forth in this dissertation requires a detailed understanding of the DIW system behavior and fluid behavior. The DIW system described in more detail in Section 3.5 uses a two-part silicone with in-situ mixing performed by a static mixer, Chapter 2, designed to reduce the pressure drop of the static mixer, making it more efficient for DIW. Next a model of transient fluid flow during DIW, Chapter 3, is derived and validated to quantify the effects transient fluid flow has on DIW. Lastly the transient fluid flow model is used with an optimal control law to create a feedforward controller for the DIW process, Chapter 4.

1.1. Static mixing

Mixing is an industrial process to create a homogenous blend for applications such as chemical reactors and heat exchange [23]. Some standard methods for mixing include the static mixing, stirred vessels, impellers, and manual stirring [24]. Static mixing, commonly used in

chemical and food processing, utilizes pipes with internal elements and fluid momentum to induce flow, which traverses the primary flow direction, creating a homogeneous blend without any moving parts [25]. The advantages of static mixing over other mixing methods include the short mixing time, small profile, continuous mixing, and high repeatability, all desirable properties for processes that require continuous production in a compact space[24].

Four of the most common types of static mixers are the: 1) spiral static mixers (SSM) such as the Kenic KVM™ (Chemineer, Dayton Ohio, USA) and Chemineer HEV™ (Chemineer, Dayton Ohio, USA) 2) corrugated static mixers such as the Koch-Sulzer SMV™ (Sulzer, Winterthur, Switzerland), 3) guide vane static mixers such as the Koch-Glitsch SMX™ (Koch-Glitsch, Wichita Kansas, USA), and 4) crossed elliptical mixers such as the Komax™ mixer (Komax Systems Inc, Huntington Beach California, USA) [24,26]. The SSM is widely used in industry and an active area of research [24,26]. Advantages of SSM are: 1) its versatility in the types of mixing for both laminar and turbulent flows of liquid-liquid, liquid-gas, liquid-solid, and solid-solid mixing [24,26,27], 2) the laminar flow mixing design for liquids [2], 3) the low-pressure drop in comparison to other types of static mixers, such as the SMV™, SMX™, and Komax™ [24,26,27], and 4) the degree of mixing is proportional to the length of the mixer [24,27].

Experimental studies on mixer performance have led to an extensive data set for the pressure drop and mixing of various static mixer designs [24,26,28–31]. As computer simulation has improved, computational fluid dynamics (CFD) has demonstrated its capability to accurately predict pressure drop and mixing of static mixers in single-phase and multiphase flows using techniques such as particle tracking and volume of fluid (VOF) solvers [25,26,32–37]. A plethora of static mixer designs used CFD for their development. Hobbs and Muzzio [38] found

that a slight reduction in the standard twist of 180° in SSM results in a significant increase in performance, such as the extent of mixing per element and energy efficiency. Cheng et al. [39] applied CFD to study static mixer designs that increased cell circulation between light and dark zones in a photobioreactor. Soman [40] showed that the inclusion of small perforations in an SMX^{TM} style mixer design leads to an improvement in the reaction rate of the homopolymerization of acrylamide. Zhang et al. [41] designed a toroidal helix pipe that achieves mixing without any internal elements.

Advancements in additive manufacturing (AM) have enabled the creation of new features in novel static mixer designs. For example, Armbruster et al. [35] utilized AM to fabricate eight new static mixer geometries with turbulence promoters to increase the turbulence flow and prevent fouling of membrane filters. Li et al. [42] applied AM to fabricate a high flow rate microfluidic mixing chamber for the extraction of copper from a sulfite solution. Nguyen et al. [43] studied AM to build an SMX^{TM} style mixer made of nickel so that the static mixer could not only mix but act as a catalyst for chemical processes reducing the size of a tubular production reactor. These recent studies demonstrate that AM enables the creation of novel static mixers that includes features not typical in standard static mixers.

1.2. Modeling of transient fluid flow

There have been investigations into the fluid dynamics of molten plastic deposition in plastic filament material extrusion, commonly referred to as fused filament fabrication (FFF), an MEX process that has a lot of similarities to DIW. Bellini et al. [44] developed a mathematical model for the material flowrate based on the force from the extruder and the heat flux from the heater. The step response of the plastic flowrate was verified in an experimental study. Comminal et al. [45] used computational fluid dynamic (CFD) models of the molten plastic flow

through the nozzle orifice of the extruder in FFF during deposition to demonstrate that mismatches between nozzle speed and material flowrate lead to excess material deposition, similar to the corner swell in Figure 1(a). Ertay et al. [46] created a FFF tool path optimization algorithm that determines the nozzle maximum tangential speed, as constrained by the extruder's capability to deliver the molten plastic. Experimental validation of the algorithm demonstrated improved dimensional accuracy of parts by keeping the actual extrusion rate of plastic proportional to the nozzle speed.

There have been studies to develop mathematical models for transient high viscosity liquid extrusion as well. Hoelzle et al. [47,48] developed a first-order approximation for the delay in the shear-thinning fluid response to changes in a syringe plunger velocity and applied it towards the printing of calcium bone scaffolds. Li et al. [49,50] modeled ceramic pastes as Herschel-Bulkley fluids to simulate the transient response to plunger forces. The model could predict the volumetric flowrate within 6% of the actual flowrate and quantify the effects of bubbles trapped within the ceramic pastes. Simeunovic et al. [51] modeled transient fluid flow as a capacitive system similar to an RC electronic circuit to capture fluid transients in the system that was able to model the output volumetric flowrate within 10% of the actual flowrate. The system compliance in the syringe affected the transient volumetric output behavior for the dynamics of syringe based DIW systems and not applicable for the PDP required for precision DIW. Research into precision liquid dispensing has shown that transient deposition of fluid is a time- and space-dependent process affected by both rheological properties (fluid viscosity, fluid density, and acoustic wave speed), geometrical parameters (pipe length, pipe diameter, and nozzle diameter), and process parameters (input pressure and input flowrate) [52–54]. A deeper understanding of the modeling of the fluid flow for DIW is needed.

Lumped parameter models derived from the momentum equation of fluid dynamics have proven effective in modeling transient fluid response for precision liquid PDP dispensing systems used in electronic packaging [52,53,55,56]. Two critical assumptions for these lumped parameter models are the fluid flow is flowing through a closed pipe (pipe flow), and there is no variation in volumetric flowrate along the length of the system. The DIW process has both long nozzles and static mixers that break these two assumptions [57,58]. There will be a variation in volumetric flowrate along the length of long dispensing nozzles with lengths greater than ten times their diameter during transient flow due to delays in the propagation of pressure in the fluid system [59–61]. The continuity equation of fluid dynamics is required to model the transient fluid flow in DIW with long nozzles or pipe lengths. Static mixers are pipes with internal elements that interrupt flow to cause mixing and enable the use of multipart materials such as silicone, urethane, and resins [58,62,63] in DIW. The assumption of pipe flow is not valid with static mixers because of their internal elements. There are accurate empirical models relating to steady-state flow inside static mixers to the pipe flow [24]. To the authors' knowledge, there is no literature establishing a similar relationship for the transient behavior of fluid in static mixers. Without the simplifying assumptions of no variation in flowrate or pipe flow, a generalized model using both the continuity and momentum equations is needed to analyze the fluid flow in DIW. This generalized model will be able to characterize the DIW fluid dispensing system and provide insight into ways to control the deposition of high viscosity fluid during the printing process.

1.3. Feedforward control in AM

There are two main methods of control, feedback and feedforward [64]. Feedback control uses measurements of system state to correct for error and excels at maintaining system

stability[64–66]. However feedback control is weak at correcting for large system disturbances, such as those created by transient system states while minimizing system error [64,66]. Feedforward control uses a system model to adjust for changes in system state in advance and is ideal for situations where overall system error needs to be minimized [64,66].

Feedforward control and using process models to correct AM parts defects have been adopted in powder bed fusion (PBF), an AM process that uses a laser to fuse powdered metal into three-dimensional parts [67–69]. Wang et al. implemented a feedback controller for laser power within a PBF simulation to generate a corrected laser tool path to reduce part defect rate by 23-40% [67]. Druzgalski et al. created a framework for simulating, correcting, and applying the updated laser tool paths to small features common to complex parts and demonstrated that these corrections could be applied in new parts [68]. Khairallah et al. used a proportional integral derivative (PID) controller in a PBF simulation to control molten metal depth induced by laser [69].

A MEX machine's motion is produced with trapezoidal motion planning that assumes the machine's dynamics, including material deposition extrusion flowrate vs. nozzle speed, are linear [70,71]. Trapezoidal motion planning has proven very useful and easy to implement for MEX of thermoplastics [10] and also serves as an accurate process model for the DIW machine dynamics enabling the use of feedforward control for machine dynamics. With an accurate process model for transient fluid flow, it is possible to implement feedforward control to improve the accuracy and quality of parts in DIW in a similar manner to what has been done with PBF [72].

1.4. Research gaps

Key gaps in research addressed by this dissertation include the following: (1) No previous study demonstrated the use of AM to reduce pressure drop in a static mixer. (2) No general

model of transient fluid flow in DIW exists. (3) No models for transient fluid flow through a static mixer on a macro scale exist. (4) There are no examples of feedforward control in DIW. (5) No use of optimal control in DIW material deposition. To address these gaps a focused multi-disciplinary effort covering chemical engineering, fluid dynamics, system design, and control will be needed. The research goals of which are to: 1) understand the system properties critical to the DIW system, 2) develop a transient fluid model for deposition in DIW, and 3) creation of control policy that corrects for deficiency of transient response of fluid deposition in DIW.

This dissertation aims to investigate the behavior transient mixing and deposition of fluids in DIW to improve the quality of DIW parts. Chapter 2 of this dissertation describes the design and testing of a novel static mixer design using AM. Chapter 3 describes a transient fluid model that characterizes the deposition of fluid in the DIW process, a key part of this chapter is the characterization of fluid flow through a static mixer enabled by Chapter 2. The transient fluid model is validated and used to predict errors in DIW tool paths. Chapter 4 uses the transient fluid model from Chapter 3 as the foundation of a feedforward controller. The feedforward controller uses both machine learning and optimal control to reduce the errors in DIW tool paths and improve the quality of a test DIW part. Chapter 5 covers the major contributions made by this dissertation and a discussion of areas for future research.

Chapter 2. Pressure Drop Reduction of an Impeller Spiral Static Mixer Design Enabled by Additive Manufacturing

2.1. Abstract

A new spiral static mixer (SSM) design, also known as helical or twisted tape mixers, called the Impeller SSM, inspired by centrifugal pump impeller blades and fabricated by additive manufacturing (AM), is presented. The pressure drop and mixing efficiency of an Impeller SSM are compared to the standard SSM. Both the pressure drop and mixing characteristics are measured experimentally and validated by computational fluid dynamics (CFD) analyses. Five Impeller SSM designs of different taper, release, and attack angles were studied. Compared to a standard SSM of the same size, the Impeller SSM demonstrated a pressure drop (and power) reduction up to 18.2%. Such reductions could lead to significant energy saving and size reduction in static mixer industrial applications. Experimental results also show the ability of AM to fabricate the custom Impeller SSM without using costly machining and joining techniques.

2.2. Introduction

Spiral static mixers (SSM) are one of the most common static mixer designs. SSM has several advantages over other common static mixer designs. 1) It is usable for a wide variety of mixing situations such as mixing of either laminar and turbulent flows, mixing of liquids with liquids, mixing liquids with gas, and mixing liquids with solids [24,26,27]. 2) The SSM is able to mix liquids with laminar flow [2]. 3) The SSM design has a lower pressure drop in comparison

to other types of static mixers, such as the SMV™, SMX™, and Komax™ [24,26,27]. 4) The degree of mixing in a SSM is a function to its length [24,27].

In this chapter the SSM design is modified based on a centrifugal pump impeller blade to reduce the pressure drop, Section 2.3. The empirical equations that define a SSM's behavior are discussed in Section 2.4. The new SSM design is enabled by additive manufacturing and is discussed in Section 2.5. The computational fluid dynamics (CFD) modeling of the SSM's used in this study and the experimental validation set up are discussed in Section 2.6 and 2.7 respectively. Lastly the results of the experimental validation and CFD as well as the conclusions are shown in Sections 2.8 and 2.9.

2.3. Standard SSM Design

A standard SSM, as shown in Figure 2.1(a), is characterized by stacking alternating clockwise (CW) and counterclockwise (CCW) helical elements. In Figure 2.1(b), each helical element is offset by 90° and interfaces at points B_1, A_2, B_2, A_3, etc. The CW and CCW helical elements are illustrated in Figure 2.1(c) and (d), respectively. Alternating CW and CCW elements of the standard SSM causes the fluid flow to repeatedly split and recombine following a baker transformation, which is a mapping operation that cuts and recombines an arbitrary space, always resulting in a chaotic distribution [73]. The number of layers of two fluids increases exponentially until the fluid is homogeneously blended by passing through the alternating CW and CCW helical elements in the SSM [24]. As shown in Figure 2.1, four parameters define the SSM are: 1) helix diameter, d, 2) helix length, l, 3) helix thickness, t, and 4) overall length, L. The standard geometry for each helical element is to have the helix length, l, to be approximately 1 to 1.5 times the diameter, d, with a pitch $p = 2l$ [24,74]. The standard thickness of a helix is not specified but should be as thin as possible. In Figure 2.1(c) and (d), the CW and CCW helical

elements are shown cut from a full helix, which is a helix with a pitch *p*. Additionally, the origin of each helix is denoted as point A, and the end of each helix along the *z*-axis is labeled as point B. An isometric view of the SSM can be seen in Figure 2.1(b), showing the A-B interfaces of each helix in the Standard SSM.

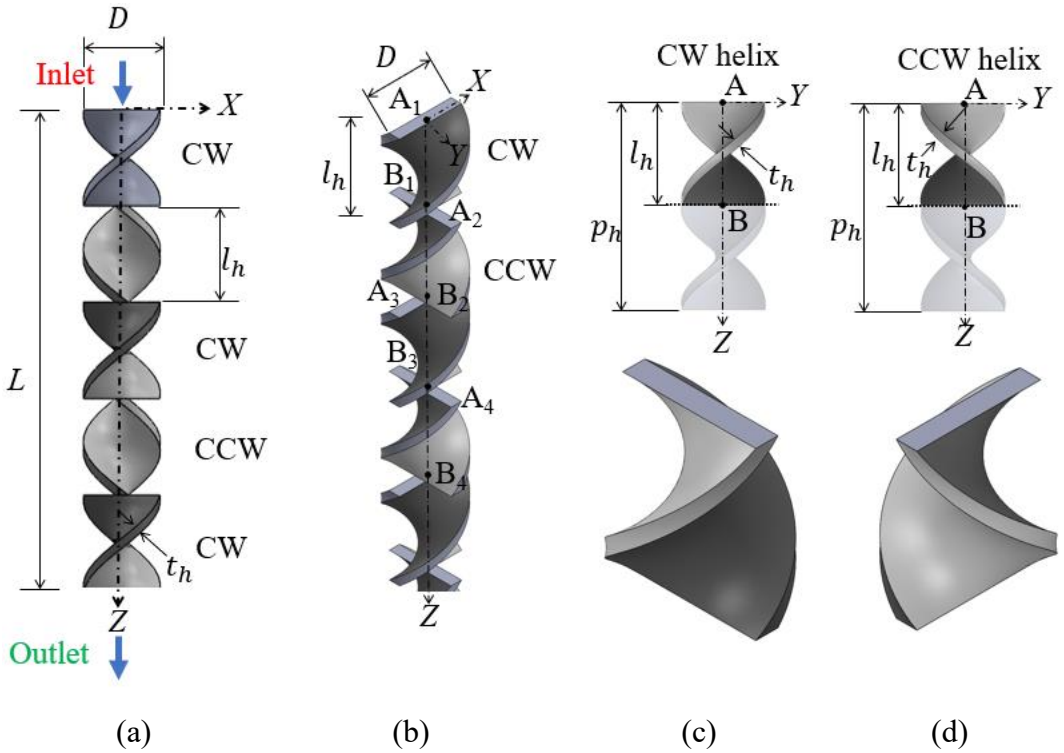

Figure 2.1: A standard SSM with alternating clockwise (CW) and counter-clockwise (CCW) helix rotations with four parameters, 1) helix diameter, *d*, 2) helix length, *l*, 3) helix thickness, *t*, and 4) overall length, *L*: (a) the side and (b) perspective view of a standard SSM with alternating CW and CCW helical elements and (c) the CW and (d) CCW helix elements with point A at the top of the helix and point B at the bottom of the helix on the *z*-axis.

The surfaces at points A and B along the helix centerline are flat surfaces perpendicular to the fluid flow in the SSM, as shown in Figure 2.1. These flat surfaces abruptly interrupt the flow of fluid within the SSM, increasing drag within the SSM and reducing the SSM efficiency.

2.4. Impeller SSM Design

The Impeller SSM design, as shown in Figure 2.2, improves the SSM performance by reducing the abruptness of the fluid transition between each helical element. The core concept for the Impeller SSM came from centrifugal pumps where reduction of impeller blade angles to less than 90° with respect to the flow direction has been shown to reduce losses [75]. Centrifugal pumps have impellers with curved blades that have a similar twist shape to the helixes in an Impeller SSM. For centrifugal pumps, the fluid is rotated around a center axis by the spinning impeller. The behavior is very similar to SSM's where fluid flows around the central axis of the helix elements. The Impeller SSM introduces the three new parameters, 1) taper angle, α, 2) release angle, β, and 3) attack angle, γ, to create the taper inlet, release winglet, and attack angle features on the SSM helix element and reduce the resistance to the fluid flow.

The application of the Impeller SSM parameters happens in two stages. The first stage creates the intermediate Impeller SSM helix element, which is derived from the helix elements of standard SSM in Figure 2.1. The helix created by cuts along planes P-P and Q-Q in Figure 2.2 defines an intermediate CW helix element of the Impeller SSM. Figure 2.2(a) shows planes P-P and Q-Q that cut a CW Impeller SSM helix element and create the taper inlet at the entrance and the release winglet at the exit, respectively. Plane P-P intersects point A and is used to define α, which is the angle between the P-P and *x*-*y* planes. In Figure 2.2(b) and (c), the green surface indicates the taper inlet. Plane Q-Q intersects the *z*-axis at point B and is used to define the release winglet. The release angle, β, is the angle between the Q-Q and *x*-*y* planes. In Figure 2.2(b) and (c), the red surface indicates the release winglet. Using this planer definition for the taper inlet and release winglet preserves the helix twist while creating an angled surface relative to the fluid flow reducing drag within the SSM.

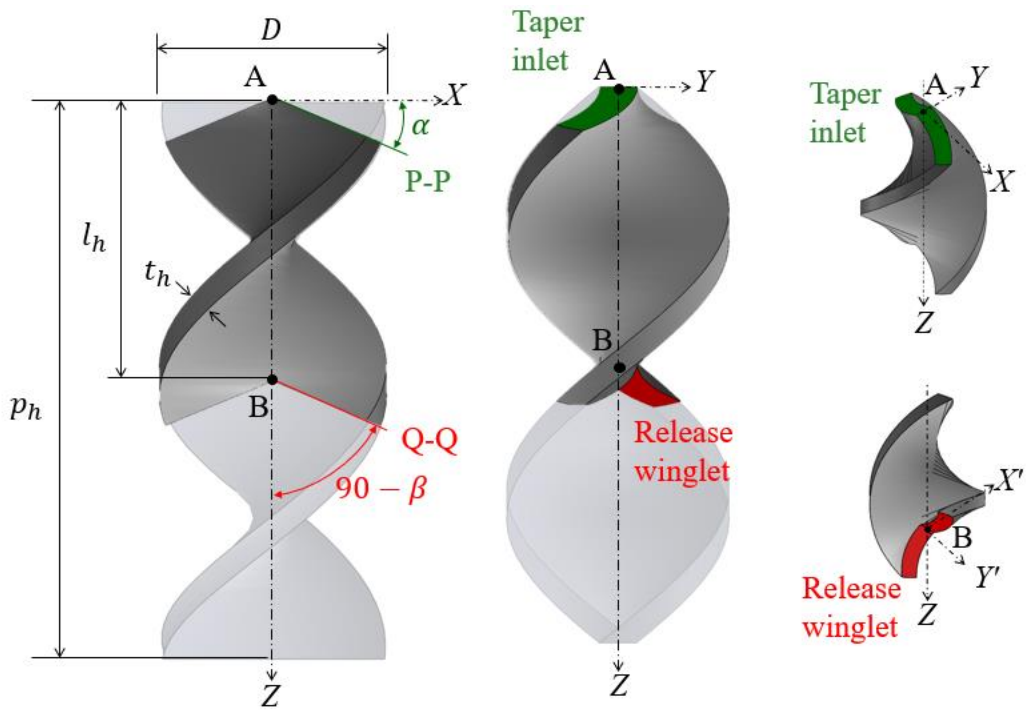

Figure 2.2: (a) Front view of the Intermediate helix element created by cuts from P-P and Q-Q planes. The P-P plane intersects the *z*-axis at point A, has an angle α with respect to the *x*-*y* plane, and is perpendicular to the *x*-z plane. The Q-Q plane intersects the *z*-axis at point B, has an angle β with respect to the *x*-*y* plane, and is perpendicular to the *x*-*z* plane. (b) Side view of the Intermediate helix where taper inlet is shown in green and release winglet is shown in red and (c) isometric views of the intermediate helix element showing more detail of the taper inlet and release winglet.

The second stage of Impeller SSM application is the application of the attack angle, γ, to sharpen the taper inlet and release winglet of the intermediate Impeller SSM helix to reduce the flow resistance. The vertex of the taper inlet is on point A of the intermediate helix element, as shown in Figure 2.3(a). For the taper inlet, in the *y*-*z* plane, triangles ACD and AGH are defined on the side of inner and outer edges ef and ij, respectively. The angle between lines AD and AC (along the *y*-axis) is γ in triangle ACD. Similarly, the angle between lines AH and AG (along the *y*-axis) is also γ in triangle AGH. Triangles ACD and AGH are swept along edges ef and ij to triangles A'C'D' and A'G'H', as shown in Figure 2.3(b) and (c), respectively, to complete the

creation of a sharp taper inlet shown in Figure 2.3Figure 2.3(d). The same procedure is repeated for the release winglet using point B as the vertex, Figure 2.3(e). The sharpened release winglet of the CW Impeller SSM helix elements is shown in Figure 2.3(f).

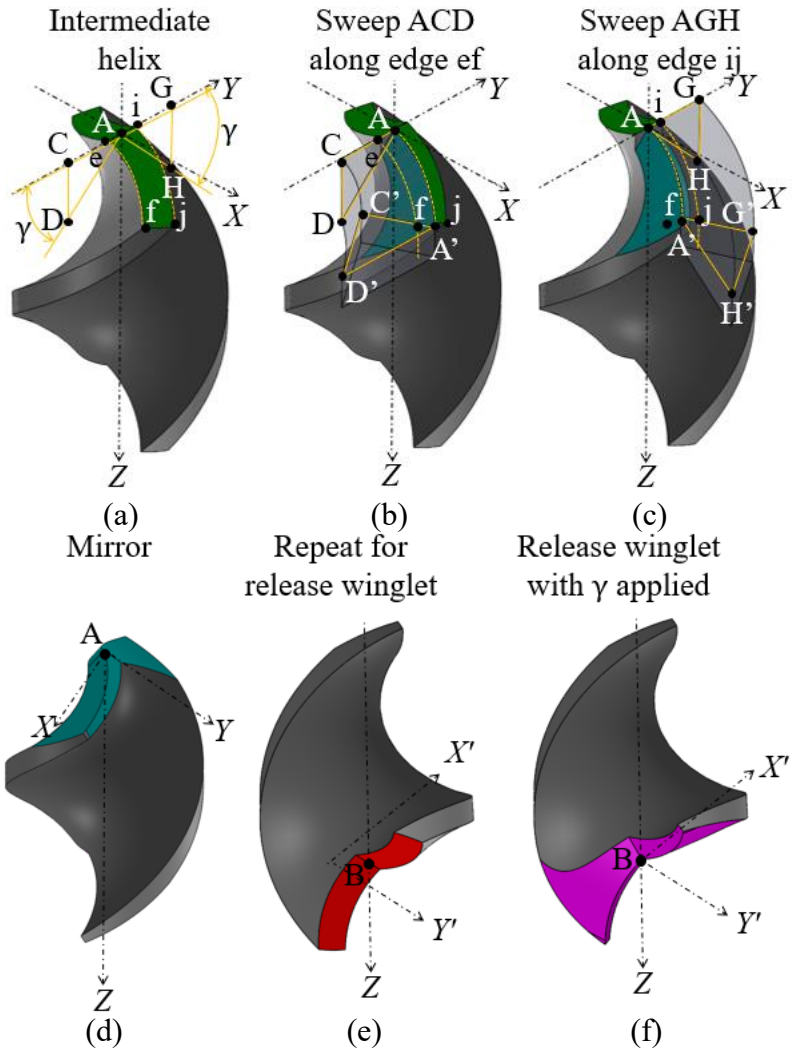

Figure 2.3: (a) Isometric views of the Intermediate helix element showing the attack angle, γ, and vertex points A and B, (b) the first sweep of triangle ACD along the edge ef to triangle A'C'D' of the Intermediate helix element, (c) the second sweep of triangle AGH along the outer edge ij to triangle A'G'H' of the Intermediate helix element, (d) the sharpened taper inlet of the intermediate helix, (e) the release winglet and vertex point B used for the origin for application of the attack angle, and (f) the sharpened release winglet of the Impeller helix element.

Both CW and CCW Impeller SSM helix elements are constructed using this method and alternated between the two with 90-degree offset to assemble as a completed Impeller SSM, as shown in Figure 2.4. The sharp taper inlet separates the fluid flow, as shown in Figure 2.4(a),

reducing the resistance of the fluid transfer from helix to helix within the SSM. The taper inlet and release winglet are colored as teal and purple, respectively. The Impeller SSM shown in Figure 2.4(b) uses the same base dimensions, D, l_h, t_h, and L of a standard SSM and are assembled in the same manner as the standard SSM with α = 22.5-degree, β = 22.5-degree, and γ = 22.5-degree. The isometric view of the Impeller SSM with five helix elements is shown in Figure 2.4(c).

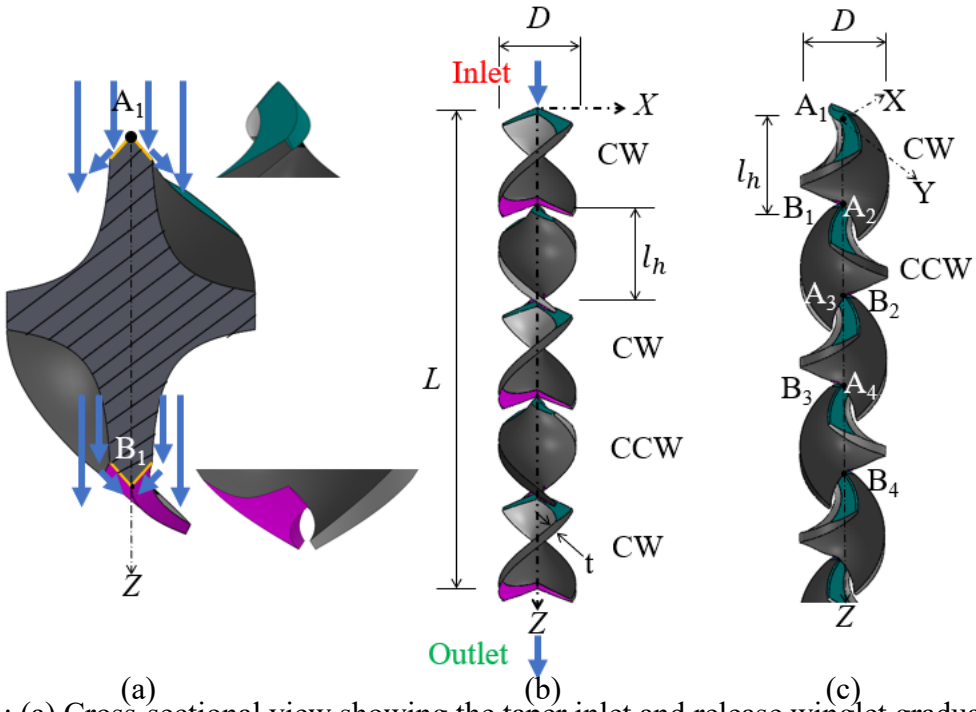

(a) (b) (c)

Figure 2.4: (a) Cross-sectional view showing the taper inlet and release winglet gradually divert flow reducing drag, the close-up views of the sharpened taper inlet and release winglet. (b) The side view of Impeller SSM with the same D, l_h, t_h, and L as the Standard SSM shown in Figure 2.1, and α = 22.5-degree, β = 22.5-degree, and γ = 22.5-degree. (c) The isometric view of Impeller SSM.

Each new feature of the Impeller SSM may reduce the losses associated with the fluid flow transitioning from helix to helix. These new features would be extremely difficult to fabricate using traditional machining, forming, or molding techniques. Most of this difficulty is from the undercuts created by the taper inlet and release winglet and the fine feature size of the

attack angle. The undercuts and fine feature would require the use of complex tooling and extensive machining operations [76]. Using AM, the Impeller SSM design can be produced quickly and with the freedom to vary the design parameters as needed.

The Impeller SSM has the same D, l_h, t_h, and L as the standard SSM while α, β, and γ are varied through various configurations for testing to explore their effects on the pressure drop within the Impeller SSM. The various configurations of the Impeller SSM will be referenced as α-β-γ (in the unit of degrees) are shown in Table 2.1 and compared in Figure 2.5.

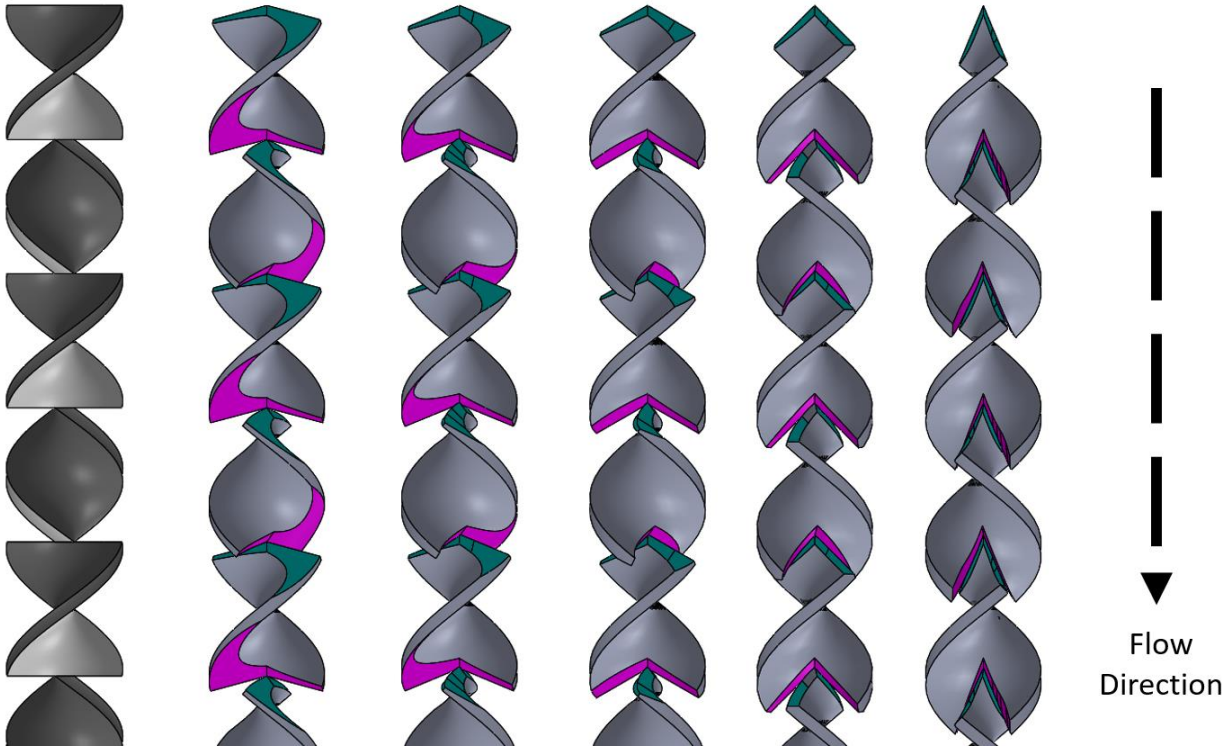

(a) (b) (c) (d) (e) (f)

Figure 2.5: The (a) standard SSM, (b) 15-15-22.5, (c) 22.5-22.5-22.5, (d) 30-30-22.5, (e) 45-45-22.5, and (f) 67.5-67.5-22.5 Impeller SSM

Table 2.1: SSM parameters and dimensions used in this study

Mixer	L (mm)	D (mm)	l_h (mm)	t_h (mm)	α (degree)	β (degree)	γ (degree)
Standard SSM	53	3.0	3.75	0.5	0	0	0
15-15-22.5	53	3.0	3.75	0.5	15.0	15.0	22.5

Mixer	L (mm)	D (mm)	l_h (mm)	t_h (mm)	α (degree)	β (degree)	γ (degree)
22.5-22.5-22.5	53	3.0	3.75	0.5	22.5	22.5	22.5
30-30-22.5	53	3.0	3.75	0.5	30.0	30.0	22.5
45-45-22.5	53	3.0	3.75	0.5	45.0	45.0	22.5
67.5-67.5-22.5	53	3.0	3.75	0.5	67.5	67.5	22.5

2.5. Static mixer pressure drop and length

Two important parameters that indicate static mixer performance are the length required for adequate mixing and pressure drop over that length. This section presents the characteristic equations to estimate the required length and associated pressure drop.

2.5.1 Pressure Drop

The pressure drop created by the static mixer, ΔP_{sm}, is calculated using the static mixer length parameter, K_l.

$$K_l = \frac{\Delta P_{sm}}{\Delta P} \tag{2.1}$$

where ΔP is the pressure drop in an open pipe with the same D and L of the static mixer.

The pressure drop in an open pipe during laminar flow is expressed as [24]:

$$\Delta P = \frac{32}{Re}\frac{L}{D}\rho u^2 \tag{2.2}$$

where ρ is the fluid density, u is the fluid speed, $Re = \rho u d/\mu$ is the Reynolds number of the flow, and μ is the fluid viscosity.

Using Eqs. (2.1) and (2.2), the pressure drop of the fluid flow for a static mixer is:

$$\Delta P_{sm} = 32 K_l \frac{\mu L u}{D} \tag{2.3}$$

For an SSM, K_l has experimentally been determined to be 6.9 [24].

If the fluid is shear-thinning, the effective viscosity of the fluid, μ_{eff}, for Re can be calculated using the shear rate G' of the static mixer and the fluid power law [75]. For a static mixer, the shear rate can be approximated by the following [24]:

$$G' = K_g \frac{u}{D} \tag{2.4}$$

where K_g is the static mixer shear rate coefficient, shown to be 28 in a Kenics SSM [24].

The power fluid law using G' becomes [75]

$$\mu_{eff} = kG'^{N-1} \tag{2.5}$$

where k is the fluid consistency index and N is the flow behavior index.

The pressure drop in a static mixer predicted by Equation (2.3) does not take into consideration effects such as surface roughness or manufacturing variation but has proven to be within 15% of the actual pressure drop [24].

2.5.2 Mixer Length

The length of a static mixer is determined by the distance needed to achieve an adequately mixed fluid. The coefficient of variation, CoV_r, is a measure of how homogeneous the fluid mixture is. For a static mixer, the CoV_r is [24]

$$CoV_r = K_i^{L/D_h} \tag{2.6}$$

where K_i is the blending parameter and d_h is the hydraulic diameter of the static mixer. In an SSM, K_i has experimentally been shown to be 0.87 [24]. The amount of volume that a static mixer occupies in relation to the pipe volume will change the mixing behavior of the static mixer [24]. The use of d_h accounts for this by adjusting the effective size of the static mixer for the purposes of determining its length.

The exact CoV_r depends on the application, 0.05 is generally considered well mixed, but in more demanding mixing applications, such as mixing for color consistency, a lower CoV_r value of 0.01 should be used [24].

$$D_h = 4\frac{A}{P_c} \tag{2.7}$$

where A is the cross-sectional area of the static mixer and P_c is the cross-sectional perimeter.

Based on Eqs. (2.6) and (2.7), the minimum static mixer length needed to achieve an effectively homogeneous fluid mixture is:

$$L = 4\frac{A}{P_c}\frac{\log CoV_r}{\log K_i} \tag{2.8}$$

2.6. Design and Additive Manufacturing of Standard and Impeller SSMs

The standard SSM design, Figure 2.6(a), used for this study has a d = 3 mm, l = 3.75 mm, and t = 0.5 mm, all of which are within the design guidelines for a standard SSM [23]. The d and t values result in A_c = 5.58 mm^2 and P_c = 14.34 mm as determined by the 3D model of the SSM element. The A_c and P_c with a given CoV = 0.01 and K_i = 0.87 are used in Eq. (2.8) to determine L = 53 mm (14 helical elements) for a mixing application that needs color consistency. Figure 2.6(b), the 22.5-22.5-22.5 Impeller SSM is shown with α = 22.5°, β = 22.5°, and γ = 22.5° (as described in Figure 2.4). To allow for experimental measurement of pressure drop, the SSM also has two M5 threaded pressure sensor ports placed at 7 mm and 37 mm from the start of the SSM, as shown in Figure 2.6(c). Figure 2.6(d) shows the internal cut-out of a standard SSM manufactured on a stereolithography (SLA) AM machine (Form 2, FormLabs Somerville Massachusetts, USA) with two pressure sensors installed. All SSMs in this study were printed using SLA resin (Clear v4, FormLabs Somerville Massachusetts, USA) and a layer height of 0.05 mm. The internal cut-out of a 22.5-22.5-22.5 Impeller SSM can be seen in Figure 2.6(e) showing the fine features produced by AM. The size and dimensions of the AM parts were validated using a caliper (8000-F6, Products Engineering Corporation, Torrance California, USA).

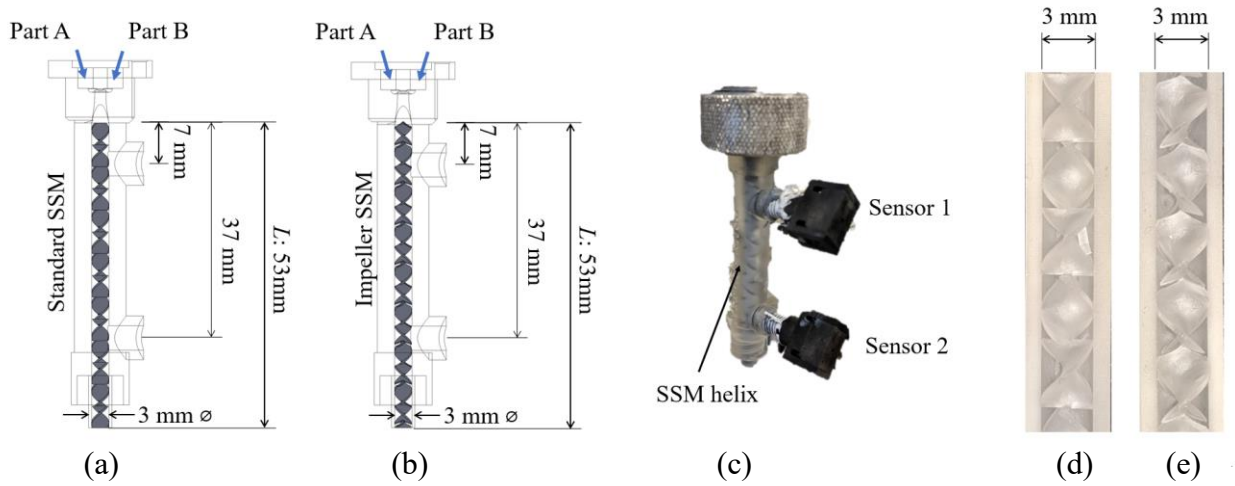

Figure 2.6: (a) The standard SSM and (b) 22.5-22.5-22.5 Impeller SSM with the location of the pressure ports and overall length annotated, (c) the standard SSM produced using SLA and with pressure sensors installed, and cutaway view of the (d) standard SSM and (e) 22.5-22.5-22.5 Impeller SSM produced using SLA.

As shown each standard SSM and Impeller SSM configuration take approximately 7 mL of resin to be made on the SLA AM machine. At the time of writing one liter of resin costs $149, making the total material cost per SSM is approximately $1.05. This makes the cost of producing a SSM comparable to purchasing commercially available static mixers of comparable size and length.

2.7. CFD modeling of standard SSM and Impeller SSM

CFD modeling was used to accurately simulate the pressure drop of the standard SSM and Impeller SSM. Using CFD will provide a detailed analysis of the fluid flow within the static mixers that cannot be easily obtained experimentally. The Fluent^{TM} (v19.1) CFD software package from ANSYS (Canonsburg Pennsylvania, USA) was used to simulate the fluid flow in the standard SSM and various Impeller SSM configurations.

2.7.1 CFD Mesh, Boundary Conditions, and Initial Conditions

The mesh for the CFD was generated from the 3D CAD model of the standard SSM and Impeller SSM configurations, by using a Boolean subtract on the 3D model to isolate the fluid regime within the 3D model. In Figure 2.7(a), the 3D CAD models for a standard SSM and a 22.5-22.5-22.5 Impeller SSM are shown. In Figure 2.7(b), the fluid domain inside both SSMs is generated from a Boolean subtract operation. Figure 2.7(c) shows the tetrahedral mesh generated on the fluid domain by the ANSYS meshing tool using the patch conforming method [26] with a mesh size of 0.2 mm, resulting in 6.6x10^6 meshing elements and was checked for independence. Due to the size of the model relative to the mesh size, only a small portion of the mesh is shown for visualization purposes.

The boundary conditions of the CFD model are assumed to be a constant volumetric flow inlet, gauge pressure outlet, and non-slip walls. The fluids used in the CFD models are made up of two parts, Part A and Part B. Each fluid part has a separate constant volumetric flow inlet, as shown in Figure 2.6(a) and (b). The Volume of Fluid (VOF) model [12] was used for the multiphase flow of both the Part A and Part B components flowing through the static mixer. The material properties used for the CFD model are discussed in the next section. The initial conditions for the model were determined using the hybrid initialization feature of Fluent^{TM} [27].

The predicted pressures at points S1 and S2, which are 7 mm and 37 mm, respectively, from the start of the SSM, as indicated in Figure 2.7(a), (b), and (c), are captured as output and will be compared against experimental data. In order to evaluate the level of mixing, contour plots showing the volume fraction of Part A and Part B are captured at the entry and in the middle of the first four elements of both the standard SSM and Impeller SSM, as shown in Figure 2.7(d).

The CFD model for the standard SSM and Impeller SSM configurations were based on an alkoxysilicone sealant silicone from Dow, Inc. (Midland, MI, USA) with Part A and Part B components as the model fluids. The alkoxysilicone mixture was simulated at three volumetric flow rates: 1, 2, and 3 mL/min. The Part A and Part B components individually had a flow rate half of the overall volumetric flow rate; i.e., 0.5, 1, and 1.5 mL/min. For each flow rate, the CFD model was run until the pressure and volume fraction achieved steady-state. A total of 18 CFD simulations were conducted on the three flow rates and six SSM configurations.

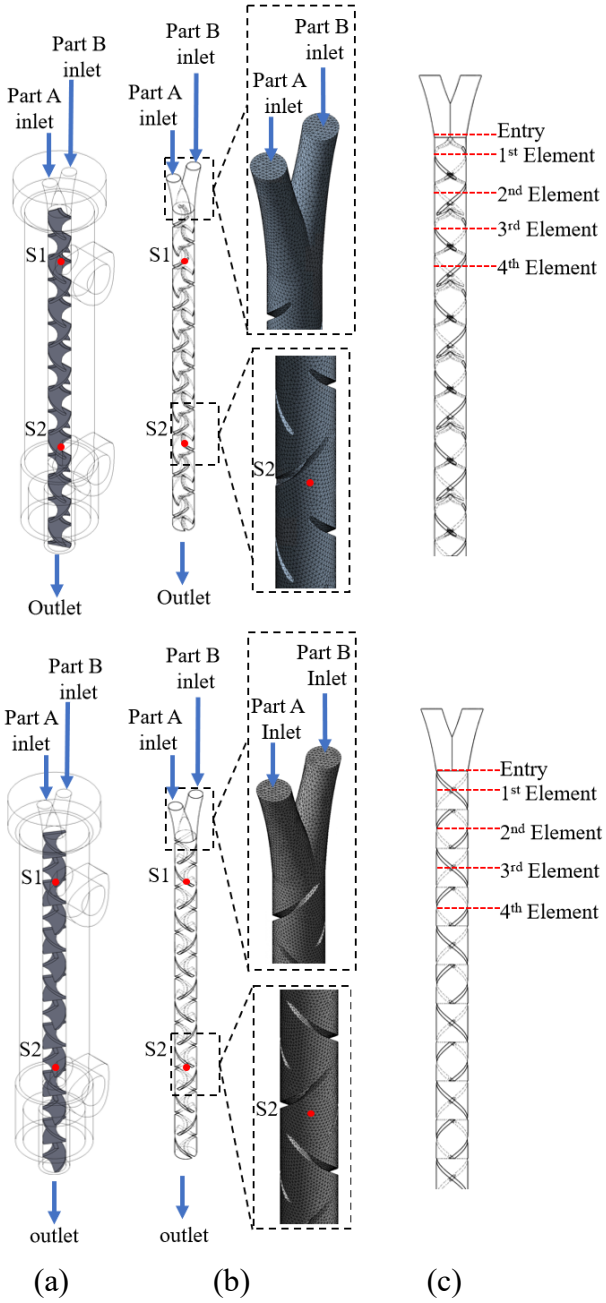

Figure 2.7: (a) The 3D model and (b) the fluid domain of the CFD models for the standard SSM and 22.5-22.5-22.5 Impeller SSM showing the fluid inlets, outlet, and pressure measurement locations marked, (c) the CFD mesh for standard SSM and 22.5-22.5-22.5 Impeller SSM, and (d) the mixing of the CFD model to be measured at the entry and middle of the first four elements for every SSM configuration.

2.7.2 Fluid Properties in CFD

The densities, ρ, and viscosities, μ, of the alkoxysilicone Part A and Part B components are required as inputs for the CFD model. The densities for Part A and Part B are 1350 and 1240 kg/m^3, respectively. A power law viscosity model, Eq. (2.5), is used to capture the shear thinning rheological characteristics of the alkoxysilicone components as shown in Figure 2.8. The fitted power law equation parameters for Part A and Part B are = 190 and 1110 Pa-s for *k* and 0.7 and 0.5 for *N*, respectively.

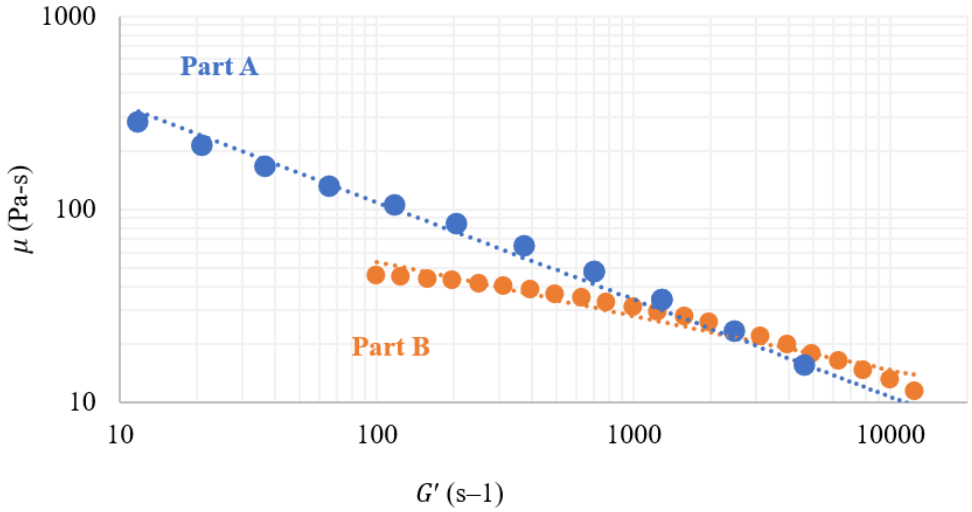

Figure 2.8: Rheological data for alkoxysilicone provided by Dow, Inc.

2.8. Experimental setup of pressure measurement of standard and Impeller SSMs

An experimental pressure drop measurement was performed to validate the CFD models of the standard SSM and various Impeller SSM configurations. The fluid flow in the standard SSM and various Impeller SSM configurations was created using a dual progressive cavity pump (Model PTC 2-SD01, Shanghai Baoling Intelligent Technology Co., Shanghai, China) shown in Figure 2.9. Progressive cavity pumps are a type of positive displacement pump where a rotor forces fluid through a series of fixed cavities, which creates a precise constant volumetric flow rate for both high and low viscosity fluids [79]. These dual progressive cavity pumps, which are

placed next to one another, deliver two fluids, Part A and Part B, to the SSM to replicate conditions from the CFD model.

The progressive cavity pump flow rate was calibrated by dispensing the alkoxysilicone through each static mixer for 60 seconds and weighing the material extruded through the mixers using an electronic scale (Model Tree HRB103, LW Measurements LLC, Rohnert Park, CA, USA). The calibrated flow rates used in all experiments are 0.99±.03, 2.02±.03, and 2.98±.03 mL/min for the target volumetric flow rates of 1, 2, and 3 mL/min respectively.

Pressure sensors (Model 24PCGFH6G, Honeywell Charlotte North Carolina, USA) are installed into the two pressure ports on the standard SSM and Impeller SSM configurations. The pressure sensors installed at the 7 mm and 37 mm locations are marked as Sensor 1 and Sensor 2, respectively, as shown in Figure 2.9. The signal from the pressure sensor is amplified by a custom op-amp circuit with a gain of 10 and was read by the analog input of an Arduino microprocessor (Arduino Mega 2560 Rev3) at a 30 Hz sampling rate. Both pressure sensors were calibrated using a pressure gauge (Model DPGA-07, Dwyer Instruments Michigan City Indiana, USA) and a custom pressure manifold. The pressure manifold was pressurized and the readings from the pressure sensors and gauge were taken. The calibration showed a linear response to changes in pressure and approximately 1% hysteresis in the pressure measurement, which conforms to the sensor datasheet [80].

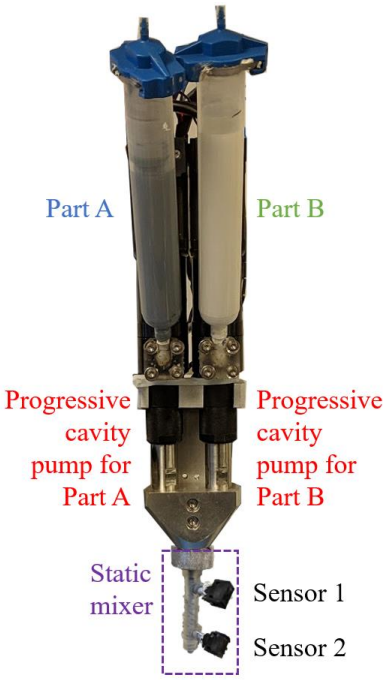

Figure 2.9: The dual progressive cavity pump used for dispensing Part A and Part B at a constant volumetric flow rate. The displayed standard SSM has two pressure sensors for monitoring the pressure drop.

For all tested configurations, the progressive cavity pump was run at the calibrated target flow rate of 1, 2, and 3 mL/min for 20 seconds with the pressure at Sensors 1 and 2 recorded. The steady-state pressure drop between Sensors 1 to 2 is calculated by averaging the difference of pressure for the middle 15 seconds of the steady-state to ignore transient effects caused by the starting or stopping of the flow. This experimental procedure was repeated three times for each of the 18 CFD simulations for a total of 54 tests.

2.9. Results

Results of the pressure drop from the experiments and CFD simulations for all SSM configurations are compared to determine validly of the CFD simulations. The empirical model for the pressure drop within a standard SSM is used to validate the CFD results for the standard SSM. Further analysis of the fluid velocity within each SSM from the CFD simulations will

provide further insight into how the Impeller SSM parameters affect the internal fluid flow to reduce its pressure drop.

2.9.1 Pressure Measurements and Validation of CFD Model

Figure 2.10 shows the pressure data recorded from the 22.5-22.5-22.5 Impeller SSM with a 1 mL/min volumetric flow rate of alkoxysilicone at Sensors 1 and 2 as well as the pressure difference between these two sensors. This test begins at the 4 seconds, ends at the 24 seconds and the steady-state region is between 6.5 and 21.5 seconds. The pressure difference between Sensors 1 and 2 in the steady-state area is averaged to determine the pressure drop of the SSM for this test. By only using data from the steady-state region, effects of the transients created by the progressive cavity pumps starting and stopping the flow and the residual pressure that remained within the SSM in between tests do not significantly affect the pressure measurement data.

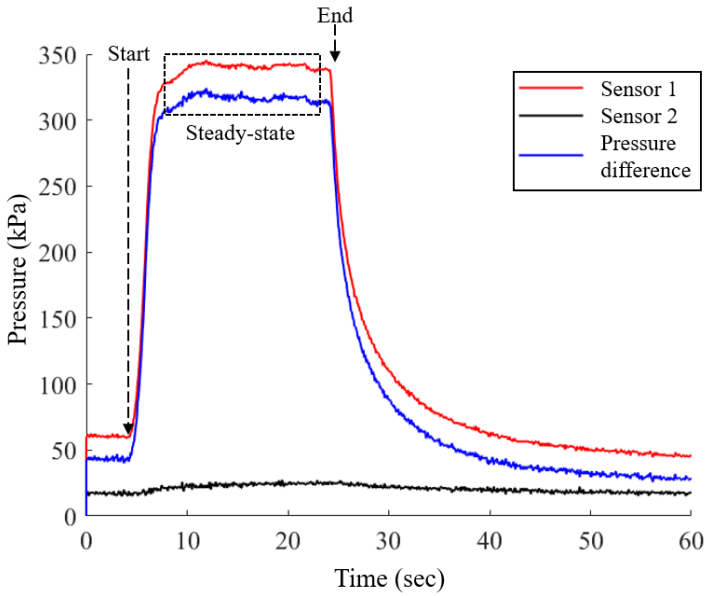

Figure 2.10: Pressure recorded using the Sensors 1 and 2 for 22.5-22.5-22.5 Impeller SSM with a 1 mL/min volumetric flow as well as the pressure difference between them. The test began at 4 seconds, ended at 24 seconds, and the steady-state region was between 6.5 and 21.5 seconds.

The 22.5-22.5-22.5 Impeller SSM CFD steady-state pressure data for the same 1 mL/min flow rate is shown in Figure 2.11. For CFD simulations, the pressure drop used to compare with experimental results for all tested standard SSM and Impeller SSM configurations is the difference in pressure between points S1 and S2. For the 1 mL/min flow rate, the CFD simulation showed a pressure drop of 378 and 301 kPa between S1 and S2 for the standard SSM and 22.5-22.5-22.5 Impeller SSM, respectively, a 20.3% reduction in pressure drop. Experimentally at the same flow rate, the average experimental pressure drop was 392 and 320 kPa for the standard SSM and 22.5-22.5-22.5 Impeller SSM, respectively, a 18.2% reduction in pressure drop.

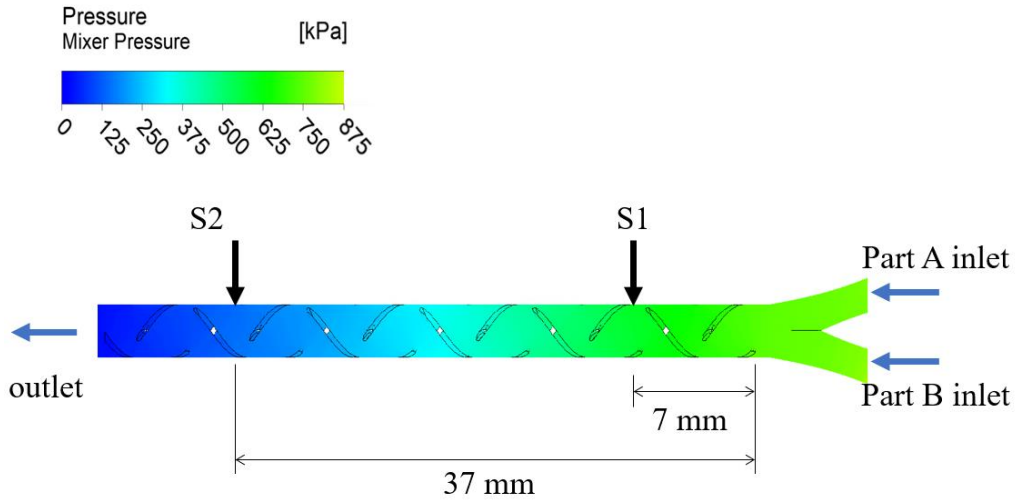

Figure 2.11: CFD pressure data for the 22.5-22.5-22.5 Impeller SSM with a 1 mL/min steady-state volumetric flow rate. The pressure drop is the difference in pressure at S1 and S2.

The pressure drops between Sensors 1 and 2 from the experiments and between S1 and S2 in CFD models are presented in Figure 2.12 for all 6 tested SSM configurations. The error bars on the experimental values represent the range of pressure drop recorded during the experimental tests and the dotted line is the expected pressure drop in the static mixer over a 30

mm distance predicted by Equation (2.3) using the *d* and *L* of the standard SSM from Table 2.1 and the fluid properties presented in Section 2.4.

The results show a good agreement between the CFD and experiments on the pressure drop for both SSMs and materials. For all standard SSM experiments and CFD models, the expected pressure drop predicted by Equation (2.3) was within 15% of the actual pressure drop indicating the results conform with the expected performance of a standard SSM [24].

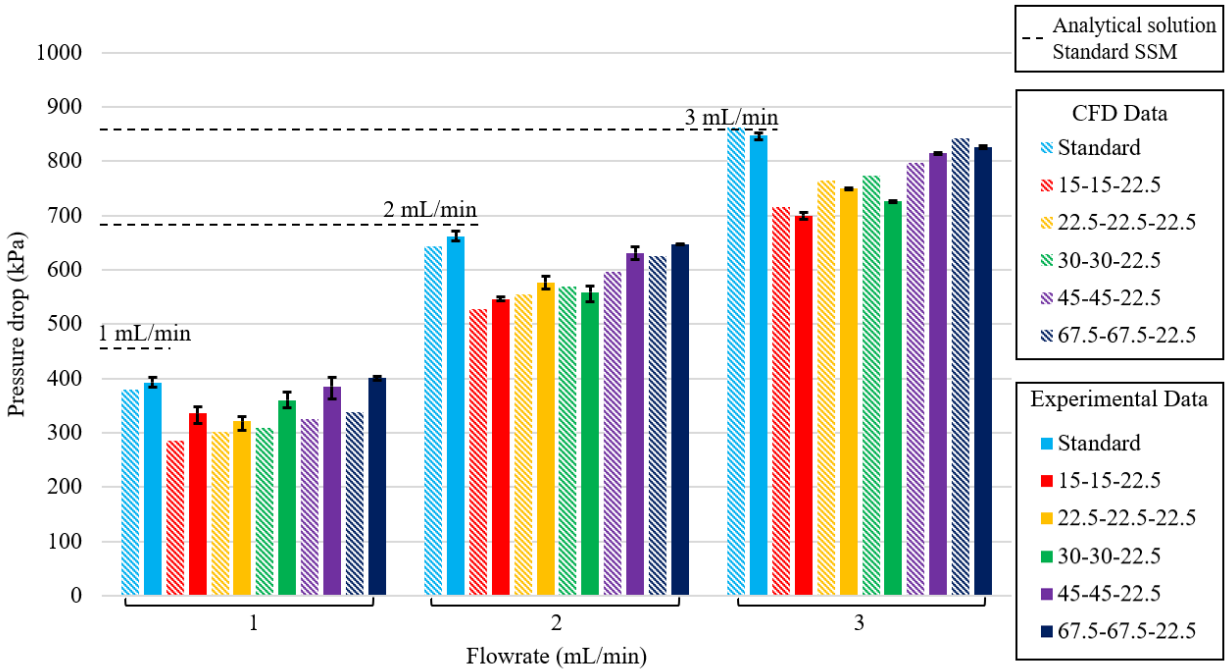

Figure 2.12: The experimental and CFD pressure drops for the Impeller SSM and standard SSM at a flow rate of 1, 2, and 3 mL/min. The dashed black line is the expected pressure drop for the standard SSM predicted by Equation (2.3).

The reduction in experimental measured pressure drop for each Impeller SSM configuration ranged between 1.8% and 18.2%. Overall, the 15-15-22.5 Impeller SSM configuration showed the most improvement with an average pressure drop reduction of 16.4% for three flow rates. The 22.5-22.5-22.5 configuration is the next best at 14.1% reduction in pressure drop. The 45-45-22.5 and 67.5-67.5-22.5 configurations only showed marginal

improvement over the standard SSM with an average of 3.3 and 2.3% reduction in pressure drop respectively. Reducing the pressure drop in the Impeller SSM will reduce the amount of power needed to create fluid flow.

2.9.2 CFD Analysis of Mixing and Internal Flow

The 15-15-22.5, 22.5-22.5-22.5 and 30-30-22.5 Impeller SSM configurations had the best experimental reduction in pressure drop compared to the standard SSM. The CFD data is compared between the standard SSM and these three Impeller SSM configurations to gain insight of mixing and flow characteristics.

Figure 2.13 shows a comparison of the contour plots of the volume percent of Part A and Part B over cross sections at the mixer inlet and the center of the first four SSM elements for the standard SSM and the 15-15-22.5, 22.5-22.5-22.5 and 30-30-22.5 Impeller SSM configurations at a volumetric flow rate of 2 mL/min. The red regions are alkoxysilicone Part A, the blue is alkoxysilicone Part B, the green is fully mixed alkoxysilicone, and the intermediate colors are the other varying degrees of mixing. The plots indicate a similar level of mixing performance for all four static mixers.

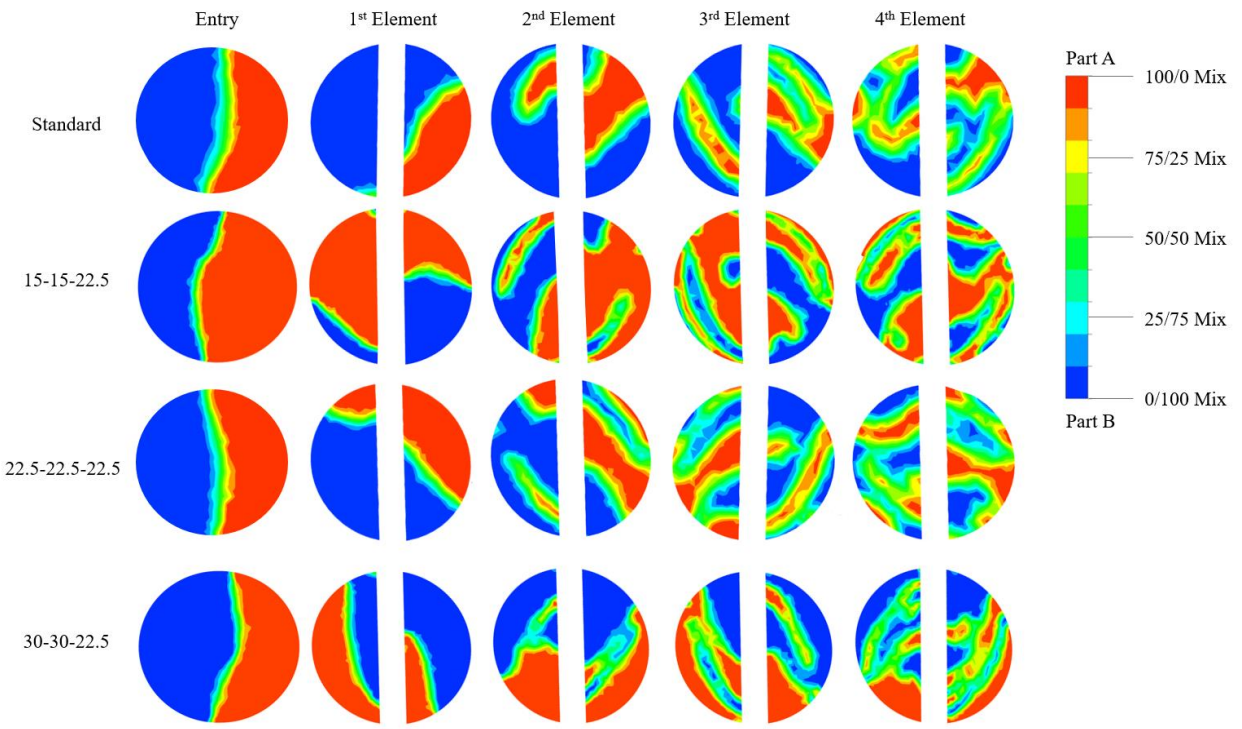

Figure 2.13: Volume percent of Part A (red) and Part B (blue) components at cross sections located at the inlet and the center of the first four elements (see Figure 2.7(d)) of the standard SSM, top row, and three best Impeller SSM configurations. The green color indicates fully mixed alkoxysilicone.

Figure 2.14 shows the 3D velocity magnitude fields from CFD simulations run at 2 mL/min volumetric flow of alkoxysilicone for the standard SSM (Figure 2.14(a)) and the three best performing Impeller SSM configurations: 15-15-22.5 in Figure 2.14(b), 22.5-22.5-22.5 in Figure 2.14(c), and 30-30-22.5 in Figure 2.14(d). The junctions between SSM helical elements are circled to highlight the improvements that the Impeller SSM makes to the internal fluid flow patterns, compared to the standard SSM, by reducing the interferences at the helix junctions. The standard SSM flow has noticeably larger areas that have very slow to stagnant flow (the blue areas) in comparison to the Impeller SSM configurations. Additionally, for all the flows in the Impeller SSM configurations, there are relatively uninterrupted streams of high velocity (red

colored) flow indicating that the Part A and Part B alkoxysilicone fluids are traveling and mixing through the SSM efficiently.

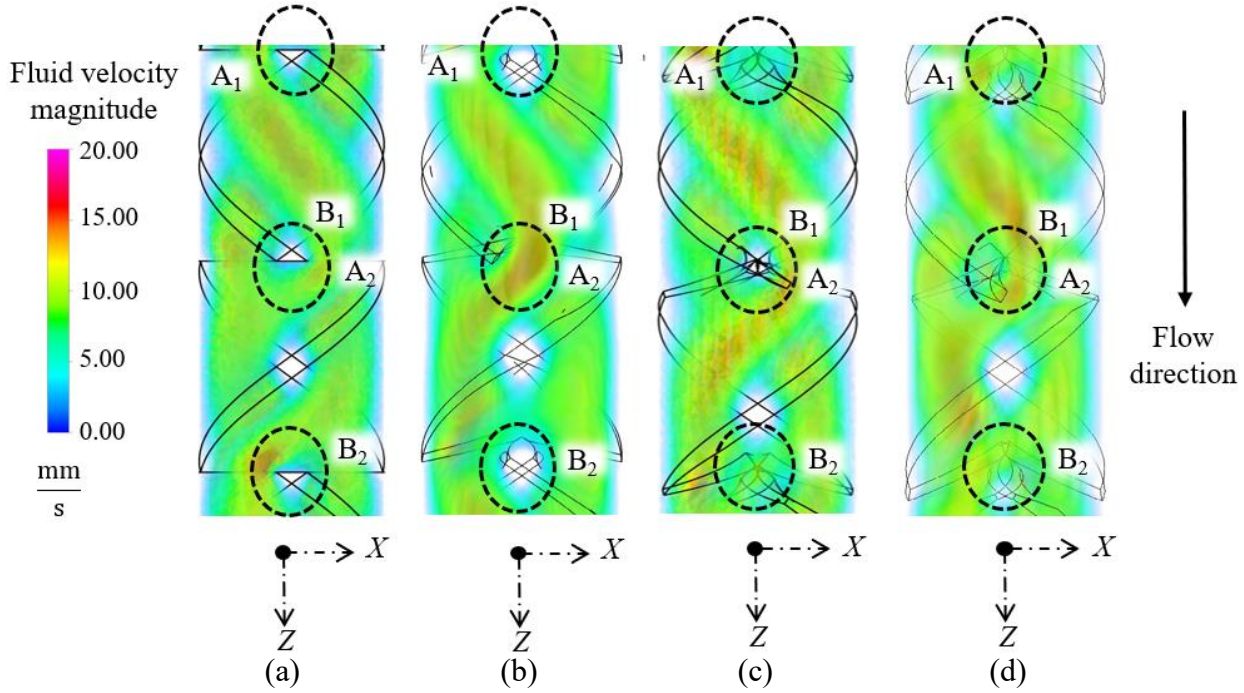

Figure 2.14: Side view of the 3D velocity magnitude fields for (a) the standard SSM, and (b) 15-15-22.5, (c) 22.5-22.5-22.5, and (d) 30-30-22.5 Impeller SSMs. The circled areas indicate the junctions between two helical elements.

A close-up isometric view of the B_2 junction of helical element shows the region at the top of the next element. For the standard SSM, Figure 2.15(a), the area has a noticeable slow flow (blue color) indicating that a significant impedance to the fluid flow exists in this area. The same region on the three best performing Impeller SSMs, Figure 2.15(b)-(d), indicates relatively little fluid interference, as shown by the green color that is prominent in the B_2 junction region.

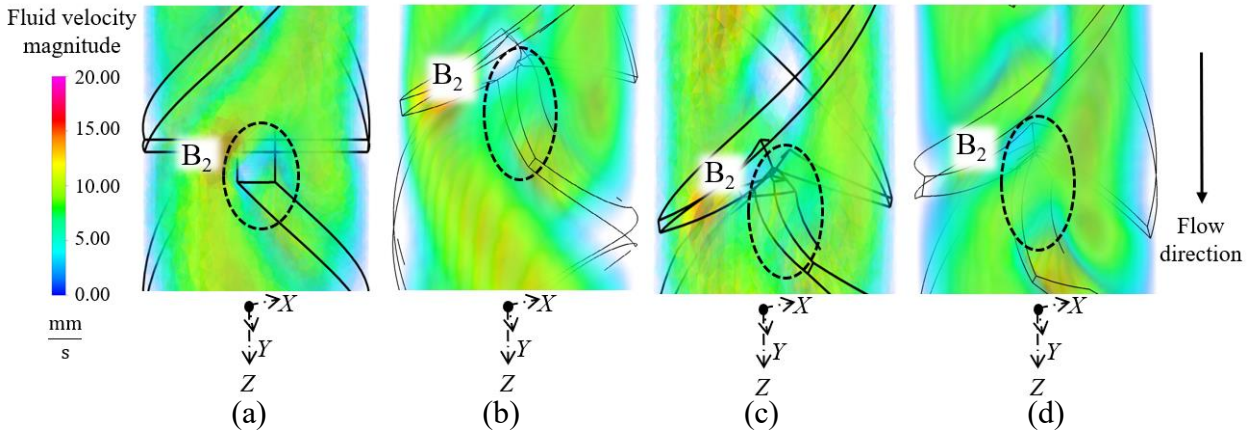

Figure 2.15: Isometric view of the B_2 interface on the (a) standard SSM, (b) 15-15-22.5, (c) 22.5-22.5-22.5, and (d) 30-30-22.5 Impeller SSMs.

The effect of the Impeller SSM geometry on the fluid flow can also be seen in the fluid velocity contour plots that lies on the central *x*-*z* plane as shown in Figure 2.16. The high flow areas (green and yellow) for the15-15-22.5 Impeller SSM in Figure 2.16(b), are much larger and more continuous than those of the standard SSM in Figure 2.16(a). Additionally, the abrupt stop of the high flow areas that is seen at the junction between two helical elements for the standard SSM does not occur for the Impeller SSM. This is again an indicator of the reduced impedance to the flow by the Impeller SSM helix. This behavior is also seen in the 22.5-22.5-22.5 and 30-30-22.5 Impeller SSMs in Figure 2.16(c) and (d), respectively.

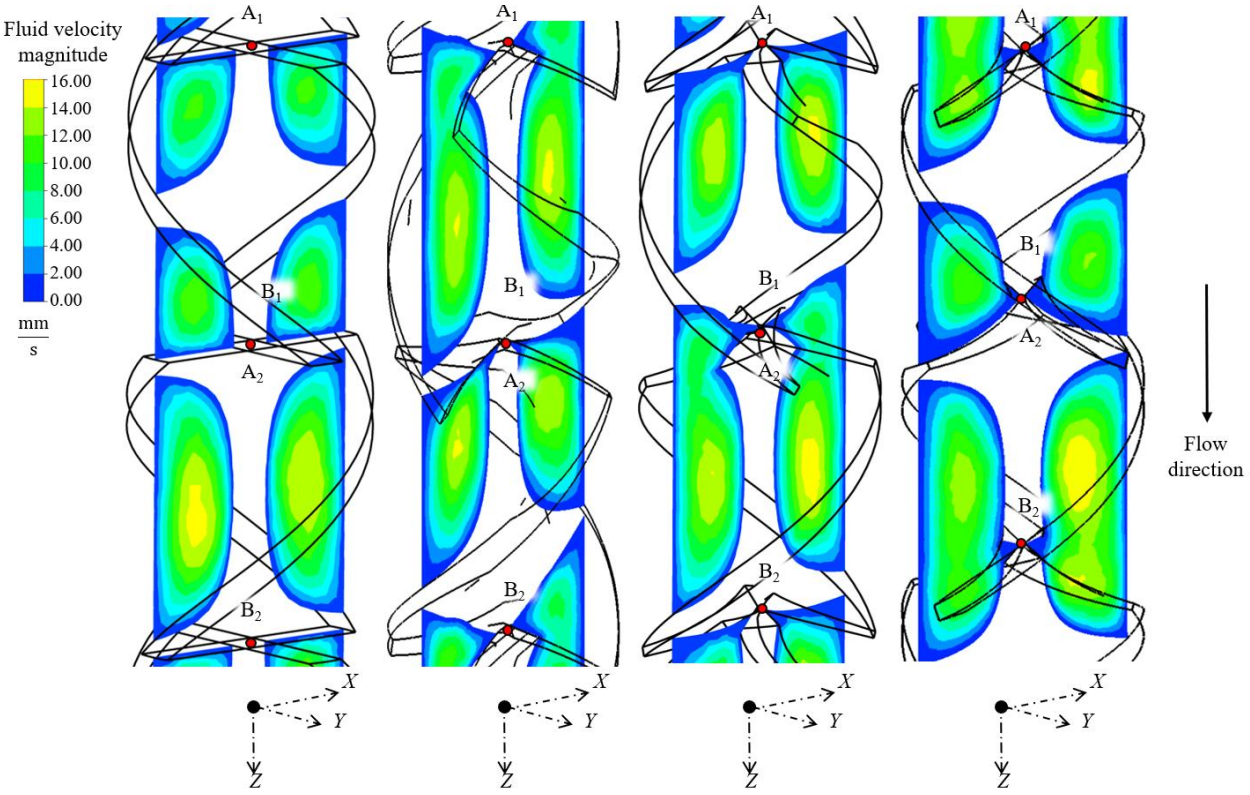

Figure 2.16: Velocity contour plots on the central *x*-*z* plane of the (a) standard SSM, (b) 15-15-22.5, (c) 22.5-22.5-22.5, and (d) 30-30-22.5 Impeller SSMs. The three Impeller SSM configurations have a larger and more continuous fluid flow regions than those of the standard SSM.

Inspection of the CFD data for the 67.5-67.5-22.5 Impeller SSM configuration reveals why it did not have as large of pressure drop reduction as other Impeller SSMs. The circled regions show the fluid flow having low flow velocity, indicating a choke point. This choke point is created by the extra height and twist of the release winglet getting too close to the next mixing element's taper inlet. This behaviour was also noticed in the 45-45-22.5 Impeller SSM as well.

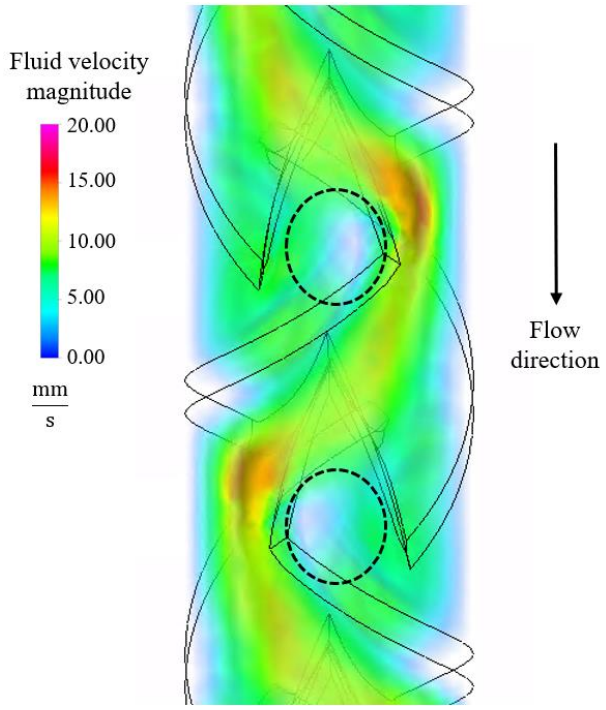

Figure 2.17: Choke point created by the release winglet and taper inlet of the 67.5-67.5-22.5 Impeller SSM.

2.10. Conclusions and future work

The Impeller SSM, inspired by a centrifugal pump impeller, adds advanced features to the standard SSM design, , which result in a reduction in pressure drop as demonstrated both experimentally and computationally. Experiments showed that the Impeller SSM design could lower the pressure drop by up to 18.2% compared to a standard SSM design. CFD data showed improvements as high as 20%. The 15-15-22.5 Impeller SSM configuration was the experimentally tested configuration with the best performance, with a pressure drop reduction of 16.4%, averaged over three flow rates. The second best SSM configuration, 22.5-22.5-22.5, had an average pressure drop reduction of 14.1%. The 45-45-22.5 and 67.5-67.5-22.5 SSM configurations showed the least improvement over the standard SSM, with a 3.3 and 2.3% pressure drop reduction, respectively. This reduction in performance is likely due to a choke point in flow pattern. CFD analysis show similar mixing patterns between Part A and Part B components in the first four elements of the Impeller SSMs compared to the standard SSM.

The Impeller SSM features responsible for the reduction in pressure drop are the taper inlet, release winglet, and the transfer angle created by the α, β, and γ angles. The taper inlet is a sharp angle on the helix inlet edges and serves two primary purposes. The first is to promote fluid recombination on each side of the helix, reducing the low fluid velocity, or dead zone, that is created at the inlet of a standard helix. The second purpose of the taper is to reduce the drag created by the bottom release winglet of the helix as it splits the fluid flow. The flat bottom edge of the helix found in the standard SSM is replaced by another sharp taper angle, creating the release winglet that cuts the flow, reducing losses. The release winglet, created by the release angle, directs the fluid flow from the prior helix into the next helix without abrupt flow interruptions. The transfer angle, found on both on the bottom and top of the helix, reduces the abruptness of the fluid flow transfer by acting as a knife-edge splitting the fluid flow. There appears to be a limit to the improvements offered by this design concept. Large angle taper inlets and release winglets will start to create choke points limiting pressure drop reduction as seen in the 67.5-67.5-22.5 and 45-45-22.5 Impeller SSMs.

The α, β, and γ features of the Impeller SSM create undercuts that would be difficult to fabricate using traditional manufacturing processes such as molding or machining. The SLA additive manufacturing process was used for the new SSM design at a material cost of $1.05 per part, which is comparable to the cost to purchase commercially available SSMs, demonstrating how additive manufacuting can be used to produce novel static mixer designs at a similar cost to standard designs. The Impeller SSM introduced in this study could be applied to any mixing application that a standard SSM of the same size could. The reduced pressure drop of the Impeller SSM requires less energy, improving process efficiency, and allowing the use of smaller, less expensive pumps in industrial applications.

Due to the capability of SLA technology in producing parts with geometric variations, future work can focus on a more detailed study the effects of the design parameters of Impeller SSM on pressure drop, leading to an optimized design. This method can also be applied to the development of other novel static mixer designs. Additional efforts can also be applied to quantitatively validating the mixing properties of the static mixer designs.

Chapter 3. Modeling of Transient Fluid Flow in Direct Ink Write Additive Manufacturing using the Characteristic Method

3.1. Abstract

The transient flow inside a direct ink write (DIW) system is characterized using the continuity and momentum equations. New frictional models describing the fluid flow of a viscous non-Newtonian fluid through both an impeller spiral static mixer (ISSM) and a tapered nozzle are created for the momentum equation. Using the Characteristic Method (CM) and boundary conditions for the DIW system, the continuity and momentum equations are numerically solved. Using CM, the transient response of the DIW system with step changes to the input volumetric flowrate is modeled for both a tube and ISSM. The transient response of the DIW output volumetric flowrate is recorded using a doppler volumetric flow sensor and two pressure sensors and is found to match the CM model. CM is also used to predict the corner swelling of a 90-degree corner DIW tool path from trapezoidal motion planning with accelerations of 100, 250, 500, 1000, 1500, and 2000 mm/s^2. The predicted corner swelling is matched with the actual corner swelling found through image processing of a 90-degree corner produced on a DIW system. The corner swelling is significant, ranging from 0.76 to 0.37 mm for a line width of 0.25 mm and a height of 0.15 mm. This study demonstrates that the CM can accurately predict the transient response of the DIW volumetric flowrate, which needs to be considered for accurate printing of the DIW system.

3.2. Introduction

Accurate process models for fluid deposition are needed to improve the quality of DIW. Previous DIW process models have either relied on experimental characterization or fitting parameters [22,48–51]. Transient fluid flow is a highly non-linear process that is affected by rheological, process, and geometrical parameters [52–54]. A common simplifying assumption for transient fluid flow is that there is no variation in flowrate which cannot be made for DIW systems due to the use of long static mixers and dispensing nozzles. Additionally while there are accurate empirical models relating to steady-state flow inside static mixers to the pipe flow [24], there is no literature establishing a similar relationship for the transient behavior of fluid in static mixers. Without the simplifying assumptions of no variation in flowrate or pipe flow, a generalized model using both the continuity and momentum equations that includes static mixers is needed to analyze the fluid flow in DIW.

In this chapter the continuity and momentum equations with frictional models for static mixers and tapered nozzles are discussed in Section 3.3. In Section 3.4 the characteristic mothed (CM) and the boundary conditions for DIW are described. The setup for experimental validation of the CM model is shown in Section 3.5 and the results are shown in Section 3.6. Lastly the conclusions of the study and discussion of future work is done in Section 3.7.

3.3. Transient Fluid Flow

The continuity and momentum equations of fluid dynamics and the frictional models to model the transient fluid flow in the PDP DIW system are presented.

3.3.1 Continuity and Momentum Equations

Based on a Reynolds transport theorem analysis of fluid flow inside a pipe, a series of generalized equations, the continuity and momentum equations, are derived [81]. The continuity and momentum equations are the basic equations of fluid dynamics [81]. The most common forms of the one-dimensional continuity equation, Equation (3.1), and the momentum equation, Equation (3.2), are [61]:

$$\frac{\delta P}{\delta t} + \frac{Q}{A}\frac{\delta P}{\delta x} + \frac{\rho a^2}{A}\frac{\delta Q}{\delta x} = 0 \tag{3.1}$$

$$\frac{1}{A}\frac{\delta Q}{\delta t} + \frac{Q}{A^2}\frac{\delta Q}{\delta x} + \frac{1}{\rho}\frac{\delta P}{\delta x} + g\sin\theta + F = 0 \tag{3.2}$$

where P is pressure, t is time, Q is the volumetric flowrate in the pipe, A is the pipes cross-sectional area, ρ is the fluid density, a is acoustic wave speed, x is the location along the central axis, g is gravity, θ is the angle of gravity relative to the central axis, and F is the frictional model for the system. The effect of transient flow is unidirectional, and only the one-dimensional forms of the continuity and momentum equation are needed [82]. This analysis accounts for compression of the fluid through the inclusion of a which is important for describing the transient behavior, more details on a are given in Appendix A.

In an one-dimensional system, the convective acceleration terms, $\frac{Q}{A}\frac{\delta P}{\delta x}$ and $\frac{Q}{A^2}\frac{\delta Q}{\delta x}$, and the gravitational term, $g\sin\theta$, can be ignored because they tend to be small in comparison to the other terms of the continuity and momentum equations [75,81]. Using this simplification, the continuity and momentum equations, as shown in Equations (3.3) and (3.4), are [81].

$$\frac{\delta \mathrm{P}}{\delta t} + \frac{\rho a^2}{A}\frac{\delta Q}{\delta x} = 0 \tag{3.3}$$

$$\frac{1}{A}\frac{\delta Q}{\delta t}+\frac{1}{\rho}\frac{\delta P}{\delta x}+F=0 \tag{3.4}$$

3.3.2 Friction Models

The friction model, *F*, for the fluid system plays a significant factor in determining fluid behavior in the continuity and momentum equations. A common friction model is the quasi steady-state friction model based on the Darcy-Weisbach Equation, Equation (3.5), that treats each finite length of fluid flow as steady-state and uses the local volumetric flowrate to calculate *F* [83]:

$$F=\frac{fQ|Q|}{2DA^2} \tag{3.5}$$

where f is the Darcy friction factor.

For DIW systems with pipe and laminar flow, f is found as [75]:

$$f=\frac{64\mu A}{\rho QD} \tag{3.6}$$

where μ is the fluid viscosity.

Empirical models for static mixers have established that pressure drop within a unit length of static mixer, ΔP_{sm}, is proportional to the pressure drop within a unit length of a pipe, ΔP_{pipe}, for a given flow and expressed using the parameter K_l [24]:

$$K_l=\frac{\Delta P_{sm}}{\Delta P_{pipe}} \tag{3.7}$$

K_l can be included in a modified Darcy friction factor f_{mod}.

$$f_{mod}=K_l f \tag{3.8}$$

The static mixers used in this study is a variant of the spiral static mixer design, the impeller spiral static mixer (ISSM) developed by the authors, which have a K_l of 5.5 [84].

For transient flows that are transferring between steady states without oscillations, a quasi-steady-state friction model will accurately predict the flow behavior because the dampening effect of local and convective acceleration have an insignificant impact on flow behavior [85]. With the quasi-steady-state assumption for transient flow behavior, it is possible to expand the continuity and momentum equations to include static mixers using Equation (3.8), since the steady-state flow behavior is similar to the pipe flow.

This quasi-steady-state assumption for *F* allows for the inclusion of more complex forms of fluid flow, such as non-Newtonian flow and tapered pipe flow, in which the common mathematical relationships rely on the assumption of steady-state flow. Both of which are relevant to DIW since most systems dispense polymers, which typically are shear-thinning fluids, through fine-tipped tapered nozzles.

For non-Newtonian fluids viscosity, μ_{eff}, is modeled using the power law [75].

$$\mu_{eff} = kG'^{n-1} \tag{3.9}$$

where *k* is the fluid constancy index, *n* is the flow behavior index, and G' is the shear rate experienced by the non-Newtonian fluid, and G' is given by Equation (3.10):

$$G' = K_g {}^{Q}/_{DA} \tag{3.10}$$

where K_G is the pipe shear constant. For the pipe and ISSM flow, the value of K_G is 8 and 28, respectively [24].

Substituting Equations (3.6)-(3.9) into Equation (3.5) gives a single equation for *F* includes the effects of a static mixer and a non-Newtonian fluid.

$$F = \frac{128K_l k \left(K_g {}^{Q}/_{DA}\right)^{n-1} |Q|}{\rho \pi D^4} \tag{3.11}$$

For tapered nozzles, K_l is derived in the same manner as it is for static mixers. The steady-state ΔP_{pipe} as shown in Equation (3.5) can be used to derive the pressure drop in a tapered nozzle ΔP_{taper}.

A tapered nozzles diameter D_{taper} varies linearly along its length, L_{taper}, according to Equation (3.12).

$$D_{taper} = D_{in} + (D_{out} - D_{in})\frac{x}{L_{taper}} \tag{3.12}$$

where *x* is the positional location along the tapered nozzle length, D_{in} is the inlet diameter, and D_{out} is the outlet diameter.

Taking the derivative of both Equations (3.5) and (3.12) results in Equations (3.13) and (3.14).

$$\frac{dD_{taper}}{dx} = \frac{(D_{out} - D_{in})}{L_{taper}} \tag{3.13}$$

$$\frac{dP}{dx} = \frac{128\mu Q}{\pi D_{taper}(x)^4} \tag{3.14}$$

Substituting Equation (3.13) into Equation (3.14) to eliminate dx,

$$dP = \frac{-128\mu L_{taper} Q}{\pi(D_{out} - D_{in})}\frac{dD}{D_{taper}(x)^4} \tag{3.15}$$

and then integrating both sides along the length of the tapered nozzle

$$\Delta P_{taper} = \frac{-128\mu L_{taper} Q}{\pi(D_{out} - D_{in})}\left(\frac{1}{3{D_{in}}^3} - \frac{1}{3{D_{out}}^3}\right) \tag{3.16}$$

which using Equation (3.7) gives

$$K_l = \frac{-D_{in}}{(D_{out} - D_{in})}\left(\frac{1}{3{D_{in}}^3} - \frac{1}{3{D_{out}}^3}\right) \tag{3.17}$$

Repeating the steps shown in Equations (3.12)-(3.17) but also using the power-law Equation, Equation (3.9), gives the following:

$$\Delta P_{taper} = \frac{128kL_{taper}Q}{3\mathrm{n}(D_{out}-D_{in})}\left(\left(3\pi {D_{out}}^3\right)^{-n} - \left(3\pi {D_{out}}^3\right)^{-n}\right)\left(K_g Q\right)^{\mathrm{n}-1} \tag{3.18}$$

$$K_l = \frac{-D_{in}\left({D_{in}}^{3n} - {D_{out}}^{3n}\right)}{3\mathrm{n}(D_{in}-D_{out}){D_{out}}^{3\mathrm{n}}} \tag{3.19}$$

3.4. Using the Characteristic Method to solve the Continuity and Momentum Equations

There are several numerical methods available to solve Equations (3.3) and (3.4). Due to its ease of implementation and numerical stability, the CM was selected [81]. The implementation and the appropriate boundary conditions for the PDP DIW system are discussed.

3.4.1 Characteristic Method

CM turns Equations (3.3) and (3.4) into ordinary differential equations using a linear combination of Equations (3.3) and (3.4) and the total derivatives of Q and P, resulting in Equations (3.20) and (3.21) [81].

$$\frac{dQ}{dt} \pm \frac{A}{a\rho}\frac{dP}{dt} + AF = 0 \tag{3.20}$$

$$\frac{dx}{dt} = \pm a \tag{3.21}$$

Equations (3.20) and (3.21) are the mathematical representation of the disturbance at a point traversing in a fluid through both time, t, and space, x, along characteristic lines created by Equation (3.21), as illustrated in Figure 3.1. For every step in time, t_i, in the CM, an interior point, A, is connected by two characteristic lines to two adjacent points, B and C, from the preceding time step, t_{i-1}. The numerical solution to Equations (3.20) and (3.21) are shown in Equations (3.22) and (3.23), which use the P at points B and C in the previous time step to find Q and P at point A [81].

$$Q_{i,j} = Q_{i-1,j-1} + \frac{AP_{i-1,j-1}}{a\rho} - F_{i-1,j-1}\Delta t + \frac{AP_{i,j}}{a\rho} \tag{3.22}$$

$$Q_{i,j} = Q_{i+1,j-1} - \frac{AP_{i+1,j-1}}{a\rho} - F_{i+1,j-1}\Delta t + \frac{AP_{i,j}}{a\rho} \tag{3.23}$$

The ratio of the time steps, Δt, and the length steps, Δx, is the same as a

$$\pm a = \frac{\Delta x}{\Delta t} \tag{3.24}$$

Combining this iterative procedure with boundary conditions to solve for the exterior points creates a characteristic grid of fluid pressure and speed at every length step and time step, as shown in Figure 3.2. A complete explanation of the CM and its mathematical implementation can be found in [81].

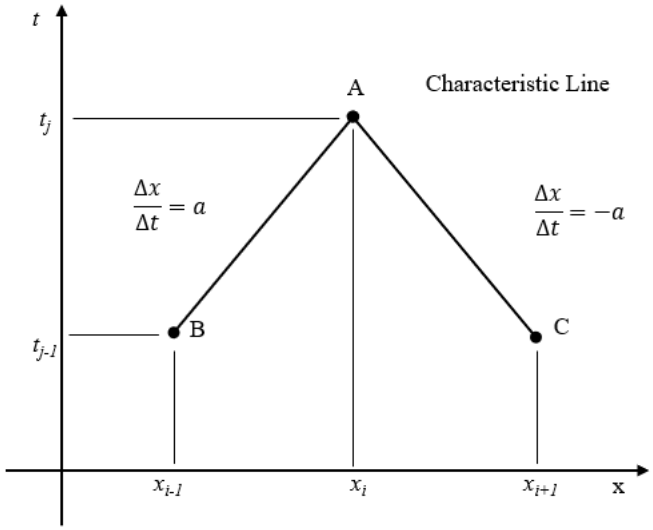

Figure 3.1: Disturbances propagated forward and backward in time and space along the characteristic lines.

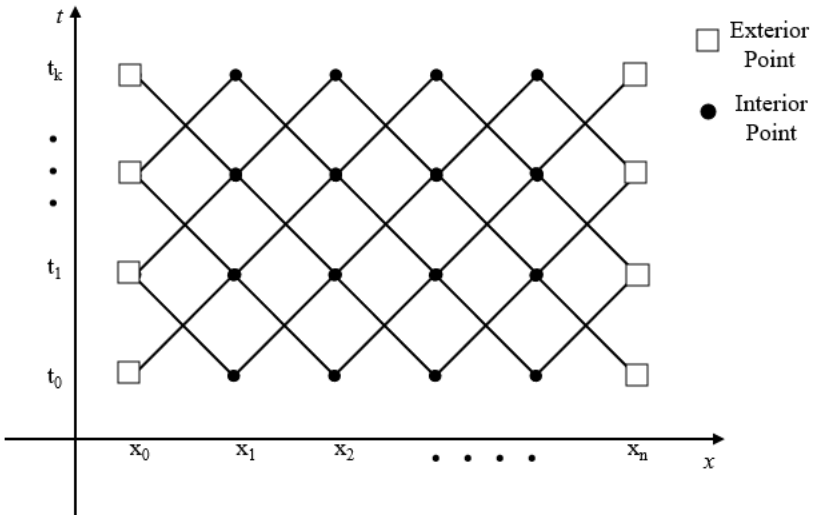

Figure 3.2: Characteristic grid using boundary conditions, Equation (3.20), and Equation (3.21) to solve for the fluid pressure and speed.

3.4.2 Boundary Conditions

The DIW system used in this study is a PDP for which the boundary conditions are constant pressure outlet and a volumetrically controlled inlet.

3.4.2.1 Constant Pressure Outlet

The constant pressure outlet boundary condition assumes that the pressure of the outlet, $P_{i,outlet}$, is held constant at gauge pressure. Using $P_{i,outlet}$, $P_{i-1,n-1}$, and $Q_{\mathrm{i-1,k-1}}$ and based on Equation (3.22), the volumetric outlet flow, $Q_{i,outlet}$, can be found:

$$Q_{i,outlet} = Q_{\mathrm{i-1,k-1}} + \frac{AP_{\mathrm{i-1,k-1}}}{a\rho} - AF\Delta t - \frac{AP_{i,outlet}}{a\rho} \tag{3.25}$$

where *k* is the total number of length steps used in the CM.

3.4.2.2 Volumetric Flow Controlled Inlet

The volumetric flow controlled inlet boundary condition assumes that the flowrate of the inlet, $Q_{i,inlet}$, can be varied according to an arbitrary time function.

$$Q_{i,inlet} = Q(t) \tag{3.26}$$

Using $Q_{i,inlet}$, $P_{i-1,2}$, and $Q_{i-1,2}$ the inlet pressure, $P_{i,inlet}$ can be found using Equation (3.27).

$$P_{i,inlet} = a\rho A\left(Q_{i,inlet} - Q_{\mathrm{i}-1,2} + \frac{P_{i-1,2}}{a\rho} + F\Delta t\right) \tag{3.27}$$

3.5. Transient Fluid Simulation and Experiments

The open-source one-dimensional water hammer code by Jensen et al. is adopted to simulate the transient flow in DIW systems [59]. The code uses CM to solve the transient fluid problem and was modified to allow for the boundary conditions needed to simulate the DIW. The modification includes new frictional terms for an ISSM and tapered nozzle and to allow for vectorization of the solver to improve its computational efficiency. CM is evaluated by modeling the step response of a DIW system in a two-step response test. The two-step response test will validate the CM's ability to predict DIW characteristics using pressure and volumetric output data measured during testing. Experimentally, a specific DIW tool path with a 90-degree turn is used to measure the shape of the deposited material and demonstrate the CM's ability to predict DIW behavior.

3.5.1 DIW system

The DIW system used for this study is a custom-built machine, Figure 3.3, that is based on the CoreXY machine design that is able to handle the weight of the PDP [86,87]. The DIW machine consists of a carriage system, a movable print bed, and a precision PDP for dispensing the viscous fluids for DIW. The carriage system controls the X and Y position of the dispensing nozzle and PDP using timing belts driven by two stepper motors. The print bed driven by two lead screws controls the Z position of the print bed.

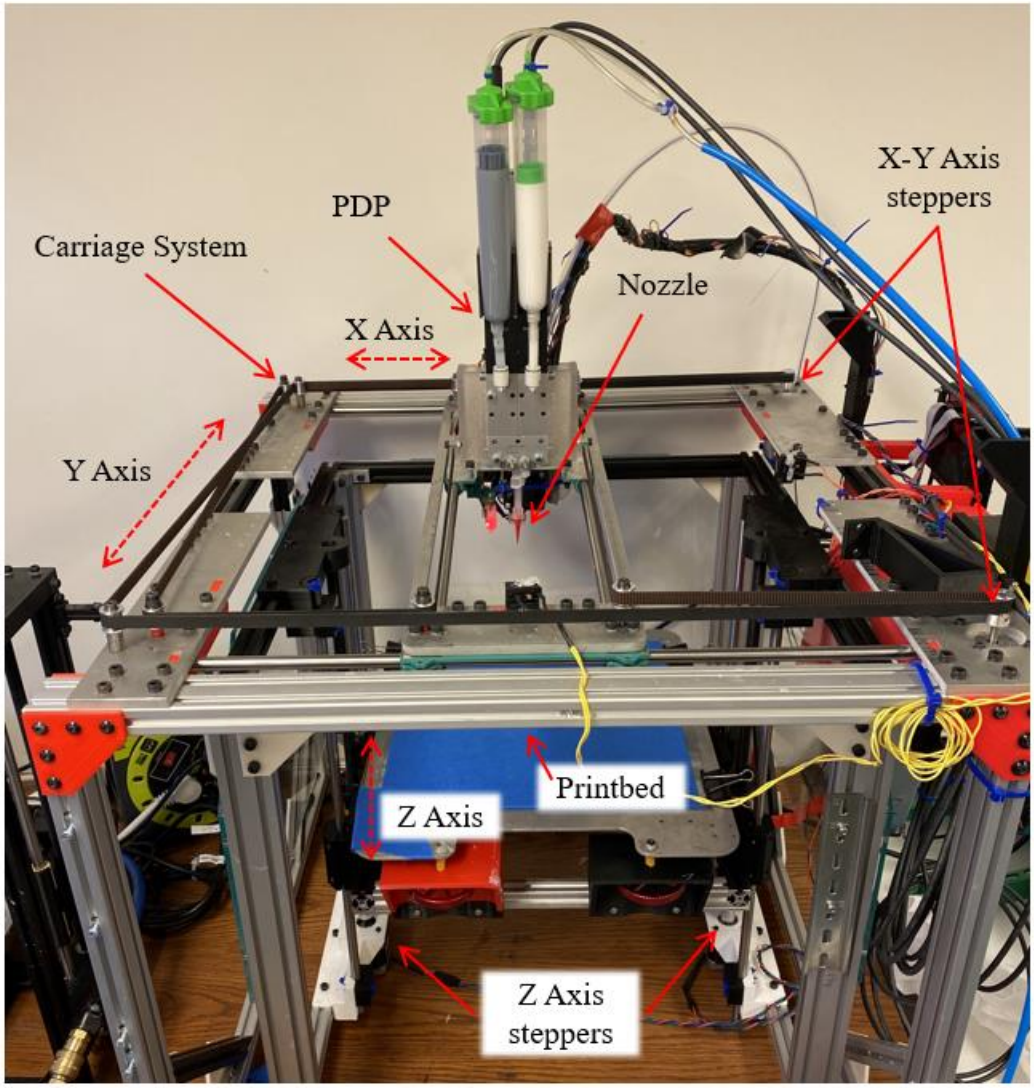

Figure 3.3: The custom-built DIW system with the CoreXY carriage system that moves the PDP and the lead screw Z-axis that moves the print bed.

3.5.2 PDP

For this DIW system, the PDP is a dual progressive cavity pump (Vipro-Head 3/3, Viscotec, Toeging am Inn, Germany), as shown in Figure 3.4(a). Two stepper motors drive two progressive cavity pumps that use a rotor to force fluid through fixed cavities, creating a well-

controlled and precise volumetric flow with minimal pulsing [79]. Two progressive cavity pumps enable the PDP to dispense two fluids simultaneously into a pipe or an ISSM for mixing. The output of the ISSM enters a tapered nozzle. The flow created by the PDP corresponds with the volumetrically controlled inlet boundary condition, and the nozzle tip corresponds to the constant pressure outlet boundary conditions described in Section 3.2. The ISSM, Figure 3.4(b), is a new type of spiral static mixer created to reduce the pressure drop in comparison to a standard static mixer of equivalent size and length [84]. In this study, the ISSM has an L of 50 mm and D of 3 mm. At the end of the ISSM is a tapered nozzle with an L of 20 mm, D_{in} of 3 mm, D_{out} of 0.25 mm. The ISSM has a series of alternating clockwise and counterclockwise mixing elements with tapers and winglets, Figure 3.4(c), that allow fluid to flow more efficiently through the mixing elements.

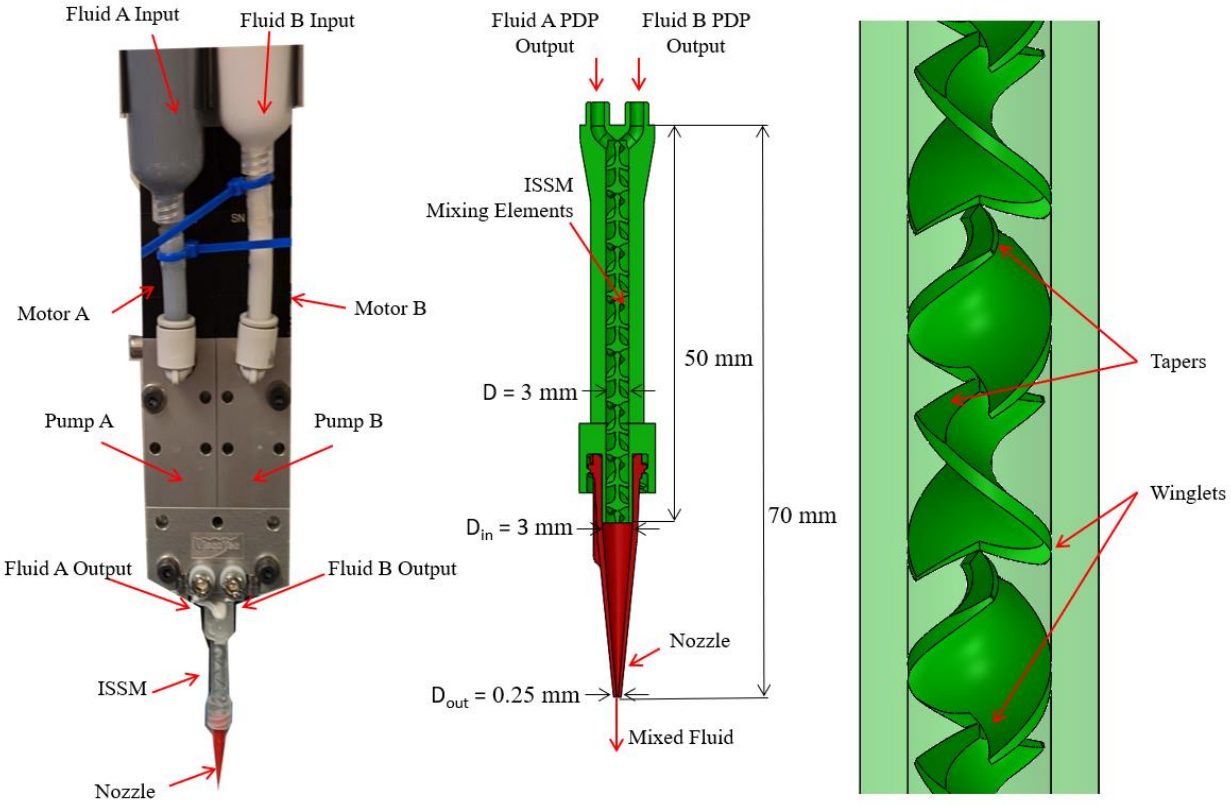

(a) (b) (c)

Figure 3.4: (a) PDP with an ISSM and fine tip nozzle along with (b) a section view of the ISSM and nozzle and (c) close-up view of the ISSM showing the mixing elements.

3.5.3 DIW Fluid Properties

The fluid for the DIW modeling and experiments is a two-part alkoxysilicone (Dow Inc. Midland, MI, USA) when mixed, has a k of 650 Pa-s^n, n of 0.6, ρ of 1295 kg/m^3, and a of 880 m/s as provided by Dow. It is the same fluid as discussed in section 2.5.2.

3.5.4 Two-step Response CM Model

A two-step response test is conducted to demonstrate the CM's ability to predict the output fluid flowrate and characterize the PDP DIW system. The two-step response test includes two step changes to the input fluid flowrate performed on both a pipe and an ISSM. Starting with zero input volumetric flow, the input volumetric flowrate is stepped to a higher flowrate, held for a period of time, and then stepped down to no flow again. The pressure and volumetric flowrate during the experimental two-step response tests were measured to verify the CM modeling results.

In this study, the input fluid flowrate is initiated at 0 mL/min and stepped to 1 mL/min. The fluid flow is maintained for 3.2 s and then step-changed back to 0 mL/min. The test is allowed to run for a further 1.7 s for a total test time of 5 s.

To simulate the transient fluid flow using the CM, the following ten parameters are needed: k, n, ρ, a, L, D, K_g, K_l, ΔX, and Δt. In this study, the step response test the fluid properties (k, n, ρ, and a) are the same as described in Section 4.3 and used for both the pipe and ISSM two-step response tests. The pipe and ISSM both have an L of 160 mm and D of 3 mm. The K_g is 8 for pipe and 28 for ISSM [24]. The pipe and ISSM have a K_l of 1 and 5.5, respectively [84]. Grid independence testing [59] showed that the pipe CM should use a ΔX of

$8x10^{-5}$ m (8000 nodes) and a Δt of $9x10^{-8}$ s and the ISSM CM should use a ΔX of $4x10^{-5}$ m (4000 nodes) and a Δt of $4.5x10^{-8}$ s.

3.5.5 Two-step Response Experiment

The pipe and ISSM used for the experimental two-step response tests, as shown in Figure 3.5(a), had the same dimensions as in the CM simulation. Two piezoresistive pressure sensors (Model 24PCGFH6G, Honeywell Charlotte, NC, USA) were placed at the fluid inlet and near the fluid outlet of the pipe or ISSM, Figure 3.5(b). A clamp-on ultrasonic Doppler volumetric flow sensor (Model FD-XS8, Keyence, Osaka, Osaka, Japan) measured the fluid flowrate. The pressure sensors were placed at the pipe and ISSM inlet (marked as Pressure Sensor #1) and 150 mm from the inlet (marked as Pressure Sensor #2), as shown in Figure 3.5. An op-amp circuit amplifies the signal from the pressure sensors with a gain of 10. The amplified pressure sensor signal and analog volumetric flow sensor signal were read by an Arduino microprocessor (Arduino Mega 2560 Rev3) at a 500 Hz sampling rate. The pressure sensors were calibrated against a pressure gauge (Model DPGA-07, Dwyer Instruments Michigan City, Indiana) using a custom pressure manifold. The volumetric flow sensor was zeroed against a pipe or ISSM filled with fluid but had no flow before every test to prevent signal drift. The pressure drop is defined as the difference in pressure from Pressure Sensor #1 to Pressure Sensor #2.

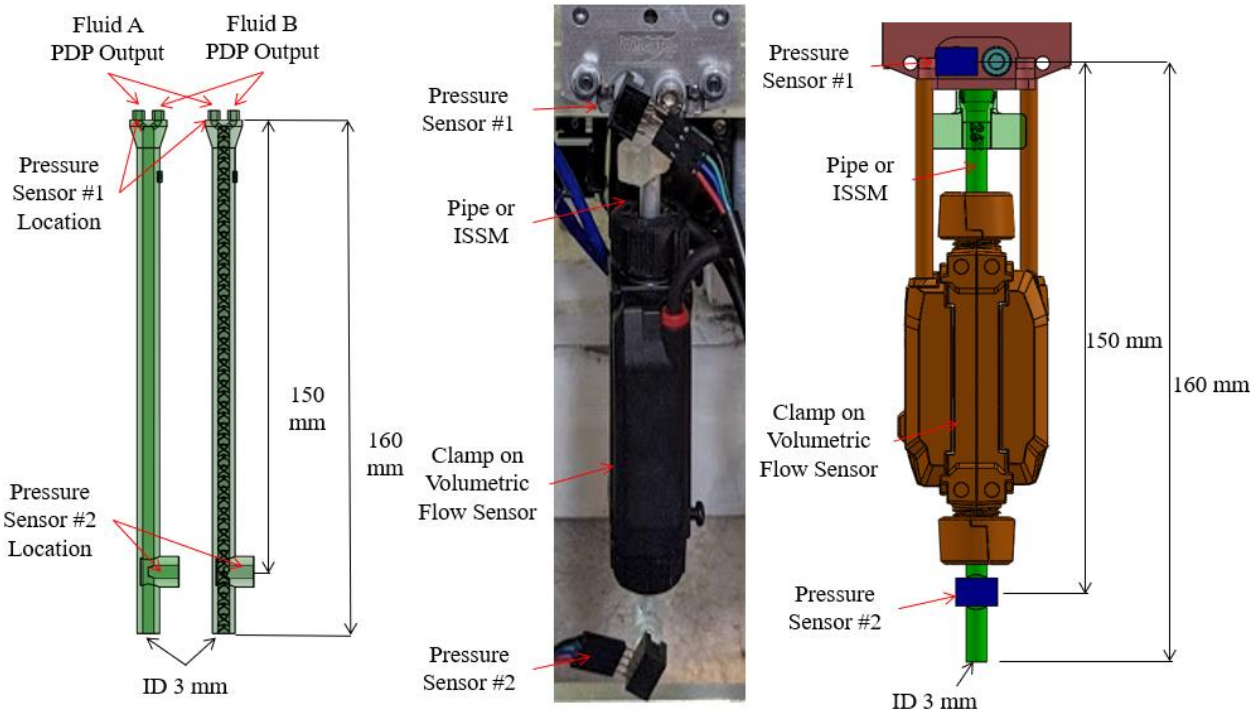

(a) (b) (c)

Figure 3.5: (a) Internal view of the pipe and ISSM used in the two-step response testing, (b) the PDP with two pressure sensors and a volumetric flow sensor to monitor experimental flow, and (c) the dimensioned experimental assembly.

The experimental two-step response test was repeated six times for both the pipe and the ISSM for a total of 12 tests. Noise from the volumetric flow sensor was filtered using a robust loess filter with a smoothing window of 0.1 s in Matlab™ (R2019B). Pressure sensor data was not filtered.

To compare the smoothed experimental volumetric output data to the modeled data, a Gompertz function [88] was fit to the first step of the two-step response tests using the Matlab Curve Fitting Toolbox™

$$G_{fit} = a_g e^{-b_g e^{-c_g t}} \tag{3.28}$$

where a_g is the asymptote, b_g is the displacement, and c_g is the growth rate [88]. Sigmoid functions like the Gompertz function are very efficient at quantifying data using very parameters[89].

In this application a_g represents the experimental steady-state value of the volumetric flowrate output data after the step input. b_g shifts the location of the function forward or backward in time, and while needed for the Gompertz function, it is not that important for this application because each test is set on a uniform time scale. c_g represents how quickly the output volumetric flowrate grew with respect to time, and it is important to quantify the difference between systems.

3.5.6 Simulating a DIW 90-degree Corner Tool path

The DIW system was used to print a single line with a 90-degree corner, Figure 3.6, a simple tool path feature that requires the system to experience acceleration and deceleration during its deposition. The print profile and corner swell of the 90-degree corner will be compared between the CM and experimental printing results.

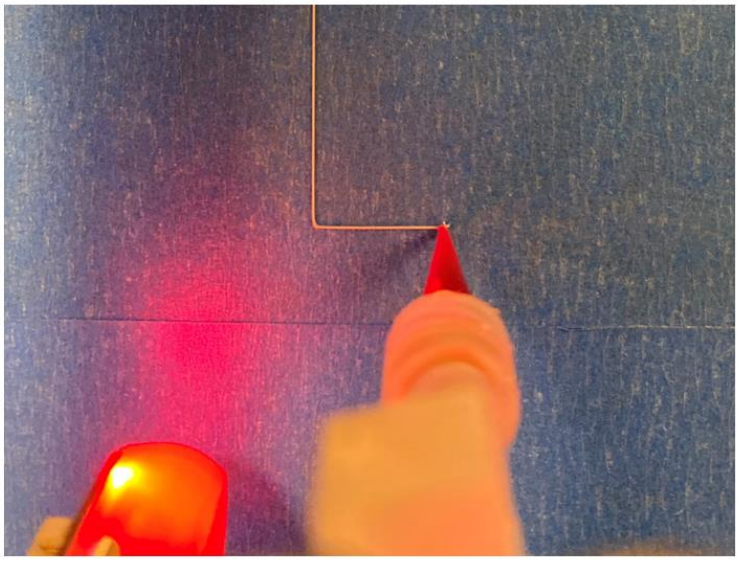

Figure 3.6: A 90-degree corner produced by the DIW system

The tool path for the 90-degree corner, followed by the center of the DIW nozzle, is shown in Figure 3.7. The ideal 90-degree corner will have a profile that is *w* wide along the entirety of the tool path. Point A is the beginning of the nozzle deceleration, point B is the point of minimum nozzle velocity and starting of acceleration, and point C is the end of the nozzle acceleration. At point B, there may be excess fluid deposited which causes corner swell [90]. The corner region, as defined by a distance equal to D_{out} from point B is shown in Figure 3.7, is denoted by the points A' and C'.

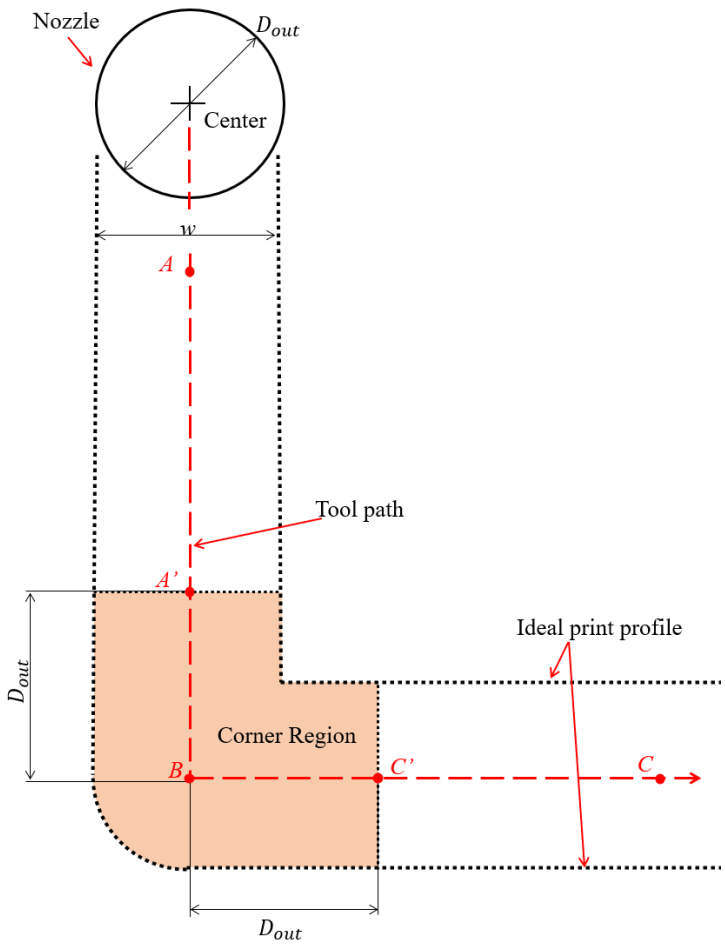

Figure 3.7: The tool path of the 90-degree corner

For the tool path outside of the corner region, the print nozzle is moving with a constant speed that the shape can be approximated as a rectangular prism where the width, w, is determined by the flowrate $Q_{i,outlet}$ (see Equation (3.25)), the nozzle velocity, v_i, and layer height, h_{layer}.

$$w = \frac{Q_{i,outlet}}{v_i h_{layer}} \text{ , } \forall\, i < i_{A'} \;||\; i > i_{C'} \tag{3.29}$$

To predict the size of the swelling at point B, it is assumed that the total material deposited during the path of the nozzle between points A' and C' is extruded outward in a

cylindrical shape with a layer height of h_{layer} [90]. The diameter of the swelling at point B, D_{swell}, is

$$D_{swell} = \sqrt{\frac{4\sum Q_{i,outlet}\Delta t}{\pi h_{layer}}}, \forall\, i_{A'} \leq i \leq i_{C'} \tag{3.30}$$

The DIW system is controlled with an open-source firmware (Marlin Firmware v1.1.9) that utilizes trapezoidal motion planning to determine the kinematics of the carriage system and the input flow for the PDP, using predefined velocity, acceleration, and a velocity limit (jerk) to print the 90-degree corner [90,91]. Jerk in the firmware is the maximum change in velocity where acceleration can be ignored by the firmware and not the time derivative of acceleration. In this study, the printed 90-degree corner has a theoretical width of 0.25 mm and a height, h_{layer}, of 0.15 mm under the steady-state condition. The DIW system had a velocity of 25 mm/s and a jerk of 2 mm/s. Six acceleration values are used in both the model and experimental tests: 100, 250, 500, 1000, 1500, and 2000 mm/s^2. An example of the tool path kinematics (speed and volumetric flowrate) from the trapezoidal motion planning with a 500 mm/s^2 acceleration for the 90-degree turn is shown in Figure 3.8.

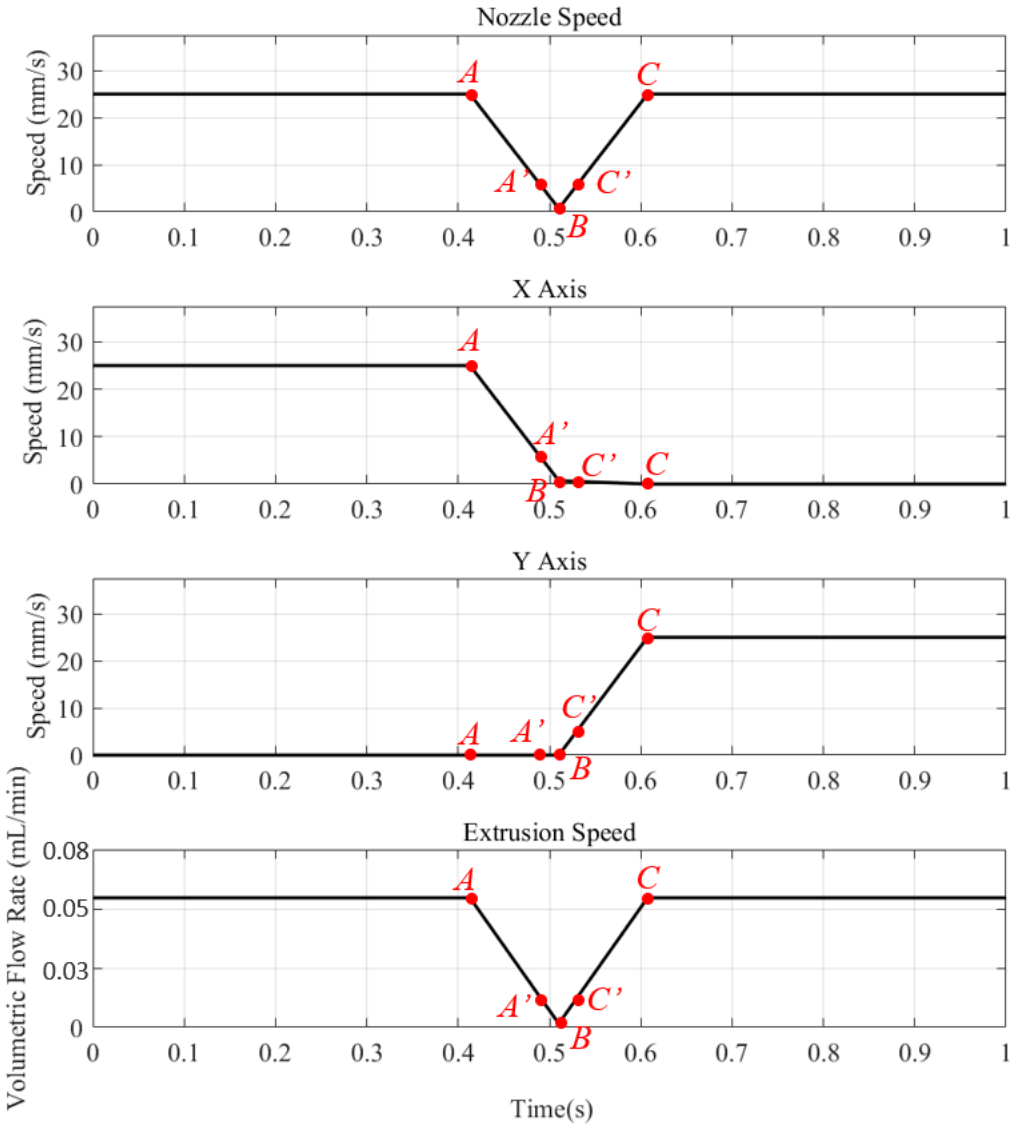

Figure 3.8: The kinematics of the DIW nozzle during the printing of a 90-degree corner with 500 mm/s2 produced using trapezoidal motion planning

The volumetric flowrate shown from the trapezoidal motion planning, as shown in Figure 3.8, is the input flowrate for the system used for both CM and the experimental tests. To simulate the transient fluid flow using CM, the following parameters are needed, k, n, ρ, a, L, D, K_g, K_l, ΔX, and Δt. In this study for the 90-degree corner test, the fluid properties (k, n, ρ, and a) are the same as the silicone described in Section 4.3. The CM used an ISSM with a length of 50 mm, D of 3 mm, K_l of 5.5, K_g of 28 [24,84]. The tapered nozzle has a length of 20 mm, a K_l of 52.4 as determined by Equation (3.19) using a D_{in} of 3 mm and D_{out} of 0.25 mm, and K_g of 8 [24]. The lengths of the ISSM and tapered nozzle are combined to give a L of 70 mm. Grid independence

testing showed that for this configuration, a Δx of 4x10^{-5} m (1750 nodes) and a Δt 4.5x10^{-8} s yield convergent results.

3.5.7 Printing a DIW 90-degree Corner Tool path

The experimental configuration for the printing of the 90-degree corner is the same, as shown in Figure 3.4. For each acceleration value, the experimental test was repeated five times for a total of 30 tests. After each test, a picture of the fluid deposition was taken by a digital microscope camera (UWT500X020M, AmScope Irvine California) placed directly over the point B. The microscope camera was calibrated with a caliper digital caliper (8000-F6, Products Engineering Corporation, Torrance, California).

The image from the microscope camera, Figure 3.9(a), is processed in Matlab™ (R2019B) to measure the print profile, tool path, and corner swell of the PDP DIW extrusion. The print profile consists of two lines, the outer print profile, $\overleftrightarrow{P}_{outer}$, and the inner print profile, $\overleftrightarrow{P}_{inner}$. The color image is turned into a binary image (im2bw) using the background color as the threshold value Figure 3.9(b), and image boundary detection (bwboundaries) the boundaries of the extrusion are found, Figure 3.9(c). The resulting boundary lines are smoothed with a 61st order Savitzky-Golay filter (sgolayfilt) using a frame length of 10 mm to define $\overleftrightarrow{P}_{outer}$ and $\overleftrightarrow{P}_{inner}$ without affecting the shape of the lines significantly, Figure 3.9(d).

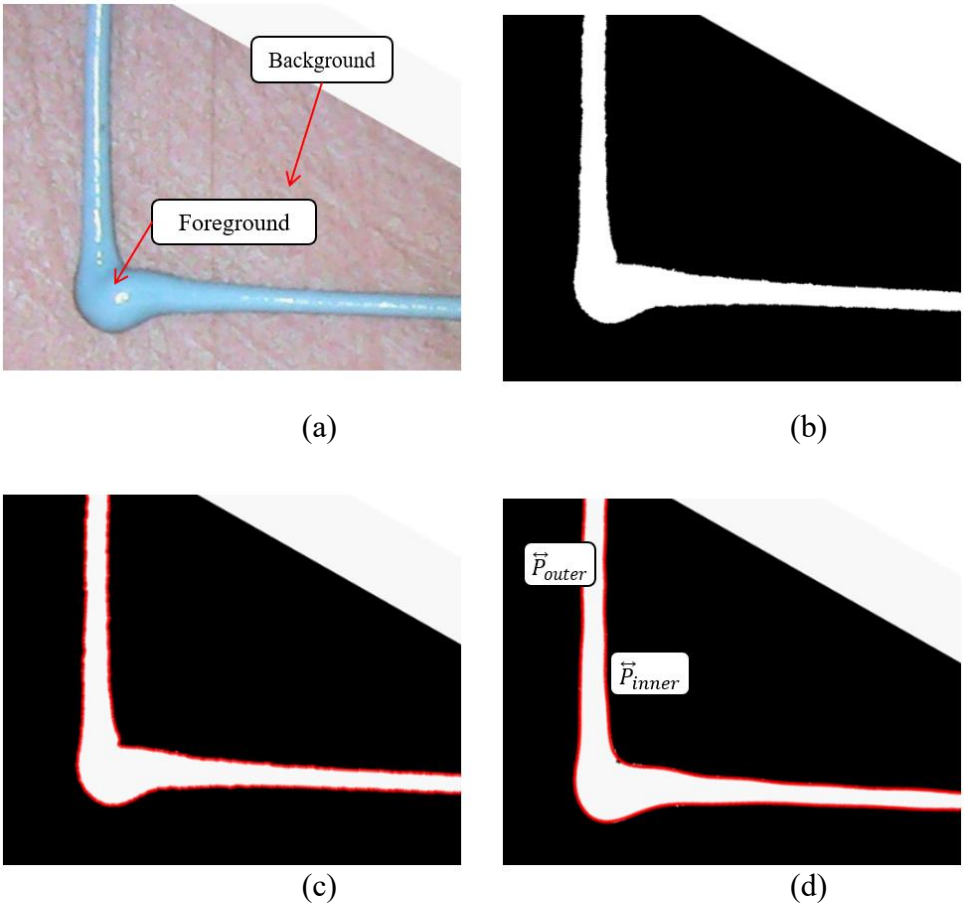

Figure 3.9: (a) The microscope image, (b) the binary image of the background and the foreground, (c) the edge detection of the binary image, and (d) the boundary lines smoothed using a Savitzky-Golay filter to create $\vec{P}_{outer}$ and $\vec{P}_{inner}$.

In Figure 3.10, two straight lines, $\vec{L}_{in}$ and $\vec{L}_{out}$, that represent the tool path of the PDP DIW and the Point B are found at the intersection of these two lines. Region A'' is manually chosen to start approximately 3 mm from the corner region before there is noticeable swelling on the tool path. On both sides of Region A'', two line segments of $\vec{P}_{outer}$ and $\vec{P}_{inner}$ are identified and averaged to create a straight line $\vec{L}_{in}$. This procedure is repeated for $\vec{L}_{out}$ by identifying Region C'', the area without noticeable swelling on the tool path after the 90-degree corner and two line segments of $\vec{P}_{outer}$ and $\vec{P}_{inner}$ in this region. The intersection of $\vec{L}_{in}$ and $\vec{L}_{out}$ defines the location of the point B.

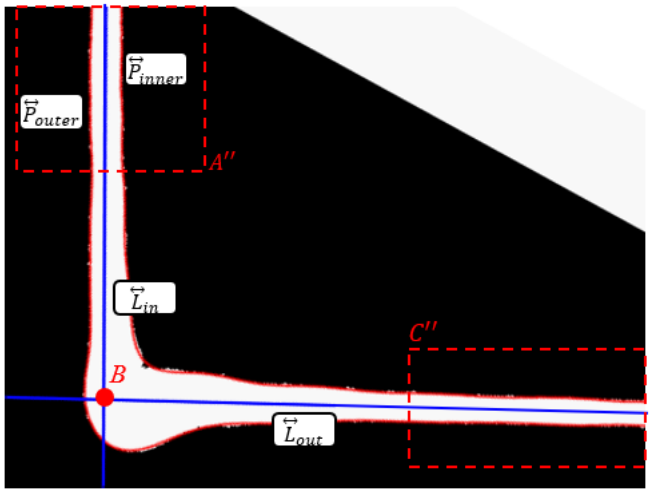

Figure 3.10: $\overleftrightarrow{L}_{in}$, $\overleftrightarrow{L}_{out}$, and point B found using $\overleftrightarrow{P}_{outer}$ and $\overleftrightarrow{P}_{inner}$.

A circle, the corner swell circle, is fit to the corner swell region to determine the diameter, D_{exp}, and the location of the swelling. As shown in Figure 3.11, three points U, V, and W are identified to determine this circle. Points U and V are defined using the line $\overleftrightarrow{R}$, which is the bisector of the angle between lines $\overleftrightarrow{L}_{in}$ and $\overleftrightarrow{L}_{out}$ at point B. As shown in Figure 3.11(a), point U is on $\overleftrightarrow{P}_{outer}$ that is tangent to the line $\overleftrightarrow{R}_U$, which is parallel to $\overleftrightarrow{R}$; point V is on $\overleftrightarrow{P}_{inner}$ that is tangent to the line $\overleftrightarrow{R}_V$, which is also parallel to $\overleftrightarrow{R}$. Point W is the point on $\overleftrightarrow{P}_{outer}$ that has the longest perpendicular distance from the line $\overline{BC'}$, as shown in Figure 3.11(b). The circle has two points U and W on its circumference and its diameter:

$$D_{exp} = \frac{|\overline{UV}| + |\overline{VW}|}{2} \tag{3.31}$$

where $|\overline{UV}|$ is the distance between points U and V and $|\overline{VW}|$ is the distance between points V and W. Point V is close to but not necessarily on this circle, as shown in Figure 3.11(c). The offset location of the center of the corner swell circle is determined relative to the point B with the x-axis being $\overleftrightarrow{L}_{out}$ and the y-axis being perpendicular to $\overleftrightarrow{L}_{out}$. The offset distances in the x- and y-axis are C_x and C_y, respectively.

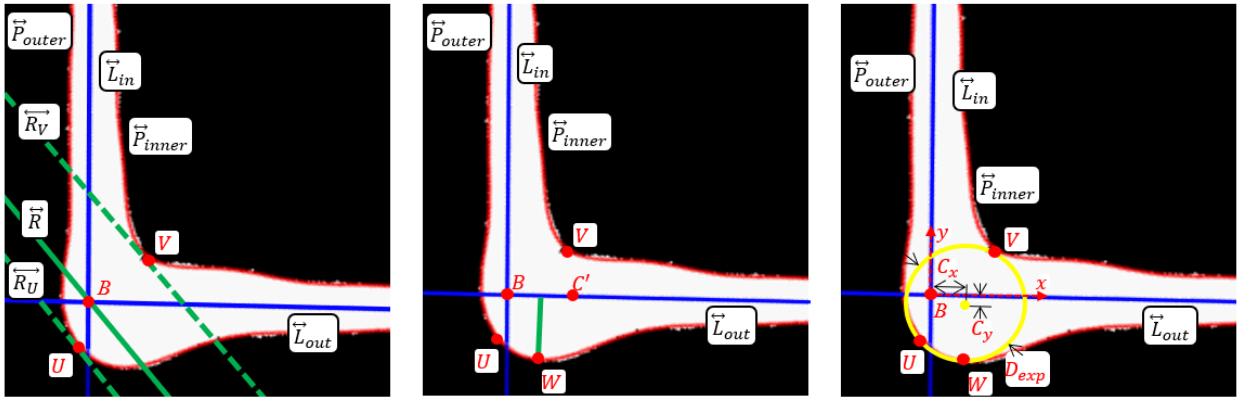

(a) (b) (c)

Figure 3.11: (a) Points U and V are the tangent points on $\overleftrightarrow{P}_{outer}$ and $\overleftrightarrow{P}_{inner}$ to lines parallel to $\overleftrightarrow{R}$, the angular bisector of $\overleftrightarrow{L}_{in}$ and $\overleftrightarrow{L}_{out}$ at point B. (b) Point W is the point on $\overleftrightarrow{P}_{outer}$ with the largest perpendicular distance to $\overline{BC'}$. (c) The diameter and location used to quantify the corner swell circle are defined by the points U, V, and W. The offset location of this circle relative to point B are C_x and C_y.

This strategy of quantifying the corner swell avoids having to occasionally use manual correction on a fit circle that is obviously undersized or misplaced for the swell region, which sometimes occurred when defining the circle using points U, V, and W directly. This approach is also applicable to non 90-degree turns as well to quantify the corner swell circle diameter and center location.

3.6. Results

Results of the CM calculations of the two-step response tests and the DIW 90-degree corner tool path are presented and compared against experimental measurements.

3.6.1 Two-step Response Results

Using the k, n, ρ, a, L, D, K_g, K_l, ΔX, and Δt parameters and volumetric inputs described in Section 4.4, the CM model of a two-step response for the PDP DIW system with the pipe and

ISSM is shown in Figure 3.12. The time for the system to reach 90% of the input flow after the step input is 0.088 and 0.728 s for the pipe and ISSM accordingly.

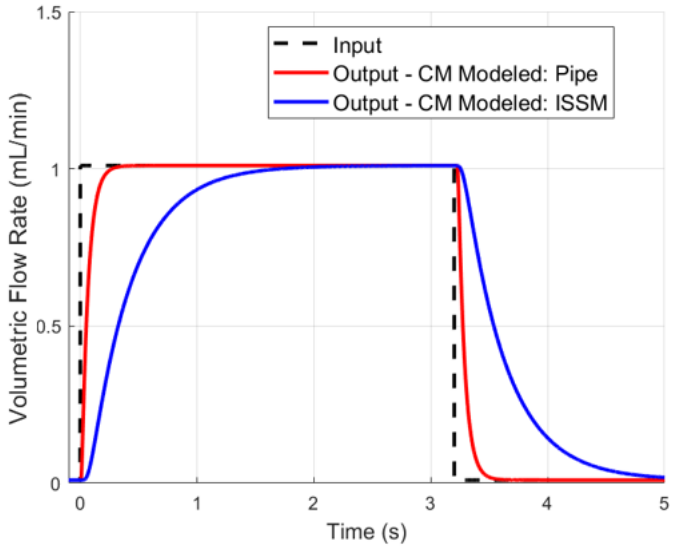

Figure 3.12: Two-step flow response of the PDP for the pipe and the ISSM.

Following the experimental procedure outlined in Section 4.5, the volumetric flowrate and pressure drop of the first (among the total six) two-step response experiments for the DIW system with a pipe are shown in Figure 3.13. The dashed black line in Figure 3.13(a) is the step volumetric flowrate input. The corresponding volumetric flowrate output measured by the Doppler flow meter is the dashed red lines. The robust loess filtered volumetric flowrate output filtering the noise from the sensor is shown as the solid red line. The CM model predicted volumetric flowrate, solid black line, is shown for comparison. The match between these two solid lines was good and validated the CM model. Figure 3.13(b) shows the measured pressure drop data (solid red line) next to the CM modeled pressure drop (solid black line). These two lines show a strong agreement in pressure drop between the experiments and the CM model.

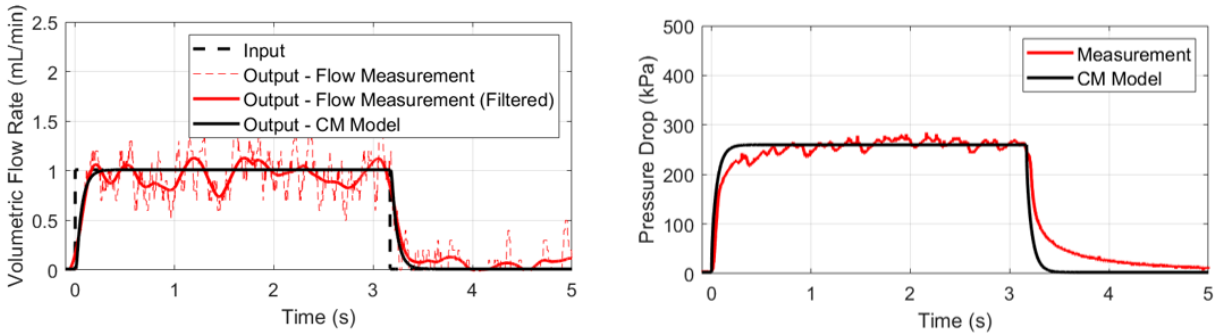

(b)

Figure 3.13: The experimental measured and CM modeled (a) volumetric flowrate and (b) pressure drop for the pipe two-step response test #1.

To further quantify the step response of the pipe, the rise of the filtered volumetric flowrate data of test #1 is fitted with a Gompertz function, Figure 3.14, where the a_g, b, and c values are 1.00 $\left(\frac{\text{mL}}{\text{min}}\right)$, 95.13 $\left(\frac{\text{mL}}{\text{min}}\right)$, and 31.75 $\left(\frac{\text{mL}}{\text{min}*\text{s}}\right)$, respectively, and an R^2 value of 0.83.

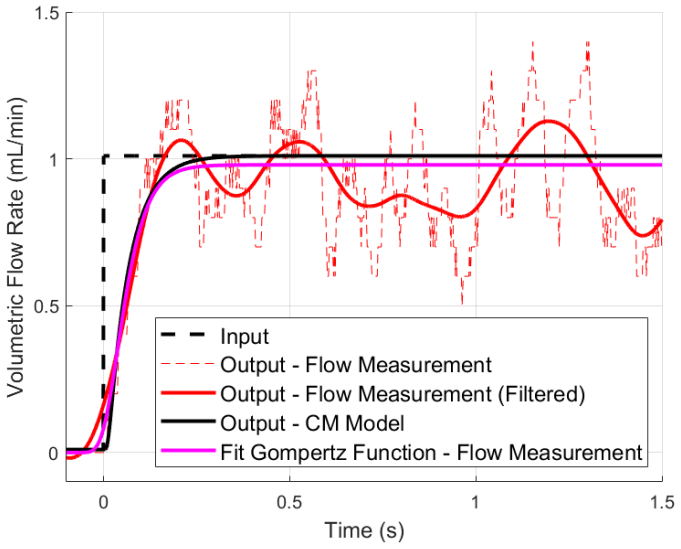

Figure 3.14: Fit Gompertz function of the volumetric flowrate for the pipe test #1.

In the same manner for the ISSM, the two-step response test #1 volumetric flowrate and pressure drop for the DIW system are shown in Figure 3.15. The dashed black line in Figure 3.15(a) shows the two-step volumetric flowrate input, and the dashed blue line is the responding volumetric flowrate output from doppler flow measurement. Additionally, the filtered volumetric flowrate, solid blue line, is shown to account for the noise from the sensor, and the CM modeled volumetric flowrate, solid black line, is shown for comparison. Figure 3.15(b) shows the measured pressure drop (solid blue line) next to the CM modeled pressure drop (solid black line). The volumetric flowrate and pressure drop data once again show a strong agreement between the experiments and the CM model.

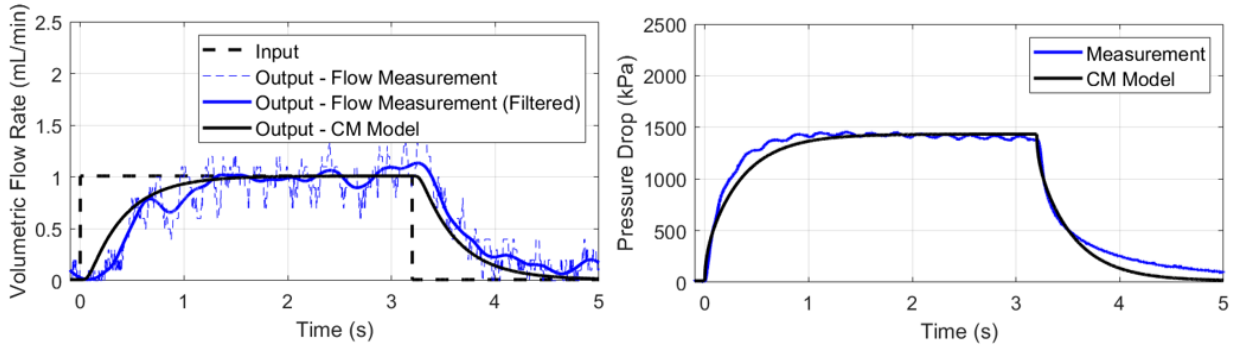

(a) (b)

Figure 3.15: The experimental measured and CM modeled (a) volumetric flowrate and (b) pressure drop for the ISSM two-step response test #1.

To further quantify the step response, the rise of the volumetric flowrate output is fit with a Gompertz function, Figure 3.16, where the a_g, b, and c values are 0.98 $\left(\frac{\text{mL}}{\text{min}}\right)$, 5.21 $\left(\frac{\text{mL}}{\text{min}}\right)$, and 3.99 $\left(\frac{\text{mL}}{\text{min}*\text{s}}\right)$, respectively, with an R^2 value of 0.94.

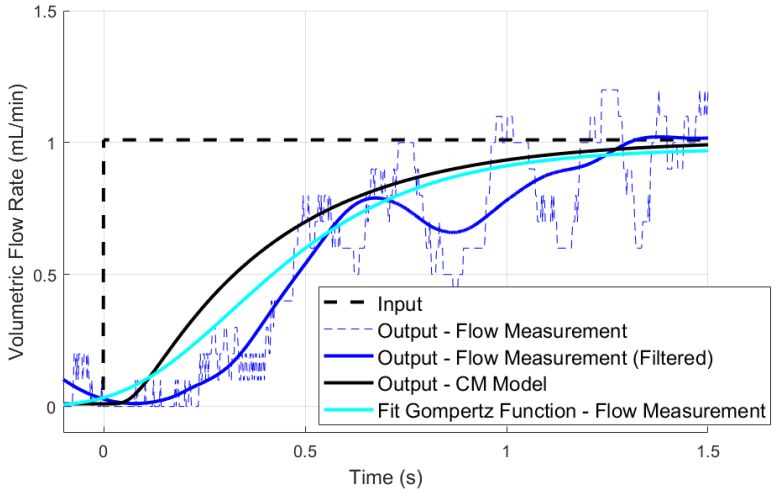

Figure 3.16: Fit Gompertz function of the volumetric flowrate for the ISSM test #1.

The fit Gompertz functions for the six experimental tests (marked as #1-#6) for the pipe are shown in Figure 3.17 as the dotted lines with an average R^2 of 0.83 and a minimum R^2 of 0.81, as listed in Table 1. For the ISSM, the fit Gompertz functions of six experimental tests (also marked as #1-#6) had an average R^2 of 0.94 and a minimum R^2 of 0.90, as listed in Table 1. The a_g, b, and c values, as well as the 95% confidence bounds of the Gompertz function for all 12 tests and CM model data for pipe and ISSM, are shown below in Table 3.1. The CM models response, the solid lines in Figure 3.12, are fit with the Gompertz function to allow for easy recreation of the modeling results, and comparison with the experimental data. The agreement between the CM model and the experimental measurements in pipe tests is better than that in ISSM tests, likely due to the longer response time of the ISSM being affected more by the noise of the volumetric flowrate sensor. Overall, the CM does characterize the response of the system to step inputs well in both configurations.

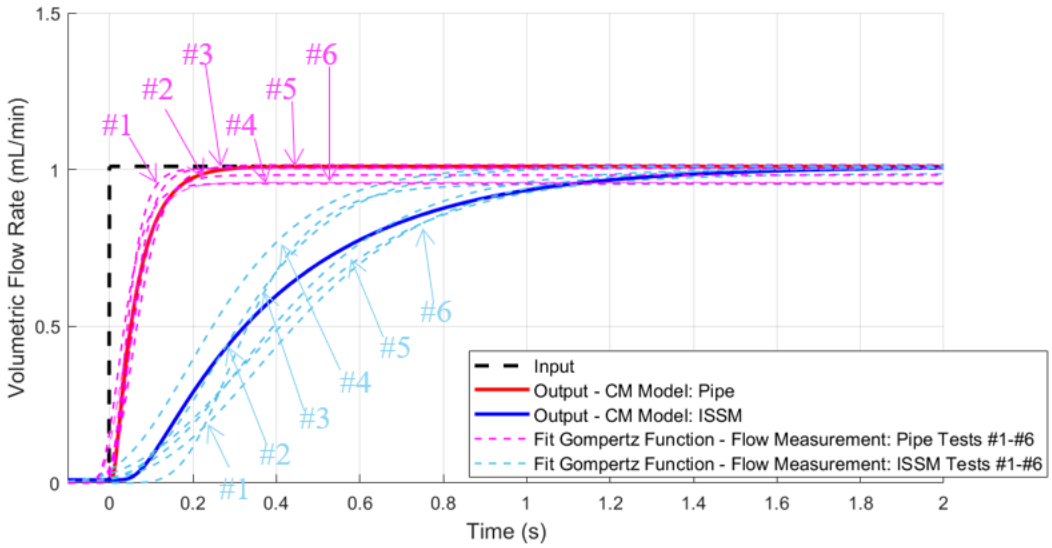

Figure 3.17: Fit Gompertz functions for the six two-step response experiments for both the pipe and ISSM shown with the modeled responses using CM.

Table 3.1: a_g, b, and c values, 95% confidence bounds, and R2 values of the Gompertz function fit to the first step in the two-part step test

			a_g 95% Confidence			b_g 95% Confidence			c_g 95% Confidence		
Config	Test	a_g $\left(\frac{mL}{min}\right)$	*Lower*	*Upper*	b_g $\left(\frac{mL}{min}\right)$	*Lower*	*Upper*	c_g $\left(\frac{mL}{min*s}\right)$	*Lower*	*Upper*	R^2
ISSM	CM Model	0.99	0.98	0.98	4.90	4.82	4.97	4.43	4.39	4.47	0.99
ISSM	#1	0.98	0.97	1.00	5.21	4.55	5.87	3.99	3.72	4.27	0.90
ISSM	#2	0.95	0.94	0.96	32.2	23.54	40.94	9.07	8.42	9.73	0.94
ISSM	#3	1.01	1.00	1.01	8.23	7.33	9.13	6.02	5.74	6.29	0.96
ISSM	#4	1.01	1.00	1.02	5.94	5.24	6.64	6.13	5.79	6.48	0.93
ISSM	#5	1.00	0.99	1.01	6.54	5.93	7.15	4.54	4.34	4.74	0.96
ISSM	#6	1.00	0.99	1.01	6.77	5.98	7.55	4.17	3.94	4.41	0.93
Pipe	CM Model	1.01	1.01	1.01	39.86	38.00	41.71	26.01	25.71	26.32	0.99
Pipe	#1	1.00	0.97	1.04	95.13	1.13	189.10	31.75	25.10	38.39	0.83
Pipe	#2	0.98	0.96	0.99	38.91	20.12	57.70	25.73	22.57	28.90	0.88
Pipe	#3	1.01	0.99	1.03	34.49	13.18	55.80	23.45	19.62	27.27	0.82
Pipe	#4	0.95	0.94	0.97	24.24	11.43	37.05	24.49	20.82	28.15	0.82
Pipe	#5	1.00	0.98	1.02	130.70	-5.88	267.20	36.53	29.12	43.94	0.85
Pipe	#6	0.95	0.94	0.97	30.02	12.72	47.33	28.24	23.95	32.54	0.81

3.6.2 DIW 90-degree Corner Tool path Results

The CM modeling procedure using k, n, ρ, a, L, D, K_g, K_l, ΔX, and Δt parameters and volumetric inputs for the 90-degree tool paths described in Section 3.5.6 is performed on a combined ISSM and tapered nozzle. The DIW extrusion print profiles for the 90-degree corner and the diameter and locations of the corner swell are compared with experimental data gathered following the experimental procedure outlined in Section 3.5.7.

Trapezoidal motion planning was used to generate the tool paths for the 90-degree corner and produced a tool path for the DIW system, as seen in Figure 3.7. The distance and travel time between the points A, A', B, C', and, C is dependent on the predefined velocity (25 mm/s), jerk (2 mm/s), and acceleration (100, 250, 500, 1000, 1500, and 2000 mm/s^2). For the 90-degree corner print, the distance and travel time for line segments $\overline{AB}$, $\overline{A'B}$, $\overline{BC'}$, and $\overline{BC}$ in Figure 3.8 created by trapezoidal motion planning, is reported in Table 3.2.

Table 3.2: Distance and travel time between points of interest in the 90-degree corner tool path.

Acceleration (mm/s^2)	$\overline{AB}$ Distance (mm)	$\overline{AB}$ Travel Time (sec)	BA' Distance (mm)	$\overline{A'B}$ Travel Time (sec)	$\overline{BC'}$ Distance (mm)	$\overline{BC'}$ Travel Time (sec)	$\overline{BC}$ Distance (mm)	$\overline{BC}$ Travel Time (sec)
100	12.47	0.485	0.25	0.057	0.25	0.057	12.47	0.485
250	3.14	0.122	0.25	0.039	0.25	0.039	3.14	0.122
500	2.49	0.097	0.25	0.029	0.25	0.029	2.49	0.097
1000	1.23	0.048	0.25	0.021	0.25	0.021	1.23	0.048
1500	0.82	0.032	0.25	0.017	0.25	0.017	0.82	0.032
2000	0.62	0.024	0.25	0.015	0.25	0.015	0.62	0.024

The extrusion kinematics produced by trapezoidal motion planning is the volumetric flowrate vs. time from the PDP in the DIW and input into ISSM and tapered nozzle. For each acceleration (100, 250, 500, 1000, 1500, and 2000 mm/s^2), the extrusion kinematics is used as the input for the CM model and is shown as the black lines in Figure 3.18. The CM model finds the resulting volumetric flowrate output by the nozzle on the DIW system, shown by the red lines in Figure 3.18. There is a significant discrepancy between the input (out of the progressive cavity pump and into ISSM) and output (out of the nozzle tip) volumetric flowrate. Due to the deceleration of the nozzle approaching point B, the volumetric flowrate should be reduced proportionally. However, the output (red) lags behind the input. This causes excess flow in the swell region, creating the corner swell. At higher accelerations, 1000, 1500, and 2000 mm/s^2, the output flowrate response was so slow that, as shown in Figure 3.18(d), (e), and (f), there was no noticeable change in the output volumetric flowrate until the nozzle left the corner region. When using trapezoidal motion planning, it was assumed that the output volumetric flowrate closely mirrors the shape of the input flowrate. However, as shown in Figure 3.18, using only trapezoidal motion planning to control the DIW will lead to corner swelling and defects in parts.

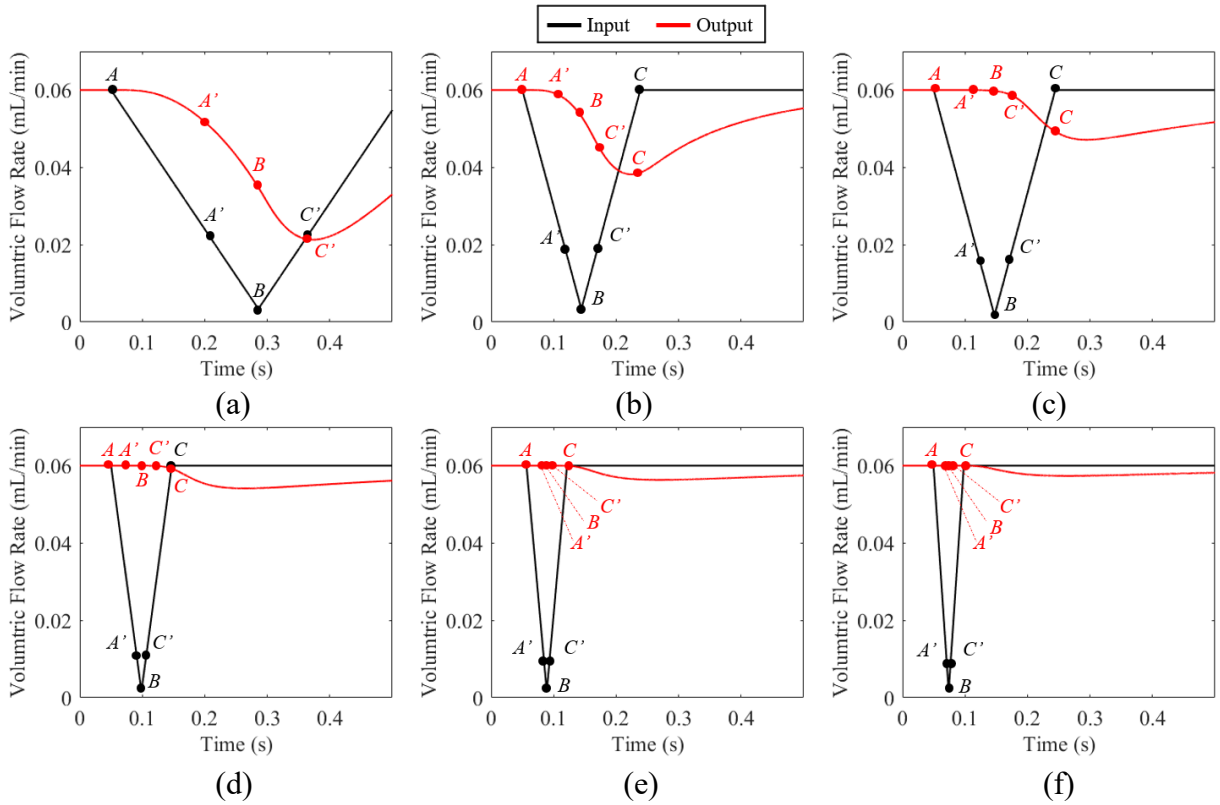

Figure 3.18: The volumetric flowrate inputs and CM modeled outputs for a 90-degree corner extrusion kinematics using the combined ISSM and tapered nozzle with (a) 100, (b) 250, (c) 500, (d) 1000, (e) 1500, and (f) 2000 mm/s^2 acceleration from trapezoidal motion planning.

From the CM modeled volumetric outputs, the width of print profile w between $\overline{AA'}$, and $\overline{C'C}$ is estimated using Equation (29). The diameter of the corner swell circle D_{swell} created by the excess flow at B is estimated using Equation (3.30) for each of accelerations. Figure 3.19 shows the print profile based on w and the swell circle centered at B based on D_{swell}. As each tool path gets near the corner swell region, there is a rapid change in the modeled print profile caused by the manner w is calculated using Equation (3.29). As the nozzle speed approaches its minimum velocity at Point *B*, w becomes asymptotic and changes rapidly. This behavior is not expected in experimental results.

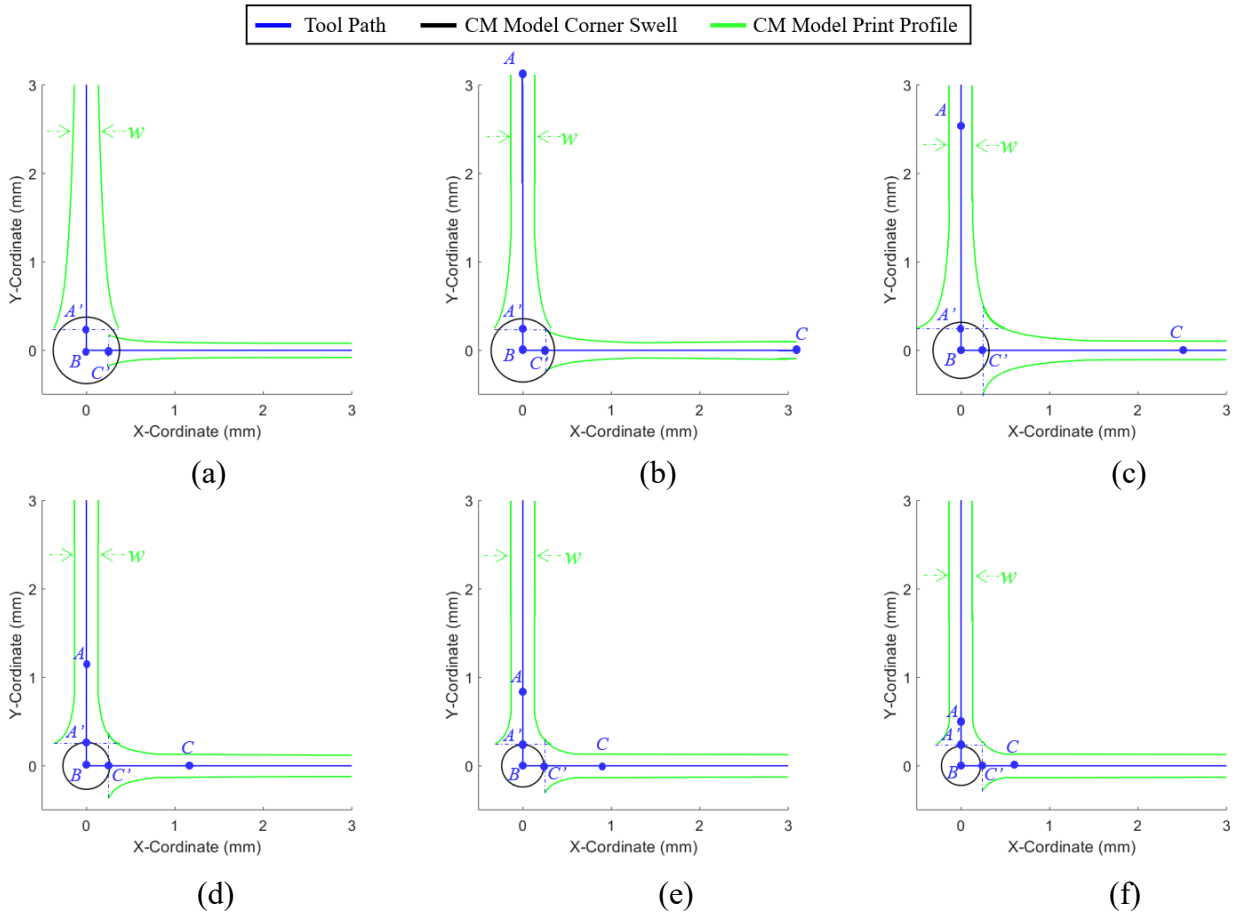

Figure 3.19: The modeled corner swell and print profile using CM for a 90 degree corner tool path with (a) 100, (b) 250, (c) 500, (d) 1000, (e) 1500, and (f) 2000 mm/s^2 acceleration.

Figure 3.20 shows the experimental print profile of the extrusion for each acceleration (100, 250, 500, 1000, 1500, and 2000 mm/s^2) with the DIW system. The image processing of the print profile described in Section 3.5.7 is applied to identify the tool path. Significant corner swelling can be identified due to the extrusion kinematics of the 90-degree corner in Figure 3.18. The procedure outlined in Section 3.5.7 are utilized to find points U, V, and W as well as D_{exp}, C_x, and C_y of the corner swell circle, which are shown in the close-up view of the corner in Figure 3.20.

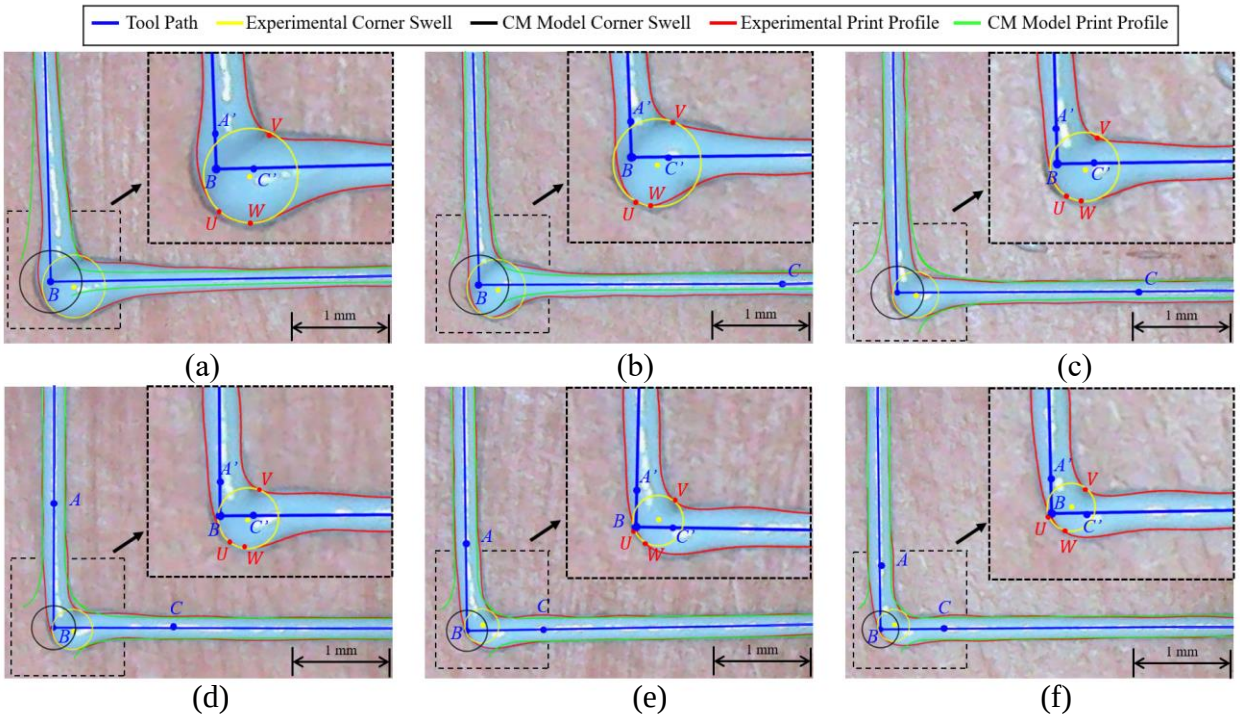

Figure 3.20: The comparison of the measured and CM model tool path, corner swell, and print profile for a 90 degree corner tool path with (a) 100, (b) 250, (c) 500, (d) 1000, (e) 1500, and (f) 2000 mm/s^2 acceleration.

Figure 3.21 compares the average and standard deviation of the experimental D_{exp} with CM model predicted D_{swell}. D_{exp} and D_{swell} showed a strong agreement, with swell diameter decreasing as acceleration increased. This is due to the reduction in total time spent in the corner region and not the volumetric output conforming to the volumetric input as desired by the trapezoidal motion planning.

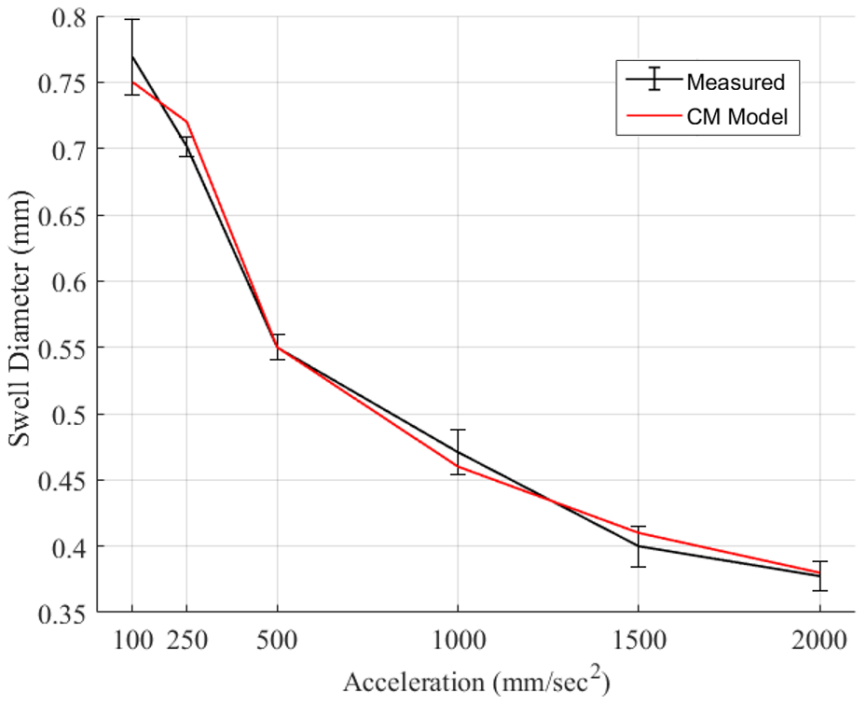

Figure 3.21: The measured and CM model swell circle diameter and its standard deviation of the measurements under six accelerations.

Figure 3.22 presents the average and standard deviation of experimentally measured C_x and C_y under six accelerations. This offset in the corner swell location can be seen in the close-up view in the print profile in Figure 3.20. The cause for this shift is due to the release of tension in belts of the DIW system as the nozzle nears its minimum velocity, resulting in a slight shift in the nozzle location. This is why the shift is consistent across all acceleration values even though the forces on the frame increase with the acceleration. The offset in center location is most visible during the lower accelerations because the total time and distance traveled by the nozzle with the released belt tension are largest for the lower acceleration print kinematics.

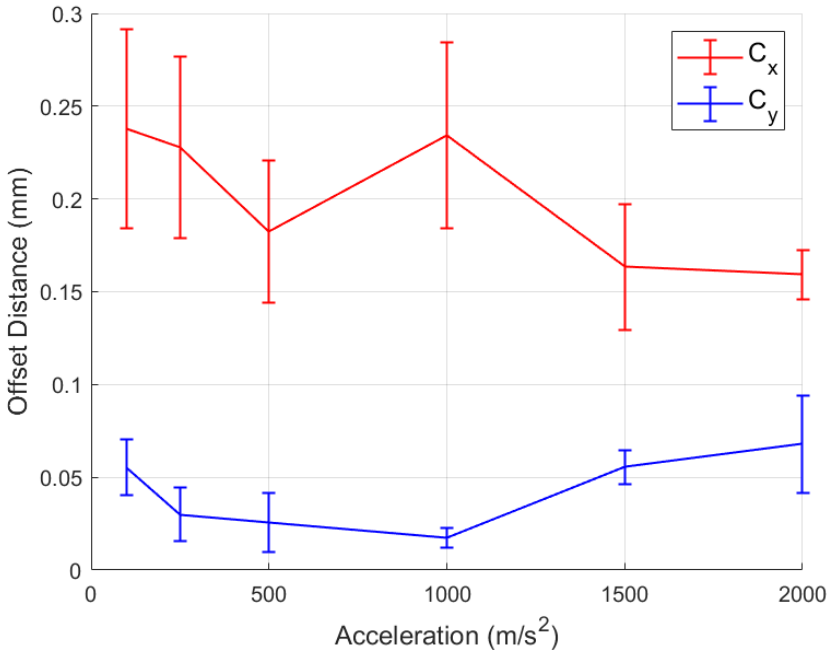

Figure 3.22: The C_x and C_y and their standard deviation of corner swell center under six accelerations.

3.7. Conclusions and Future Work

The continuity and momentum equations solved through the CM model were able to characterize the behavior of a PDP DIW system. The new mathematical friction models for the DIW system using pipes, static mixers, and fine dispensing nozzles, as well as the appropriate boundary conditions, allowed the CM model to predict with reasonable accuracy the dynamic behavior of a dispensed high viscosity fluid.

The tested input response and tool path simulations demonstrated that DIW systems could have a high degree of variation between the input and output flowrates during transient conditions. In the two-step response testing, the CM model predicted that the pipe and ISSM would have a response time of 0.088 and 0.628 s, respectively. Experimentally the CM model predicted volumetric flowrate, and pressure drop matched the experimental measurements as determined by comparing Gompertz functions fit to experimental measurements. CM was also used to simulate the behavior of a DIW system printing a 90-degree corner. The CM analysis

predicted the size of the corner swell across a range of acceleration values and captured the general shape of the line produced. There was a deviation in the corner swell center locations in the experimental results that were not predicted by CM. The cause of which, the release of belt tension in the DIW system, were analyzed.

This study showed that the DIW system's flow response behavior needs to be controlled for high-quality DIW tool paths. Assuming a simple linear approximation for the acceleration of the fluid in the transient flow of a DIW system is not adequate. Using only trapezoidal motion planning to generate a tool path for a 90-degree corner for the PDP DIW system resulted in a high variation between the desired and actual deposition. The inspection of the same tool path using CM predicted the same results. Based on this study, a better understanding of transient fluid behavior and more sophisticated control schemes can be created. Future work on DIW systems will use the CM for flowrate control to achieve precision DIW AM.

Chapter 4. Feedforward Error Compensation Control of Direct Ink Writing Additive Manufacturing using the Characteristic Method

4.1. Abstract

The transient flow of fluid for a direct ink write (DIW) system is controlled using feedforward error correction control (FECC). FECC combines trapezoidal motion planning, a transient fluid flow model, machine learning, and iLQR to create new extrusion flow paths for DIW. The new extrusion flow paths are inserted into existing tool paths for DIW to improve deposition accuracy and a corrected flow path can be reused repeatedly creating a library of corrected tool paths. The FECC process is applied to two types of tool paths: a 90-degree corner and a U-turn. With FECC the 2-norm error of the 90-degree turn transient fluid flow is reduced from 0.32 to 0.16 mL/min, while the measured size of the 90-degree corner bulge diameter was reduced from 0.63±0.03 mm to 0.48±0.03 mm. For the U-turn, the 2-norm error for transient fluid flow is reduced from 0.43 to 0.18 mL/min and the measured width of the U-turn was reduced from 0.98±0.04 mm to 0.82±0.03 mm. The total error reduction by FECC for the 90-degree corner and U-turn was 25-40%. The FECC tool paths were applied to a test part that has 5000 90-degree turns and 8500 U-turns. Without FECC the test part had noticeable bulging at the corners, material build up at the edges of infill, and gaps in the infill. The test part with FECC had noticeably improved quality with the corner bulging, material build up, and gaps all reduced significantly. This study demonstrates how FECC can be used to correct for errors in DIW deposition and be applied to improve part quality.

4.2. Introduction

Feedforward control with an accurate process model has been shown to be very effective in improving the quality of powder bed fusion (PBF) [67–69]. Using the CM model from Chapter 3 as the DIW process model this chapter investigates how feedforward control can be implemented in a DIW system.

In this chapter feedforward error compensation control (FECC) using the CM model, trapezoidal motion planning, machine learning, and an iterative linear quadratic regulator (iLQR) is shown in Section 4.3. The experimental setup to validate FECC is covered in Section 4.4. Section 4.5 discusses the results of the experimental FECC validation and the conclusions are discussed in Section 4.6.

4.3. Feedforward Error Compensation Control and Path Modification for Trapezoidal Motion Planner

Feedforward control and error compensation are techniques that require accurate process models to implement. For this study, the process model is the CM model described in Section 3.4. The CM model predicts the transient volumetric flow of the DIW process to enable accurate corrections of flowrate along the printing tool path using the feedforward controller and trapezoidal motion planning. In this section, the trapezoidal motion planning, the FECC using the CM and trapezoidal motion planning, and the application of FECC in 90-degree turn and U-turn tool paths are discussed.

4.3.1 Trapezoidal Motion Planning

Trapezoidal planners have proven to be an efficient method to produce kinematic motion paths in AM [13]. The path of travel of the DIW extrusion nozzle, $\boldsymbol{\Upsilon}$, is defined by a sequenced set of points $\{\boldsymbol{p_1}, \boldsymbol{p_2}, \dots, \boldsymbol{p_j}, \dots, \boldsymbol{p_n}\}$. Every $\boldsymbol{p_j}$ is defined as a 4x1 matrix in the X, Y, Z, and E coordinates. The X, Y, and Z are positions in the Cartesian space, Figure 4.1(a), while E is the dimension representing the amount of material for extrusion Figure 4.1(b). E is given in units of length, corresponding to the length for an amount of fluid in a container with a uniform cross-sectional area. This approach has been utilized in molten plastic MEX, known as fused filament fabrication (FFF), where E is a length of plastic filament and the convention is convenient for motion planning purposes [92]. The same approach has been adopted in this study with E in the unit of length for motion planning and then converted into the unit for volumetric fluid flow in the CM model.

In the $\boldsymbol{\Upsilon}$**,** adjacent points, $\{\boldsymbol{p_j}, \boldsymbol{p_{j+1}}\}$ are defined as $\boldsymbol{S}(t)$, where $\boldsymbol{S}(t)$ is a 4x2 matrix. For motion planning, $\boldsymbol{S}(t)$ is split into $\boldsymbol{S_c}(t)$, a 3x2 matrix representing the Cartesian X, Y, and Z coordinates of $\{\boldsymbol{p_j}, \boldsymbol{p_{j+1}}\}$, and $\boldsymbol{S_e}(t)$, a 1x2 vector representing the E coordinate. The nozzle velocity in the Cartesian and the rate of change in length of material in the extrusion coordinates, are represented as $\dot{\boldsymbol{S}}_{\boldsymbol{c}}(t)$ and $\dot{\boldsymbol{S}}_{\boldsymbol{e}}(t)$, respectively. These two velocity vectors are planned using two separate trapezoidal motion planners to calculate the motion of $\boldsymbol{S}(t)$ with respect to time, t. Ideally, $\dot{\boldsymbol{S}}_{\boldsymbol{e}}(t)$ is proportional to $\dot{\boldsymbol{S}}_{\boldsymbol{c}}(t)$ for each $\boldsymbol{S} \in \boldsymbol{\Upsilon}$, as shown in Figure 4.1(c). However, synchronicity is not required between $\dot{\boldsymbol{S}}_{\boldsymbol{e}}(t)$ and $\dot{\boldsymbol{S}}_{\boldsymbol{c}}(t)$. In this study, the dual trapezoidal motion planner approach is adopted to decouple the planning of $\dot{\boldsymbol{S}}_{\boldsymbol{e}}(t)$ and $\dot{\boldsymbol{S}}_{\boldsymbol{c}}(t)$. The rate of deposition of material in DIW is asynchronous from the extrusion nozzle's Cartesian movement. This approach allows for the implementation of corrective control on the $\dot{\boldsymbol{S}}_{\boldsymbol{c}}(t)$ and $\dot{\boldsymbol{S}}_{\boldsymbol{e}}(t)$ to reduce

errors created by the nonlinear DIW extrusion fluid flow in the nozzle while following the Cartesian path in $\boldsymbol{\Upsilon}$.

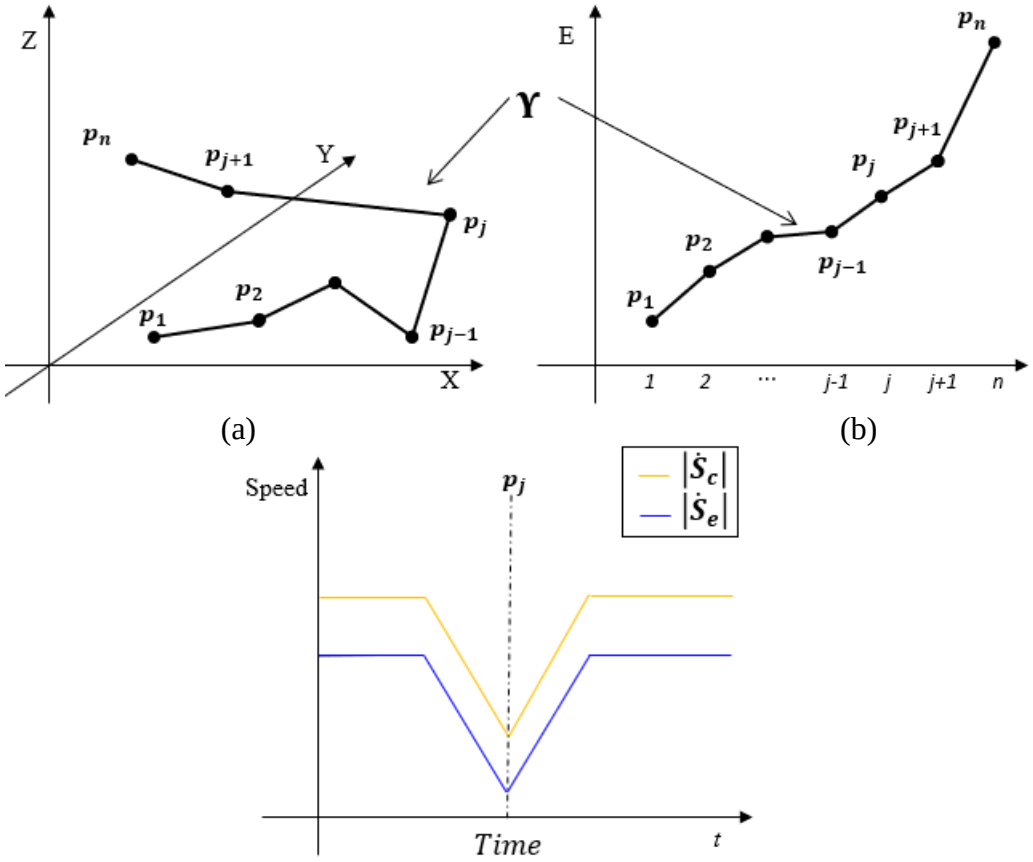

Figure 4.1: The points that make up the tool path in the(a) Cartesian (X, Y, and Z) coordinates, (b) the extrusion coordinate (E) for each point $\boldsymbol{p_j}$ on $\boldsymbol{\Upsilon}$, and (c) the synchronous $\dot{\boldsymbol{S}}_{\boldsymbol{c}}(t)$ and $\dot{\boldsymbol{S}}_{\boldsymbol{e}}(t)$ using trapezoidal motion planning for a 90-degree turn of the DIW extrusion nozzle at $\boldsymbol{p_j}$.

4.3.1.1 Trapezoidal Motion Planning – Cartesian

The Cartesian trapezoidal motion planner with a target velocity, $\boldsymbol{v_c}$, and acceleration, $\boldsymbol{a_c}$, determines the nozzle travel between a series of pair of Cartesian points that make up the $\boldsymbol{S_c}(t)$. When the extrusion nozzle is traveling along $\boldsymbol{S_c}(t)$, the motion profile has three phases: acceleration, constant velocity, and deceleration as defined by the following [93]:

Acceleration $$\dot{\boldsymbol{S}}_{\boldsymbol{c}}(t) = \boldsymbol{a}_{\boldsymbol{c}} t + \dot{\boldsymbol{S}}_{\boldsymbol{c}}(0), \quad \text{for } 0 \leq t \leq \frac{\left|\boldsymbol{v}_{\boldsymbol{c}} - \dot{\boldsymbol{S}}_{\boldsymbol{c}}(0)\right|}{|\boldsymbol{a}_{\boldsymbol{c}}|} \tag{4.1}$$

Constant Velocity $$\dot{\boldsymbol{S}}_{\boldsymbol{c}}(t) = \boldsymbol{v}_{\boldsymbol{c}}, \quad \text{for } \frac{\left|\boldsymbol{v}_{\boldsymbol{c}} - \dot{\boldsymbol{S}}_{\boldsymbol{c}}(0)\right|}{|\boldsymbol{a}_{\boldsymbol{c}}|} < t \leq T - \frac{\left|\boldsymbol{v}_{\boldsymbol{c}} - \dot{\boldsymbol{S}}_{\boldsymbol{c}}(T)\right|}{|\boldsymbol{a}_{\boldsymbol{c}}|} \tag{4.2}$$

Deceleration $$\dot{\boldsymbol{S}}_{\boldsymbol{c}}(t) = \boldsymbol{v}_{\boldsymbol{c}} - \boldsymbol{a}_{\boldsymbol{c}}\left(t + \frac{\left|\boldsymbol{v}_{\boldsymbol{c}} - \dot{\boldsymbol{S}}_{\boldsymbol{c}}(T)\right|}{|\boldsymbol{a}_{\boldsymbol{c}}|} - T\right), \quad \text{for } T - \frac{\left|\boldsymbol{v}_{\boldsymbol{c}} - \dot{\boldsymbol{S}}_{\boldsymbol{c}}(T)\right|}{|\boldsymbol{a}_{\boldsymbol{c}}|} < t \leq T \tag{4.3}$$

where T is the time it takes to travel along the length of $\boldsymbol{S}_{\boldsymbol{c}}(t)$, represented as $|\boldsymbol{S}_{\boldsymbol{c}}|$, and $0 \leq t \leq T, \forall\, \boldsymbol{S} \in \boldsymbol{\Upsilon}$. It should be noted that for every $\boldsymbol{S}(t)$, t will range from 0 to T, and the $\sum T \;\forall\, \boldsymbol{S}(t) \in \boldsymbol{\Upsilon}$ is the total time that it takes the DIW system to complete the $\boldsymbol{\Upsilon}$. Additionally, $\dot{\boldsymbol{S}}_{\boldsymbol{c}}(t)$ can be decomposed into its respective components in the X, Y, and Z dimensions for motion in the Cartesian coordinate.

For DIW systems, it is important to minimize the time spent during the acceleration and deceleration phases. This is represented by minimizing the Cartesian trapezoidal objective value, Λ [90]:

$$\Lambda = \sum \frac{\left|2\boldsymbol{v}_{\boldsymbol{c}} - \dot{\boldsymbol{S}}_{\boldsymbol{c}}(0) - \dot{\boldsymbol{S}}_{\boldsymbol{c}}(T)\right|}{|\boldsymbol{a}_{\boldsymbol{c}}|}, \quad \forall\, \boldsymbol{S} \in \boldsymbol{\Upsilon} \tag{4.4}$$

Two constraints are used in conjunction with Λ to find the $\dot{\boldsymbol{S}}_{\boldsymbol{c}}(\boldsymbol{t})$. The first constraint creates a continuous velocity path along $\boldsymbol{\Upsilon}$ for the extrusion nozzle of the DIW system with the starting and exit velocity magnitudes for each adjacent $\boldsymbol{S}_{\boldsymbol{c}}(t)$ in $\boldsymbol{\Upsilon}$ are the same.

$$\left|\dot{\boldsymbol{S}}_{\boldsymbol{c}}(T)_i\right| - \left|\dot{\boldsymbol{S}}_{\boldsymbol{c}}(0)_{i+1}\right| = 0, \quad \forall\, \boldsymbol{S} \in \boldsymbol{\Upsilon} \tag{4.5}$$

The second constraint limits the magnitude of the difference between the Cartesian velocity vectors of $\dot{\boldsymbol{S}}_{\boldsymbol{c}}(T)_i$ and $\dot{\boldsymbol{S}}_{\boldsymbol{c}}(0)_{i+1}$ to be less than J, commonly referred to as a jerk in the

trapezoidal motion planner [90]. The constraint allows for a limited amount of instantaneous change in velocity vector direction by the trapezoidal planner. This jerk, as implemented in trapezoidal motion planners, approximates the third derivative of position with the same name. The constraint using *J* is:

$$\left|\dot{\boldsymbol{S}}_{\boldsymbol{c}}(T)_i - \dot{\boldsymbol{S}}_{\boldsymbol{c}}(0)_{i+1}\right| \leq J, \qquad \forall\, \boldsymbol{S} \in \boldsymbol{\Upsilon} \tag{4.6}$$

There may exist some $\boldsymbol{S}(t) \in \boldsymbol{\Upsilon}$ where the time spent in the constant velocity phase of the Cartesian trapezoidal motion path will be zero based on the constraints shown in Eqs. (4.1)-(4.6). If $|\boldsymbol{S}_{\boldsymbol{c}}|$ is less than the distance traveled during the acceleration and deceleration phases, the constant velocity phase will be skipped as the extrusion nozzle will not be able to reach constant velocity during that specific $\boldsymbol{S}(t)$.

The time spent in the acceleration and deceleration phase is zero if $\left|\dot{\boldsymbol{S}}_{\boldsymbol{c}}(T)\right|$ or $\left|\dot{\boldsymbol{S}}_{\boldsymbol{c}}(0)\right| = |\boldsymbol{v}_{\boldsymbol{c}}|$ for any $\boldsymbol{S}(t)$. The corresponding acceleration or deceleration phase will be skipped for that specific $\boldsymbol{S}$ since there is no need to change velocity [91]. The condition of $\left|\dot{\boldsymbol{S}}_{\boldsymbol{c}}(0)\right|$or $\left|\dot{\boldsymbol{S}}_{\boldsymbol{e}}(T)\right| > |\boldsymbol{v}_{\boldsymbol{c}}|$ is not possible because the trapezoidal motion planner will stop accelerating once $\left|\dot{\boldsymbol{S}}_{\boldsymbol{c}}\right|$ is equal to $|\boldsymbol{v}_{\boldsymbol{c}}|$.

4.3.1.2 Trapezoidal Motion Planning – Extrusion

For the DIW system used in this study, the motion in the extrusion dimension, $\dot{\boldsymbol{S}}_{\boldsymbol{e}}(t)$, between two points in the extrusion dimension of $\boldsymbol{S}_{\boldsymbol{e}}$ is planned in conjunction with the system's Cartesian movement, $\dot{\boldsymbol{S}}_{\boldsymbol{e}}(t) \in \boldsymbol{S}_{\boldsymbol{e}}(t)$. The extrusion trapezoidal planner uses constraints in extrusion coordinate acceleration, $\boldsymbol{a}_{\boldsymbol{e}}$, and extrusion jerk, J_e, as well as $|\boldsymbol{S}_{\boldsymbol{c}}|$ and $|\boldsymbol{S}_{\boldsymbol{e}}|$ to solve the steady-state extrusion velocity vector, $\boldsymbol{v}_{\boldsymbol{e}}$:

$$\boldsymbol{v}_{\boldsymbol{e}} = \boldsymbol{v}_{\boldsymbol{c}} \left|\boldsymbol{S}_{\boldsymbol{c}}\right| \Big/ \left|\boldsymbol{S}_{\boldsymbol{e}}\right|, \qquad \forall\, \boldsymbol{S} \in \boldsymbol{\Upsilon} \tag{4.7}$$

where $|\boldsymbol{S_e}|$ is the length of $\boldsymbol{S}$ in the extrusion coordinate.

The extrusion trapezoidal planner uses the same acceleration phase, constant velocity phase, deceleration phase structure the Cartesian trapezoidal planner uses. The main difference between the two planners is that *T* is determined by the Cartesian trapezoidal motion planner and not by the extrusion trapezoidal planner. By sharing the same *T*, the two trapezoidal motion planners are linked together.

Acceleration
$$\dot{\boldsymbol{S}}_{\boldsymbol{e}}(t) = \boldsymbol{a_e}t + \dot{\boldsymbol{S}}_{\boldsymbol{e}}(0), \quad \text{for } 0 \le t \le \frac{\left|\boldsymbol{v_e} - \dot{\boldsymbol{S}}_{\boldsymbol{e}}(0)\right|}{|\boldsymbol{a_e}|} \tag{4.8}$$

Constant Velocity
$$\dot{\boldsymbol{S}}_{\boldsymbol{e}}(t) = \boldsymbol{v_e}, \quad \text{for } \frac{\left|\boldsymbol{v_e} - \dot{\boldsymbol{S}}_{\boldsymbol{e}}(0)\right|}{|\boldsymbol{a_e}|} < t \le T - \frac{\left|\boldsymbol{v_e} - \dot{\boldsymbol{S}}_{\boldsymbol{e}}(T)\right|}{|\boldsymbol{a_e}|} \tag{4.9}$$

Deceleration
$$\dot{\boldsymbol{S}}_{\boldsymbol{e}}(t) = \boldsymbol{v_e} - \boldsymbol{a_e}\left(t + \frac{\left|\boldsymbol{v_e} - \dot{\boldsymbol{S}}_{\boldsymbol{e}}(T)\right|}{|\boldsymbol{a_e}|} - T\right), \quad \text{for } T - \frac{\left|\boldsymbol{v_e} - \dot{\boldsymbol{S}}_{\boldsymbol{e}}(T)\right|}{|\boldsymbol{a_e}|} < t \le T \tag{4.10}$$

The extrusion trapezoidal planner's objective function and constraints are similar to the ones in the Cartesian trapezoidal motion planner. Overall the objective function seeks to maximize the time spent in the constant velocity phase, and the constraints create a continuous motion path along $\boldsymbol{\Upsilon}$ and to limit the difference between extrusion velocity vectors:

$$\Lambda_e = \sum \frac{\left|2\boldsymbol{v_e} - \dot{\boldsymbol{S}}_{\boldsymbol{e}}(0) - \dot{\boldsymbol{S}}_{\boldsymbol{e}}(T)\right|}{|\boldsymbol{a_e}|}, \quad \forall \boldsymbol{S} \in \boldsymbol{\Upsilon} \tag{4.11}$$

$$\left|\dot{\boldsymbol{S}}_{\boldsymbol{e}}(T)_i\right| - \left|\dot{\boldsymbol{S}}_{\boldsymbol{e}}(0)_{i+1}\right| = 0, \quad \forall \boldsymbol{S} \in \boldsymbol{\Upsilon} \tag{4.12}$$

$$\left|\dot{\boldsymbol{S}}_{\boldsymbol{e}}(T)_i - \dot{\boldsymbol{S}}_{\boldsymbol{e}}(0)_{i+1}\right| \le J_e, \quad \forall \boldsymbol{S} \in \boldsymbol{\Upsilon} \tag{4.13}$$

where Λ_e is the extrusion objective value that is minimized to keep the motion of $\dot{\boldsymbol{S}}_{\boldsymbol{e}}$ in the constant velocity phase as much as possible and J_e is the jerk in the extrusion coordinate.

The extrusion trapezoidal planner may exhibit the same behavior as the Cartesian trapezoidal motion planner when the time in the constant velocity phase is zero, based on the constraints in Eqs. (4.8)-(4.13). If $|\boldsymbol{S_e}|$ is less than the distance traveled during the acceleration and deceleration phase, the constant velocity phase will be skipped as the extrusion will not be able to reach constant velocity during $\boldsymbol{S}$.

The time spent in the acceleration and deceleration phase is zero if $|\dot{\boldsymbol{S}}_{\boldsymbol{e}}(0)|$or $|\dot{\boldsymbol{S}}_{\boldsymbol{e}}(T)| = |\boldsymbol{v_e}|$ for any $\boldsymbol{S}$. Then the corresponding acceleration or deceleration phase will be skipped for that specific $\boldsymbol{S}$ since there is no need to change velocity. The condition of $|\dot{\boldsymbol{S}}_{\boldsymbol{e}}(0)|$or $|\dot{\boldsymbol{S}}_{\boldsymbol{e}}(T)| > |\boldsymbol{v_e}|$ is not possible because the extrusion trapezoidal planner will stop accelerating once $|\dot{\boldsymbol{S}}_{\boldsymbol{e}}|$ is equal to $|\boldsymbol{v_e}|$.

4.3.2 FECC using the CM and Trapezoidal Motion Planning

An example of $\dot{\boldsymbol{S}}_{\boldsymbol{c}}$ and $\dot{\boldsymbol{S}}_{\boldsymbol{e}}$ generated using the trapezoidal motion planner for points $\boldsymbol{p_{j-1}}$, $\boldsymbol{p_j}$, and $\boldsymbol{p_{j+1}}$ on $\boldsymbol{\Upsilon}$ is shown in Figure 4.1(c). This example is representative of a 90-degree turn of the DIW extrusion nozzle. The transient simulation of fluid flow from CM is combined with the motion planning of the trapezoidal planner to find the correct transient behavior in $\boldsymbol{\Upsilon}$. A new tool path, $\boldsymbol{\Upsilon_{new}}$, is created using the FECC where the $\boldsymbol{\Upsilon_{new}}$ Cartesian movement in the X, Y, and Z coordinate is the same as $\boldsymbol{\Upsilon}$ while the $\boldsymbol{\Upsilon_{new}}$ extrusion movement is changed to correct the error in material deposition predicted by the CM model [94]. In [94], only using the reference flowrate without additional control was shown to cause excess material deposition error in DIW.

The FECC performs this error correction by first taking the points $\{\boldsymbol{p_1}, \boldsymbol{p_2}, \dots, \boldsymbol{p_j}, \dots, \boldsymbol{p_n}\}$ on a $\boldsymbol{\Upsilon}$, Figure 4.1(a) and (b), and uses the dual trapezoidal motion planners to generate both

$\dot{\boldsymbol{S}}_{\boldsymbol{c}}(t)$ and $\dot{\boldsymbol{S}}_{\boldsymbol{e}}(t)$, Figure 4.1(c). $\dot{\boldsymbol{S}}_{\boldsymbol{e}}(t)$ is converted into a reference flowrate vector, $\boldsymbol{Q}_{\boldsymbol{r}}(t)$, representing the ideal flowrate desired by the trapezoidal motion planning, Equation (4.14).

$$\boldsymbol{Q}_{\boldsymbol{r}} = wh\,\dot{\boldsymbol{S}}_{\boldsymbol{e}} \tag{4.14}$$

where w is the width and h is the height of fluid deposition in $\boldsymbol{\Upsilon}$.

$\boldsymbol{Q}_{\boldsymbol{r}}$ is the input of an iterative quadratic linear regulator (iLQR) controller. The control diagram for the iLQR, CM model, and machine learning model is shown in Figure 4.2(a). The iLQR controller is an extension of the popular LQR used for optimal feedback control of linear systems to nonlinear systems. iLQR operates in two steps: first, it iteratively linearizes the system dynamics about an initial guess of the optimal control; and second, it computes an update to the optimal control and updates the initial guess. This process is repeated until convergence [95]. iLQR comes with convergence guarantees,= and the computed control law is globally optimal for linear dynamics with convex costs and locally optimal for nonlinear dynamics with convex costs. In this study, iLQR is utilized to find the control flowrate vector $\boldsymbol{Q}_{\boldsymbol{c}}$ that minimizes the convex quadratic cost function [95]:

$$COST = \boldsymbol{Q}_{\boldsymbol{e}}\boldsymbol{G}\boldsymbol{Q}_{\boldsymbol{e}}^{\boldsymbol{T}} + \boldsymbol{Q}_{\boldsymbol{c}}\boldsymbol{R}\boldsymbol{Q}_{\boldsymbol{c}}^{\boldsymbol{T}} \tag{4.15}$$

where $\boldsymbol{Q}_{\boldsymbol{e}}$ is the flowrate error vector, $\boldsymbol{G}$ is the error cost factor matrix, and $\boldsymbol{R}$ is the control cost factor matrix.

The iLQR controller requires (potentially many) evaluations of the system dynamics to both linearize and compute updates of the control law [96]. Using the CM model to calculate the output flowrate vector, $\boldsymbol{Q}_{\boldsymbol{o}}$, repeatedly leads to excessive computation time for the iLQR controller. To speed up the optimization in iLQR, a neural network was used to generate a machine learning model that could estimate the output flowrate vector of the CM model, denoted as $\boldsymbol{Q}_{\boldsymbol{m}}$. The neural network was trained and validated outputs from the CM model generated by

simulating tool paths without control. The neural network used random data division, the Levenberg-Marquardt training method, and mean squared error performance checking (nntraintool in Matlab^{TM} R2019B). Once trained, $\boldsymbol{Q_m}$ was used to calculate $\boldsymbol{Q_e}$ for the cost function in Equation (4.15).

$$\boldsymbol{Q_e} = \boldsymbol{Q_r} - \boldsymbol{Q_m} \tag{4.16}$$

Once an optimal $\boldsymbol{Q_c}$ was found for a given $\boldsymbol{Q_r}$ using $\boldsymbol{Q_m}$, the optimal $\boldsymbol{Q_c}$ was validated with the CM model to ensure that no significant errors were introduced by the machine learning model. An illustration of the DIW system without any control where $\boldsymbol{Q_r}$ is the same as $\boldsymbol{Q_c}$ as determined by the extrusion trapezoidal motion planner is shown in Figure 4.2(b) and compared against the DIW system with the iLQR controller in Figure 4.2(c) for a 90-degree turn. Results in Section 5 will further illustrate the changes made by iLQR controller for the 90-degree turn. Without iLQR, the flowrate from the extrusion trapezoidal motion planner (output from the progressive cavity pump to be described in Section 4.1) is $|\boldsymbol{Q_r}|$. Compared to the targeted flowrate $|\boldsymbol{Q_r}|$, $|\boldsymbol{Q_o}|$ has a significant amount of error. With iLQR, the output from the pump (and input to the static mixer and nozzle) is adjusted to $|\boldsymbol{Q_c}|$ in Figure 4.2(c).

In FECC, a new time series extrusion velocity path, $\dot{\boldsymbol{S}}_{\boldsymbol{e,new}}$, is created using Eq (4.14) based on the optimized $\boldsymbol{Q_c}$. The combination of $\dot{\boldsymbol{S}}_{\boldsymbol{e,new}}$ and unchanged $\dot{\boldsymbol{S}}_{\boldsymbol{c}}$ creates the subsets for a new corrected tool path $\boldsymbol{\Upsilon_{new}}$. This study focuses only on the effect of pump flowrate control, the Cartesian coordinates of $\boldsymbol{\Upsilon_{new}}$ remain the same; but the flowrate in the extrusion coordinate is adjusted. For example, in Figure 4.2(d), the Cartesian path of $\boldsymbol{\Upsilon_{new}}$ is the same as $\{\boldsymbol{p_{j-1}}, \boldsymbol{p_j}, \boldsymbol{p_{j+1}}\}$. In Figure 4.2(e), the flowrate within points $\{\boldsymbol{p_{j-1}}, \boldsymbol{p_j}, \boldsymbol{p_{j+1}}\}_{\boldsymbol{new}}$ was adjusted in the E coordinate based on iLQR controller output. New points $\{\boldsymbol{p_i}, \boldsymbol{p_{ii}}, \dots, \boldsymbol{p_k}, \dots, \boldsymbol{p_m}\}_{\boldsymbol{new}} \subset \{\boldsymbol{p_{j-1}}, \boldsymbol{p_j}, \boldsymbol{p_{j+1}}\}$ follow the same Cartesian tool path (Figure 4.2(d)) but has different extrusion

flowrate (Figure 4.2(e)) are identified. In summary, $\{\dot{\boldsymbol{S}}_{\boldsymbol{c}}, \dot{\boldsymbol{S}}_{\boldsymbol{e,new}}\} \subset \boldsymbol{\Upsilon}_{\boldsymbol{new}} \subseteq \{\boldsymbol{p}_{\boldsymbol{i}}, \boldsymbol{p}_{\boldsymbol{ii}}, \dots, \boldsymbol{p}_{\boldsymbol{k}}, \dots, \boldsymbol{p}_{\boldsymbol{m}}\}_{\boldsymbol{new}}$.

Points $\{\boldsymbol{p}_{\boldsymbol{i}}, \boldsymbol{p}_{\boldsymbol{ii}}, \dots, \boldsymbol{p}_{\boldsymbol{k}}, \dots, \boldsymbol{p}_{\boldsymbol{m}}\}_{\boldsymbol{new}}$ subdivide the Cartesian space $\boldsymbol{S}_{\boldsymbol{c,new}}$ into segments. In this study, $\boldsymbol{S}_{\boldsymbol{c,new}}$ is segmented with a length of λ, as shown in Figure 4.2(d), between two adjacent points in $\{\boldsymbol{p}_{\boldsymbol{i}}, \boldsymbol{p}_{\boldsymbol{ii}}, \dots, \boldsymbol{p}_{\boldsymbol{k}}, \dots, \boldsymbol{p}_{\boldsymbol{m}}\}_{\boldsymbol{new}}$ in the Cartesian space. There is a practical limit on the resolution of subdivisions in $\boldsymbol{S}_{\boldsymbol{c,new}}$ due to the limitation of the microprocessor in the DIW machine.

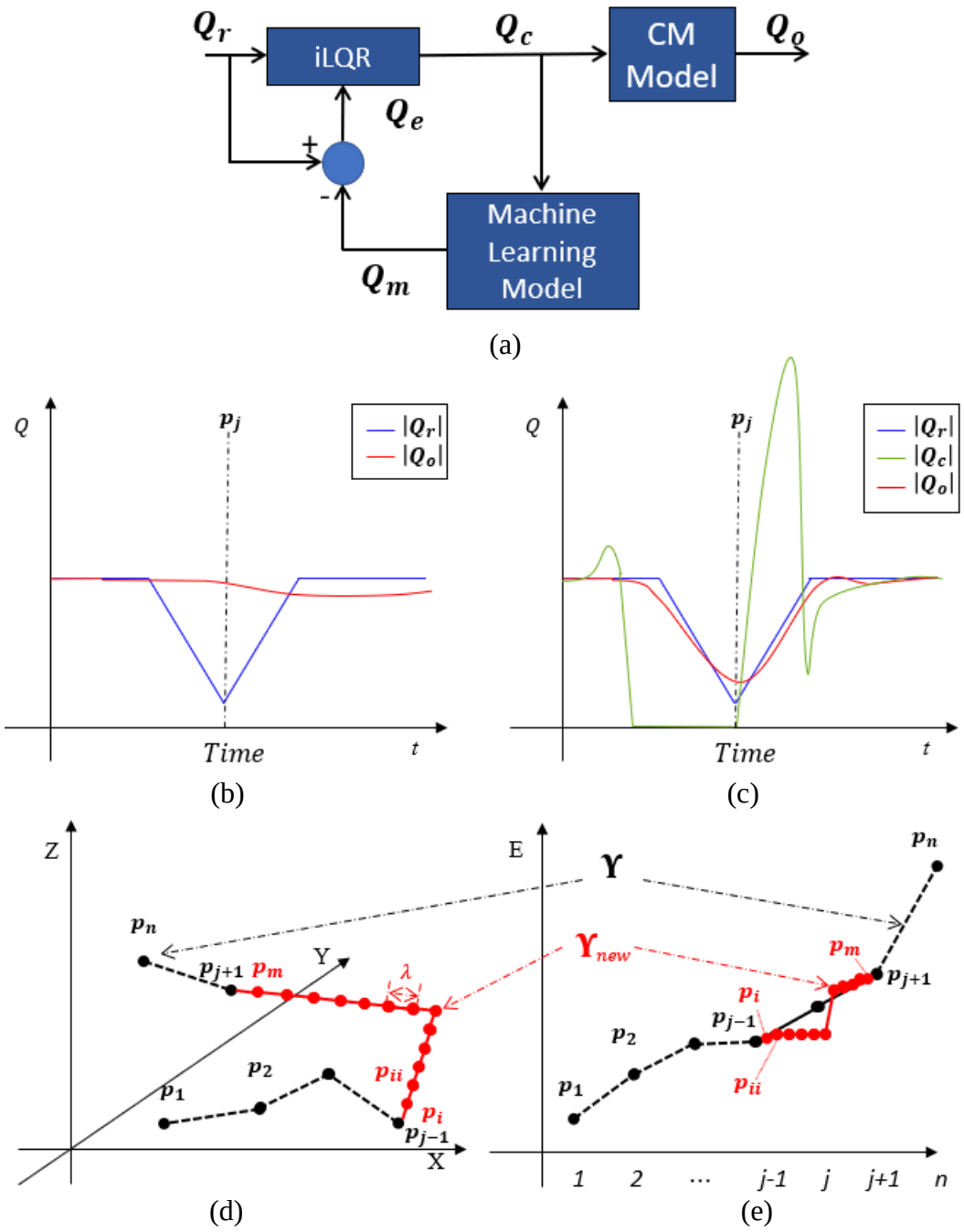

Figure 4.2: (a) iLQR controller in the CM model with machine learning model diagram. The DIW system flowrate (b) without control and (c) with iLQR control. The new points, $\{\boldsymbol{p_i}, \boldsymbol{p_{ii}}, \dots, \boldsymbol{p_k}, \dots, \boldsymbol{p_m}\}_{\boldsymbol{new}}$, that produce an approximation of $\boldsymbol{\Upsilon_{new}}$ specified by $\{\dot{\boldsymbol{S}}_{\boldsymbol{c}}, \dot{\boldsymbol{S}}_{\boldsymbol{e,new}}\}$ in (d) the Cartesian and (e) the extrusion coordinates.

4.3.3 FECC insertion and replication

For DIW, only the turning points and short sections of the extrusion nozzle tool path $\boldsymbol{\Upsilon}$ need to be corrected by FECC to adjust the material flowrate in the nozzle. The $\boldsymbol{\Upsilon}$ for DIW is created through a process called slicing, where a 3D model is subdivided into layers, and an extrusion nozzle motion path for each layer is created [97]. Subsegments of the $\boldsymbol{\Upsilon}$ with geometric shape of a corner and a U-turn found in a zigzag infill pattern are investigated in this study. This process could be expanded to any arbitrary geometric feature that repeatedly occur in a DIW tool path [97]. In this study, FECC is performed a 90-degree turn defined by three points $\boldsymbol{p_{t1}}$, $\boldsymbol{p_{t2}}$, and $\boldsymbol{p_{t3}}$ in Figure 4.3(a), and the U-turn defined by four points $\boldsymbol{p_{u1}}$, $\boldsymbol{p_{u2}}$, $\boldsymbol{p_{u3}}$, and $\boldsymbol{p_{u4}}$ in Figure 4.3(b),

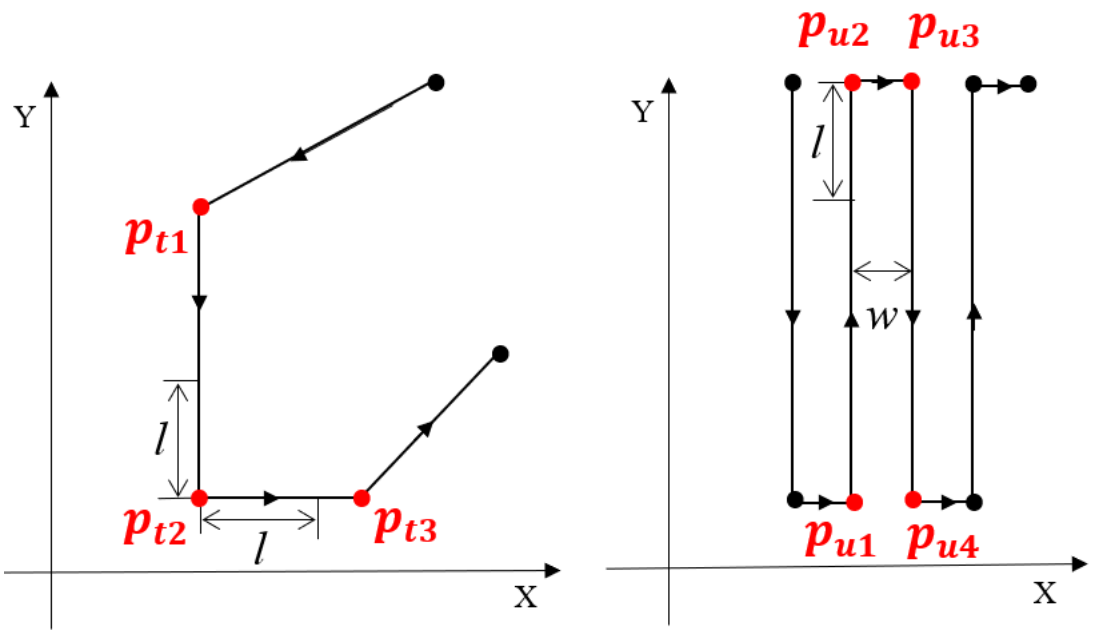

Figure 4.3: (a) The 90-degree turn and (b) the U-turn geometric features in a zigzag infill tool path.

To find every instance of the 90-degree turn in $\boldsymbol{\Upsilon}$, the entirety of $\boldsymbol{\Upsilon}$ is searched for sequential sets of 3 points, $\{\boldsymbol{p_{j-1}}, \boldsymbol{p_j}, \boldsymbol{p_{j+1}}\}$, to meet the following three criteria:

$$\angle\{\boldsymbol{p_{j-1}}, \boldsymbol{p_j}, \boldsymbol{p_{j+1}}\} = 90° \tag{4.17}$$

$$|\boldsymbol{p_{j-1}p_j}| > l \tag{4.18}$$

$$|\boldsymbol{p_j p_{j+1}}| > l \tag{4.19}$$

where l is a minimum distance that needs to be traveled by the DIW nozzle before it reached a steady-state velocity.

To find every instance of the U-turn in $\boldsymbol{\Upsilon}$, the entirety of $\boldsymbol{\Upsilon}$ is searched for sequential sets of 4 points $\{\boldsymbol{p_{j-1}}, \boldsymbol{p_j}, \boldsymbol{p_{j+1}}, \boldsymbol{p_{j+2}}\}$ that meet the following criteria:

$$\overline{\boldsymbol{p_{j-1}p_j}} \parallel \overline{\boldsymbol{p_{j+1}p_{j+2}}} \tag{4.20}$$

$$|\boldsymbol{p_{j-1}p_j}| > l \tag{4.21}$$

$$|\boldsymbol{p_{j+1}p_{j+2}}| > l \tag{4.22}$$

$$|\boldsymbol{p_j p_{j+1}}| = w \tag{4.23}$$

Once an instance of a geometric feature is found, the precalculated FECC $\boldsymbol{\Upsilon_{new}}$ for that shape is inserted into the $\boldsymbol{\Upsilon}$ centered at the point $\boldsymbol{p_{t2}}$ for the 90-degree turn shown in Figure 4.3(a) and point $\boldsymbol{p_{u2}}$ for the U-turn shown in Figure 4.3(b).

4.4. Experimental Setup in DIW and Tool paths

The FECC experiment was conducted on a custom-built DIW system by printing tool paths with 90-degree turns and U-turns to compare the excess material deposition with and without FECC. The FECC was then applied to a test part with a $\boldsymbol{\Upsilon}$ that contained multiple 90-degree turn and U-turn geometric features.

4.4.1 DIW system

The DIW machine, as shown in Figure 4.4, has a PDP and is based on a CoreXY design [86,87]. The PDP, Figure 4.4(a), is a dual progressive cavity pump (Vipro-Head 3/3, Viscotec, Toeging am Inn, Germany) that can dispense two high viscosity fluids precisely with rotors forcing fluid through small cavities in a stator. This fluid dispensing method has no pulsing, and the amount of fluid dispensed is directly controlled by the motor rotation [79]. The CoreXY gantry, Figure 4.4(b), uses two stepper motors and belts to control the X and Y positions of the extrusion nozzle on PDP. The Z position of the extrusion nozzle is controlled by a movable print bed driven by a pair of lead screws attached to stepper motors. The control board is a RAMBo 1.4 (Ultimachine, South Pittsburg, TN, USA). An open-source firmware (Marlin Firmware v1.1.9) that uses a trapezoidal motion planner, as described in Section 3.2, controls the DIW system by taking points in the form of G-code and translating them into velocities for the motors.

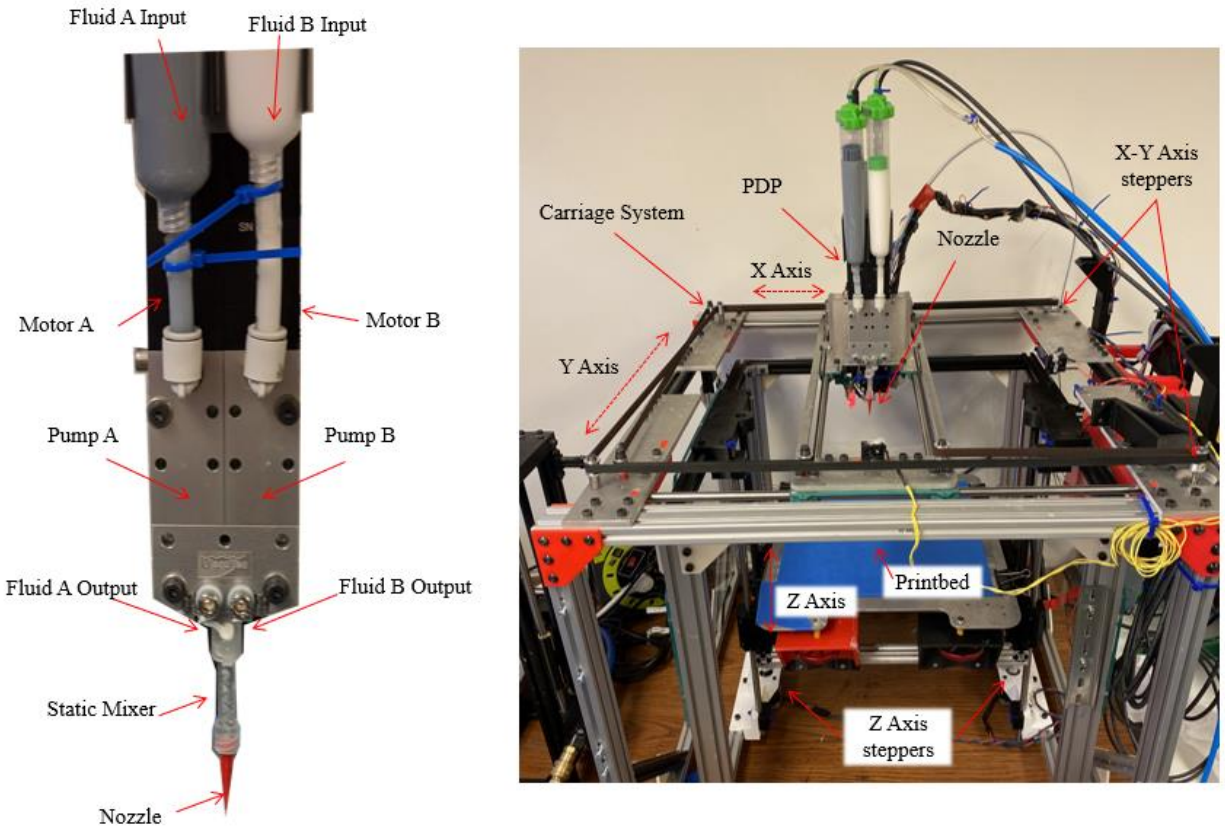

(a) (b)

Figure 4.4: (a) The PDP and (b) gantry system for the DIW system.

A static mixer performs the in-situ mixing of two fluids dispensed by the PDP, enabling the use of two-part silicones. The static mixer attached to the PDP is custom designed and 3D-printed to reduce the pressure drop along its length as described in Chapter 2, Figure 4.5(a). The overall dimensions of the static mixer and tapered dispensing nozzle can be seen in Figure 4.5(b). The 3D-printed static mixer has a L of 50 mm, D of 3 mm, K_l of 5.5 and, K_G of 28 [84]. A tapered dispensing nozzle is attached to the static mixer end has a L of 20 mm, D_{in} of 3 mm, D_{out} of 0.25 mm, and K_G of 8. The K_l is 52.4 as determined by using Equation (3.19).

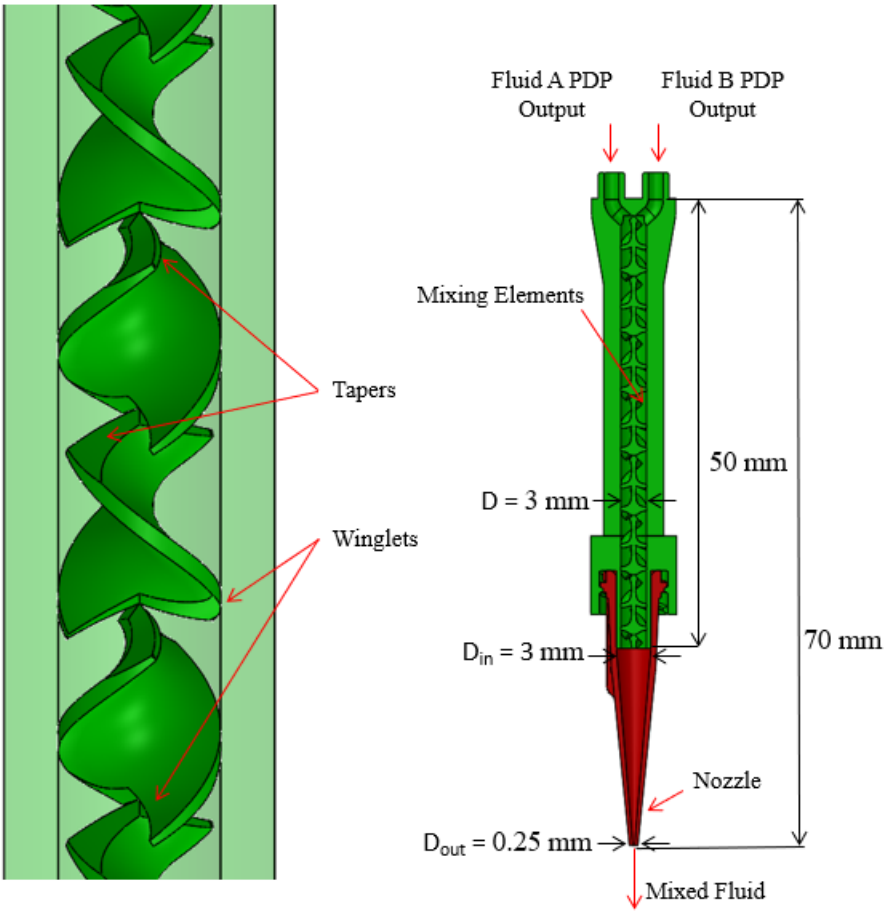

(a) (b)

Figure 4.5: (a) The static mixer with 3D-printed mixing elements to reduce its pressure drop and (b) dimensions of the static mixer and tapered dispensing nozzle.

4.4.2 The CM Model, iLQR Controller, and Machine Learning Model

The CM model used for the FECC is based on the open-source one-dimensional water hammer code by Jensen et al. [59] and modified to simulate the transient flow in DIW [94]. The fluid used in the study is a two-part alkoxysilicone (Dow Inc. Midland, MI, USA) that, when mixed, has a k =650 Pa-s^n, n =0.6, ρ =1295 kg/m^3, and a =880 m/s as provided by Dow. The L, D, K_g, and K_L of the static mixer and tapered nozzle were used for the CM model. The ΔX and Δt was 1.75x10^{-5} m (4000 nodes) and 1.98x10^{-8} s, respectively, as determined by grid independence convergent testing.

The iLQR controller was run in Matlab™ (R2019B) and adapted from the program in [98] to work with the machine learning model and the CM model. The machine learning model was a fully connected neural network with ten hidden layers that were trained, tested, and validated using a data set of 22,000 $\boldsymbol{Q_r}$, input pressure, $\boldsymbol{P_r}$, and $\boldsymbol{Q_o}$ generated a variety of simulated CM model tool paths, Figure 4.6. The data were randomly divided, with 70% used for training, 15% used for testing, and 15% used for validation. The trained machine learning model computed 1 second of transient fluid flow in 6 seconds compared to the 440 min the CM model requires on a computer with an Intel Xeon W-2145 CPU and 32 GB of RAM. The G and R used in the iLQR cost function were $20\boldsymbol{I}$ and $0.01\boldsymbol{I}$, respectively, where $\boldsymbol{I}$ is the identity matrix. These coefficients emphasize minimizing tracking error while regulating the control effort. The λ used for $\boldsymbol{\Upsilon_{new}}$ was 0.33mm, which was determined empirically to be the minimum length that could be used with the DIW machine's control board without causing command processing delays.

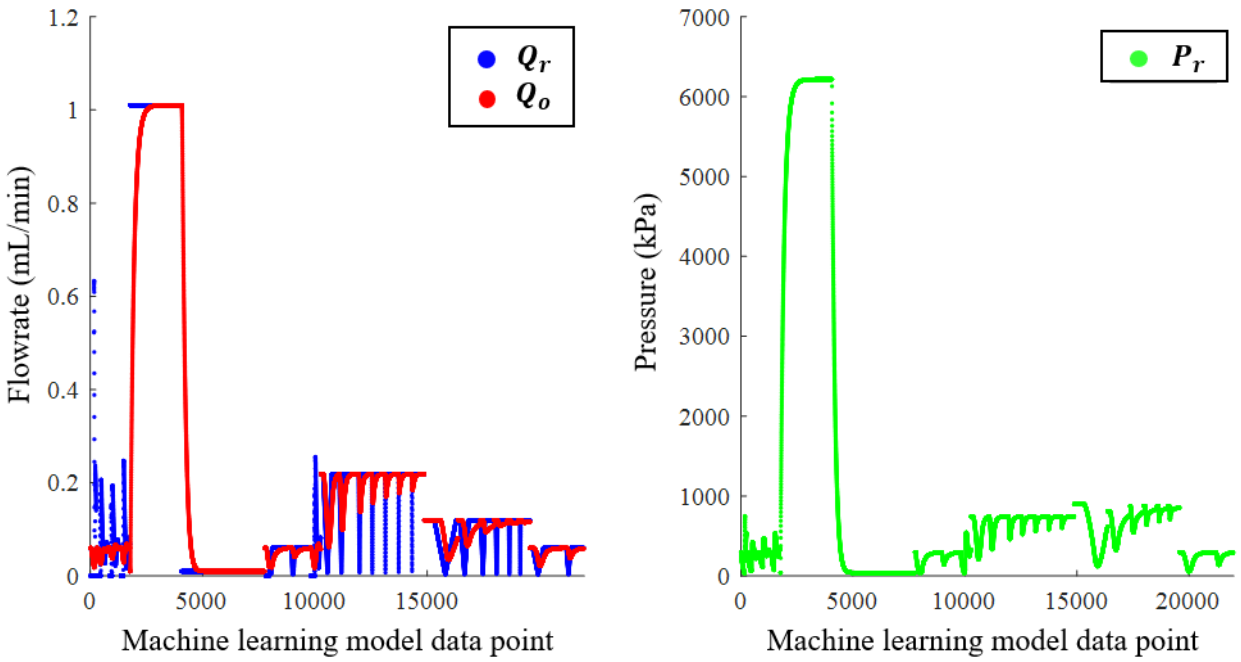

Figure 4.6: Training data for the machine learning model. The learned model was able to reproduce the CM model outputs effectively. For a 1 sec of simulation of transient fluid flow, the machine learning model takes approximately 6 sec of computation. In contrast, the CM model will take 440 min of computation on a computer with an Intel Xeon W-2145 CPU and 32 GB of ram.

4.4.3 Geometric Features and Geometric Features Test Part

The 90-degree turn and U-turn zigzag infill patterns used to study the effects of FECC are shown in Figure 4.7. In Figure 4.7(a), the 90-degree turn is denoted by points A, B, and C, with $|AB| = |BC| = l$ and $\angle\{A, B, C\} = 90°$. This satisfies the criteria given in Eqs. (4.17)-(4.19). In Figure 4.7(b), the U-turn is denoted by points A, B, C, and D with $|AB| = |CD| = l$, $|BC| = w$, and $\overline{AB} \parallel \overline{CD}$ which satisfy the criteria given in Eqs. (4.20)-(4.23).

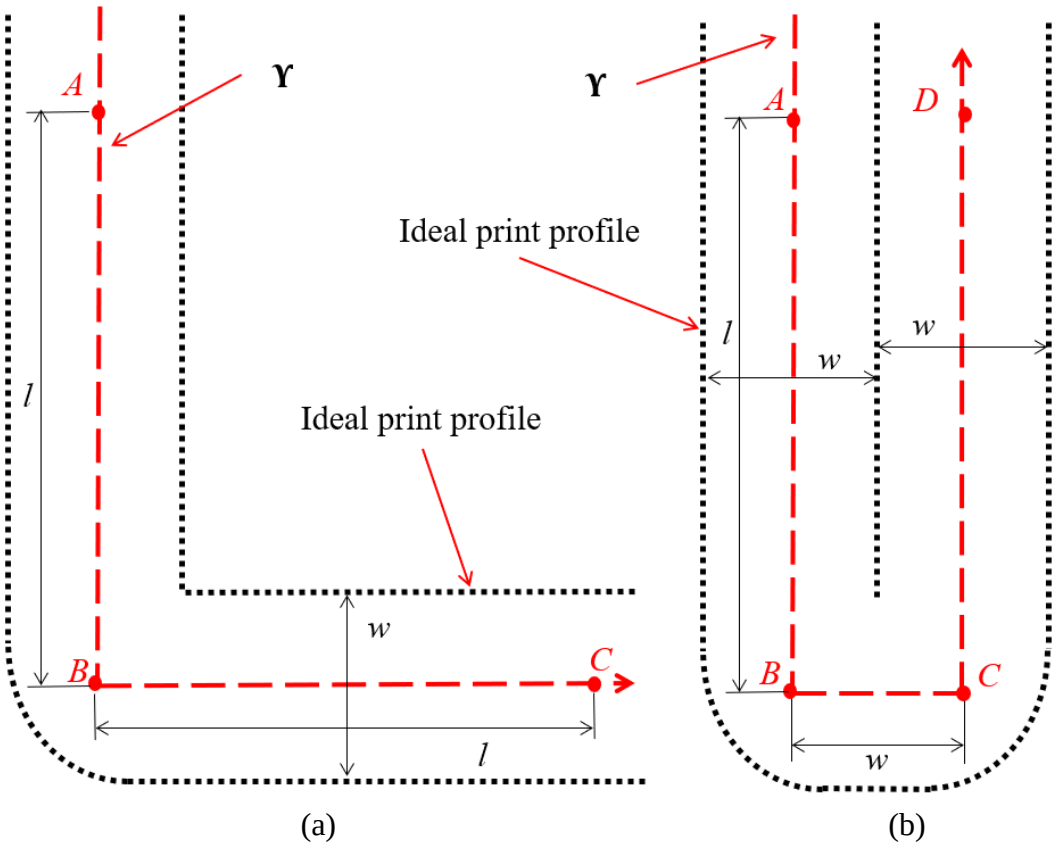

Figure 4.7: (a) The 90-degree turn and (b) the U-turn made by a zigzag infill pattern to study the effects of FECC.

The target print dimensions for both geometric features are w=0.3 mm, l=5 mm, and h=0.2 mm. For all the individual geometric feature tests, the DIW system had $|\boldsymbol{v_c}|$=25 mm/s, $|\boldsymbol{a_c}|$=500 mm/s^2, J=2mm/s, $|\boldsymbol{a_e}|$=500 mm/s^2, and J_e=2 mm/s. FECC is applied to the individual instance of a 90-degree turn and U-turn. The $\boldsymbol{\Upsilon}$ for both geometric features were generated by using the trapezoidal motion planners defined by Eqs. (4.1)-(4.13). The $\boldsymbol{\Upsilon}_{new}$ with sub points ($\{\boldsymbol{p_i}, \boldsymbol{p_{ii}}, \dots, \boldsymbol{p_k}, \dots, \boldsymbol{p_m}\}_{\boldsymbol{new}}$ in Section 3.2) for both the 90-degree turn and U-turn were generated following the FECC described in Section 3.3. The 90-degree turn and U-turn are printed using the DIW system five times without FECC and five times with FECC. In total, 20 tests were conducted.

To study the effect of FECC on DIW part quality, a test part was printed on the DIW system. The test part consists of a large base and a tall thin wall tower, as shown in Figure 4.8. The base of the test part is 127 mm long and 115 mm wide. The tower is 46 mm long, 32 mm wide, and 50 mm tall. Both the base and tower walls are 1.6 mm thick. The test part was printed with a w of 0.3 mm, a h of 0.2 mm, and a solid zigzag infill. This resulted in 8 layers on the base and 250 layers on the tower. The points that determined the $\boldsymbol{\Upsilon}$ were generated using a slicer (Cura 4.6, Ultimaker, Geldermalsen, Netherlands). The square corners of both the base and the test part's tower required the use of the 90-degree turn geometric feature, while the zigzag infill created repeated instances of the U-turn. Other than transitions, the $\boldsymbol{\Upsilon}$ mostly consisted of the 90-degree corner and U-turn geometric features used with FECC for this study. With these settings, the test part $\boldsymbol{\Upsilon}$ contained approximately 5000 90-degree turns and 8500 U-turns that will require FECC. The test part was printed once with FECC applied and once without it for a total of two test parts.

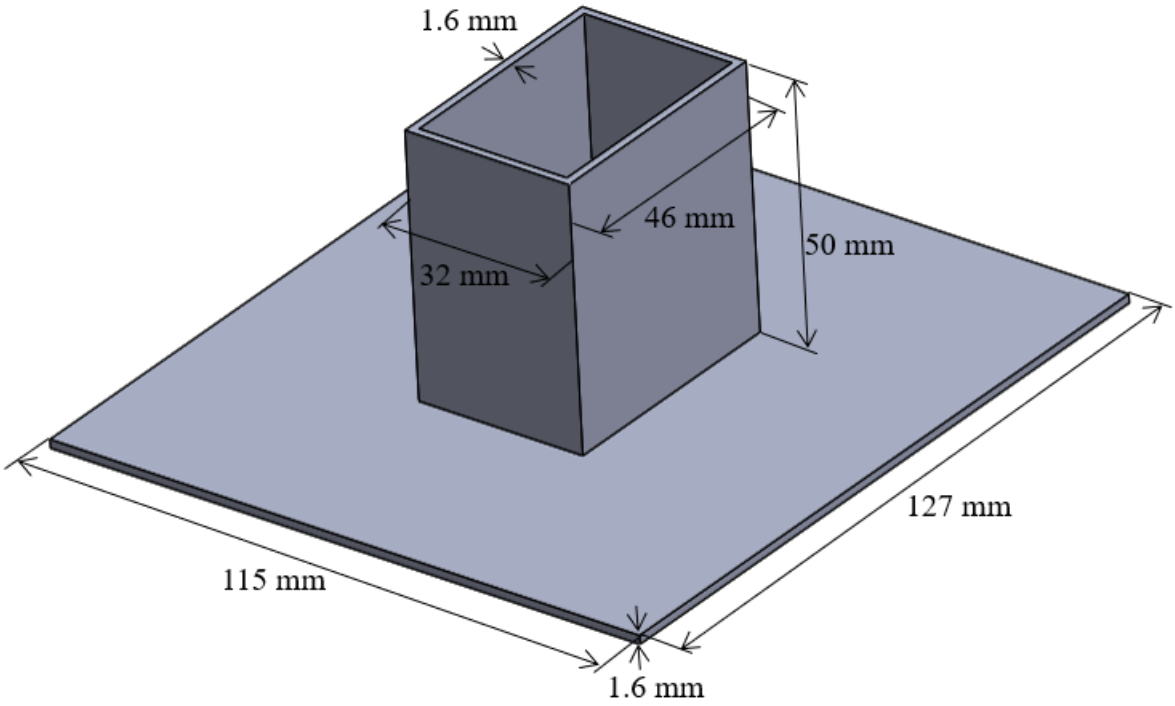

Figure 4.8: Test part used to determine FECC's effect on part quality.

4.4.4 Measurement of geometric features

After each geometric feature test, a picture was taken by a digital microscope camera (UWT500X020M, AmScope Irvine California) placed directly over the geometric feature. The microscope camera was calibrated with a caliper digital caliper (8000-F6, Products Engineering Corporation, Torrance California). Pictures of the 90-degree turn were processed using Matlab™ (R2019B) code used previously to validate the CM model [94]. In short, the Matlab™ (R2019B) script detects the edges of the 90-degree turn and fits a circle at the bulge at the corner. The corner bulge size is defined as the diameter of the material deposited at point B in Figure 4.7(a). For the 90-degree turn, the diameter of the circle at the corner is used to quantify the quality of the DIW in a 90-degree turn using the method detailed in [94]. The location of the bulge relative to point B in Figure 4.7(a) is also found but based on the results in [94] it is not expected to be affected by FECC. The ideal diameter of the 90-degree corner bulge is equal to $w\left(\frac{1+\sqrt{2}}{2}\right)$, which is the diagonal created by a circle of diameter w and square with a side length of $\frac{w}{2}$ that has a corner

at the center of the circle. Here, for w=0.3 mm, the ideal bulge diameter is 0.36 mm. The error of the corner bulge is calculated by comparing the percentage difference in measured diameter to the ideal bulge diameter.

For the U-turn, a similar image processing procedure is used to measure the width of the bulge of the U-turn, as shown in Figure 4.9(a), in Matlab™ (R2019B). Instead of diameter, this width of the bulge is used to quantify the quality of the U-turn print because the shape of the deposition for the U-turn does not fit a circle well. The U-turn image is first converted into a binary (im2bw) using the background of the image as the threshold value, Figure 4.9(b). Second, the image boundary is found using the edge detection algorithm (bwboundaries), Figure 4.9(c). The print boundary is smoothed with a 61st order Savitzky-Golay filter (sgolayfilt) with a frame length of 10 mm to find the edges of the print, Figure 4.9(d). The Savitzky-Golay filter was used because the sharp pixel edges of the unfiltered image boundary would sometimes produce errors with the next step, requiring manual intervention.

(a) (b) (c) (d)

Figure 4.9: a) The microscope image, (b) the binary image of the background and the foreground, (c) the edge detection of the binary image, and (d) the boundary lines smoothed using the Savitzky-Golay filter.

As shown in Figure 4.10, the edges of the print profile are averaged to estimate the U-turn's centerline. Two lines are created that are parallel to the centerline and tangent to the bulge

on the left and right, respectively. The distance between these parallel lines is the bulge's width, which is marked as *b*, and compared between tests with and without FECC.

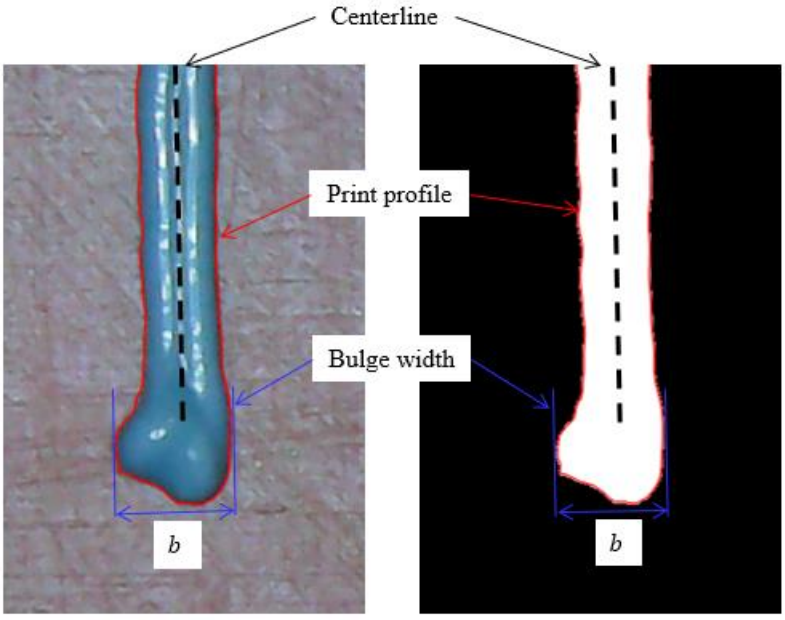

Figure 4.10: A processed image of the U-turn showing the print profile, the centerline, and the tangent lines to the bulge that measure its width b.

The width of the U-turn, as shown in Figure 4.7(b), is 2*w*. In this study, *w*=0.3 mm and the ideal bulge size for the U-turn is 0.6 mm. The error of the U-turn e is calculated by comparing the percentage difference in measured width to the ideal width. The U-turn bulge's location relative to the ideal geometry, Figure 4.7(d), is not found.

4.5. Results

Results of the FECC corrections to the 90-degree corner, U-turn, and test part are presented.

4.5.1 FECC of the 90-degree Corner

The flowrate for the 90-degree corner with and without FECC can be seen in Figure 4.11. The motion of the 90-degree corner Υ was determined using the trapezoidal planners described

in Section 3.1 and the w, l , h , $|\boldsymbol{v_c}|$, $|\boldsymbol{a_c}|$, J, $|\boldsymbol{a_e}|$, and J_e values given in Section 4.1. The FECC was done according to the procedure shown in Section 3.2 using the k, n, ρ, a, L, D, D_{in}, D_{out}, K_g, K_L, ΔX, Δt, E, R, λ, and machine learning model is given in Section 4.2.

Figure 4.11(a) shows the $\boldsymbol{\Upsilon}$ without FECC. The trapezoidal motion planner sets the target flowrate $|\boldsymbol{Q_r}|$ which has a steady-state flowrate of 0.06 mL/min approximately 0.05 s before reaching point B, the 90-degree turning point in Figure 4.7(a). $|\boldsymbol{Q_r}|$ linearly drops to 0 at point B and linearly increases to the same 0.06 mL/min steady-state flowrate 0.05 s after passing point B. The CM modeling shows the output flowrate $|\boldsymbol{Q_o}|$ does not begin to noticeably change until after the $\boldsymbol{\Upsilon}$ has passed point B, this will result in bulging at the junctions for the 90-degree corner. Figure 4.11(b) depicts the system response with FECC where the same target flowrate $|\boldsymbol{Q_r}|$ computed from the trapezoidal motion planner is used. About 0.2 s before the nozzle reaches point B, $|\boldsymbol{Q_c}|$ is slightly increased to about 0.07 mL/min (above the 0.06 mL/min steady-state flowrate) and then suddenly dropped to 0.003 mL/min about 0.13 s before point B. The $|\boldsymbol{Q_c}|$ jumped to two peak values – about 0.17 mL/min at about 0.015 s and 0.25 mL/min at about 0.04 s after passing the point B – before dropping to zero again at 0.05 s and slowly increased back to the 0.06 mL/min steady-state flowrate.

The behavior of the control computed by the iLQR is typical of a bang-bang like control scheme. This behavior is common for optimal controllers where the relative emphasis on tracking performance is significantly higher than control effort. This emphasis is placed by choosing a relatively large value of $\boldsymbol{G}$ as compared to $\boldsymbol{R}$. Typical behavior profiles for bang-bang schemes involve choosing extreme control values (here resulting in close to zero and large output flowrates) and timing the switch between the two such that the tracking error is minimized. This is exemplified by the switching behavior depicted in Figure 4.11(b), where the output flowrate is

first zeroed out in anticipation of the dip in the extrusion path then rapidly increased between 1 and 1.05 s to match the return to the nominal value. A second zeroing out and steady increase in outflow is exhibited at 1.05 s to minimize any resulting overshoot that may occur as the flow returns to its nominal value. The complexity of the control law (involving multiple switches) is due to the system's significant nonlinearity. This control significantly improves performance, the 2-norm error [99] of $|\boldsymbol{Q_o}|$ with respect to $|\boldsymbol{Q_r}|$ is 0.32 mL/min and 0.16 mL/min without and with FECC respectively. Additionally, the iLQR controller reduced the $COST$ in Equation (4.15) from 2.11 to 0.70 mL^2/min^2. With the new $\boldsymbol{Q_c}$ from FECC, Figure 4.11(b), $\boldsymbol{Q_o}$ follows the $\boldsymbol{Q_r}$ much closer and will result in reduced bulging at the 90-degree turn.

This aggressive control profile proved effective for this system due to the fast response rate of the actuator. However, it is possible to produce a smoother control by reducing the relative magnitude of $\boldsymbol{G}$ as compared to $\boldsymbol{R}$. A smoother profile comes at the cost of tracking performance, translating into potentially larger bulges and degradation of part quality. A smoother profile is typified by slower transitions between control extremes and increased transient times.

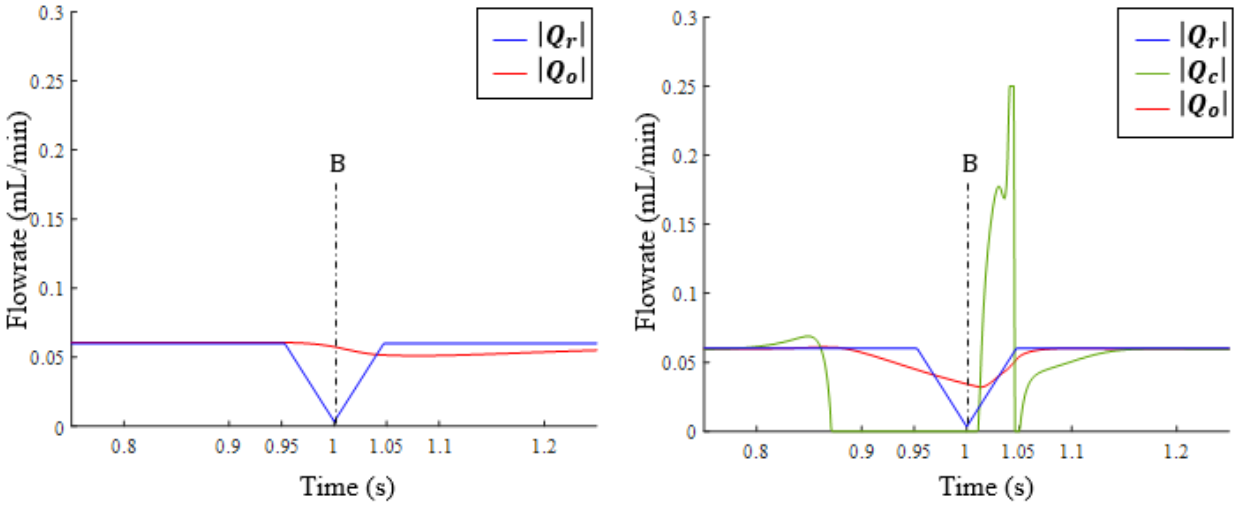

(a) (b)

Figure 4.11: Volumetric flowrates from CM of the 90-degree turn (a) without and (b) with FECC.

Examples of images of the 90-degree turn without and with FECC can be seen in Figure 4.12. The bulging is seen on the 90-degree turn without FECC, Figure 4.12(a), is reduced noticeably when FECC is applied, Figure 4.12(b), as predicted by the reduction in 2-norm error.

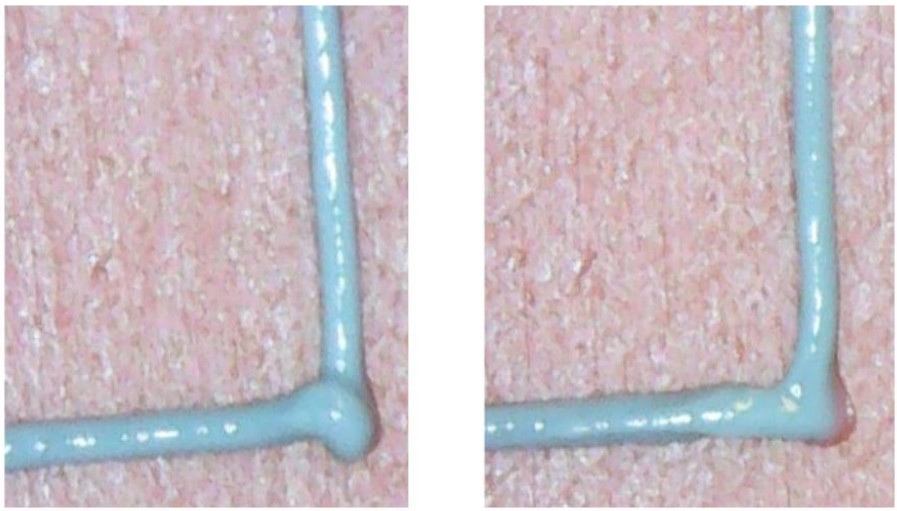

(a) (b)

Figure 4.12: The 90-degree corner (a) without and (b) with FECC.

Analysis of images of 90-degree corners following the procedure in [94] reveals that the diameter of the bulging was 0.63±0.03 mm without FECC and 0.48±0.03 mm with FECC. The ideal diameter for the 90-degree corner is 0.36 mm, giving the FECC a 40% average reduction in error for the 90-degree turn. The data for both the bulge measurements and error can be seen below in Table 4.1. With and without FECC, the offset of the detected bulge diameter is about the same at 0.11 mm as expected based on the results in [94].

Table 4.1: Bulge diameter data for the 90-degree corner without and with FECC

Without FECC			With FECC		
Sample	Diameter (mm)	% Error	Sample	Diameter (mm)	% Error
1	0.61	69.4	1	0.45	25.0
2	0.63	75.0	2	0.48	33.3
3	0.62	72.2	3	0.46	27.8
4	0.68	88.9	4	0.56	55.6
5	0.63	75.0	5	0.50	38.9
Average	0.63	76.1	Average	0.49	36.1

4.5.2 FECC of the U-Turn

The flowrate for the U-turn with and without FECC can be seen in Figure 4.13. The motion of the U-turn $\boldsymbol{\Upsilon}$ was determined using the trapezoidal planners described in Section 3.1 and the w, l, h, $|\boldsymbol{v_c}|$, $|\boldsymbol{a_c}|$, J, $|\boldsymbol{a_e}|$, and J_e values given in Section 4.1. The FECC was done according to the procedure shown in Section 3.2 using the k, n, ρ, a, L, D, D_{in}, D_{out}, K_g, K_L, ΔX, Δt, E, R, λ, and machine learning model is given in Section 4.2.

In Figure 4.13(a) with no FECC, the trapezoidal motion planner sets the target flowrate $|\boldsymbol{Q_r}|$ which has a steady-state 0.06 mL/min flowrate approximately 0.05 s before reaching point B, the first turn in the U-turn in Figure 4.7(b). $|\boldsymbol{Q_r}|$ linearly drops to 0.003 mL/min at point B, linearly increases and decreases between points B and C, drops to 0.003 mL/min at point C, and then linearly increases to 0.06 mL/min steady-state flowrate 0.05 s after passing point C. The CM modeling shows the output flowrate $|\boldsymbol{Q_o}|$ does not begin to noticeably change until after the $\boldsymbol{\Upsilon}$ has passed point B, this will result in increased width at the U-turn end. Additionally, $|\boldsymbol{Q_o}|$ remains about 0.01 mL/min below $|\boldsymbol{Q_r}|$ for 0.2 s after passing point C. Figure 4.13 (b) depicts the response of the system with FECC where the same target flowrate $|\boldsymbol{Q_r}|$ computed from the trapezoidal motion planner is used.

The iLQR exhibits the same bang-bang like behavior as the 90-degree turn. At 0.8 s, the flow is first increased before zeroing out rapidly in anticipation of the dip in the target signal. This counter-intuitive profile results from the nonlinearity of system dynamics and the

complexity of the extrusion path and emphasizes the need for predictive controllers such as the iLQR. The double-peak profile between 1.05 and 1.1 s is due to driving the flowrate back to its nominal while minimizing the overshoot in the return. These two peaks are similar to the behavior exhibited for the 90-degree turn, Figure 4.11(b), only significantly more pronounced with a dip of flow to zero. Interestingly, the optimal control profile exhibits a small amount of overshoot, favoring a faster response at the cost of this overshoot in tracking. The 2-norm error of $|\boldsymbol{Q_o}|$ with respect to $|\boldsymbol{Q_r}|$ is 0.43 and 0.18 mL/min for the U-turn without and with FECC, respectively, demonstrating a significant performance improvement. Additionally, the iLQR controller reduced the $COST$ in Equation (4.15) from 3.70 to 0.82 mL^2/min^2.

It is possible to produce a smoother control, identical to the approach outlined for the 90-degree turn case. The resulting smooth controller will result in poorer tracking performance but reduce the rapid rise and dip in flowrate and possibly moving the peaks.

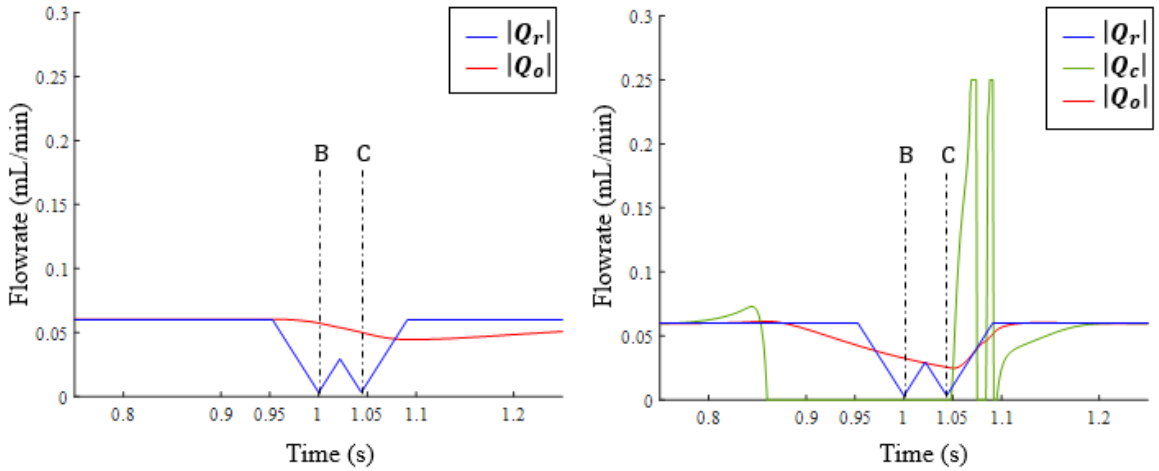

Figure 4.13: Volumetric flowrates from CM of the U-turn (a) without and (b) with FECC applied.

Examples of the U-turn without and with FECC can be seen in Figure 4.14. From inspection of the example images, the bulging seen on the geometric features without FECC,

Figure 4.14(a), is reduced significantly when FECC is applied, Figure 4.14(b), as predicted by the reduction in 2-norm error. Analysis of the U-turn images following the procedure in Section 4 reveals that the size of the width for the U-turn was 0.98±0.04 mm without FECC and 0.82±0.03 mm with FECC. The U-turn's ideal width is 0.6 mm, giving the FECC process a 25.7% reduction in error for the U-turn. The data for both the width measurements and error can be seen in Table 4.2.

(a) (b)

Figure 4.14: The U-turn (a) without and (b) with FECC.

Table 4.2: Bulge width data for the U-turn without and with FECC

Without FECC			With FECC		
Sample	Width (mm)	% Error	Sample	Width (mm)	% Error
1	1.03	71.6	1	0.86	43.3
2	1.01	68.3	2	0.79	31.7
3	0.97	61.6	3	0.79	31.7
4	0.98	63.3	4	0.82	36.7
5	0.90	50.0	5	0.86	43.3
Average	0.98	63.0	Average	0.82	37.3

4.5.3 FECC Test Part

The reduction of bulging in the geometric features will translate to improved quality of the test part with FECC applied across the entire part following the procedure described in

Section 4.3. In Figure 4.15, the test part without FECC can be seen on the left, and the test part with FECC (for 5000 90-degree corners and 8,500 U-turns) is on the right. The collective reduction in errors at 90-degree turns and U-turns has significantly improved part. The FECC test part has noticeably improved surface finish on both the base and tower portions of the print, as well as significantly reduced bulging at the corners on the tower and excess material at the edge of the base.

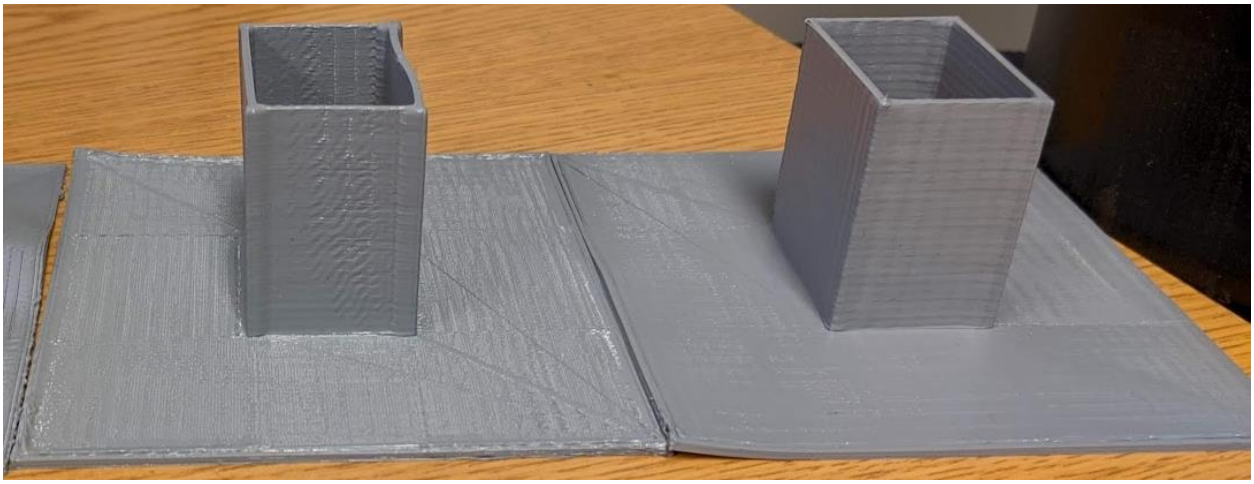

Figure 4.15: The test part without FECC on the left and with FECC on the right

Close-up inspection of the regions of notable improvement can be seen in Figure 4.16. Figure 4.16(a) shows the corner of the tower without FECC that has a bulging on what should be an instance of the 90-degree corner. Figure 4.16(b) is the same region on the test part tower with FECC where the bulging is no longer noticeable. Figure 4.16(c) is a zoomed picture of the base's edge where excess material is deposited at the location of the U-turn used to fill in the inner region of the base. The bulging of the U-turn has resulted in a ridge of material building up and deforming the base's perimeter while leaving gaps on the infill. Figure 4.16(c) is the close-up of the same base region for the FECC test part. While still noticeable, the ridge of excess material is significantly reduced, the perimeter of the part is not deformed, and gaps in the infill are reduced.

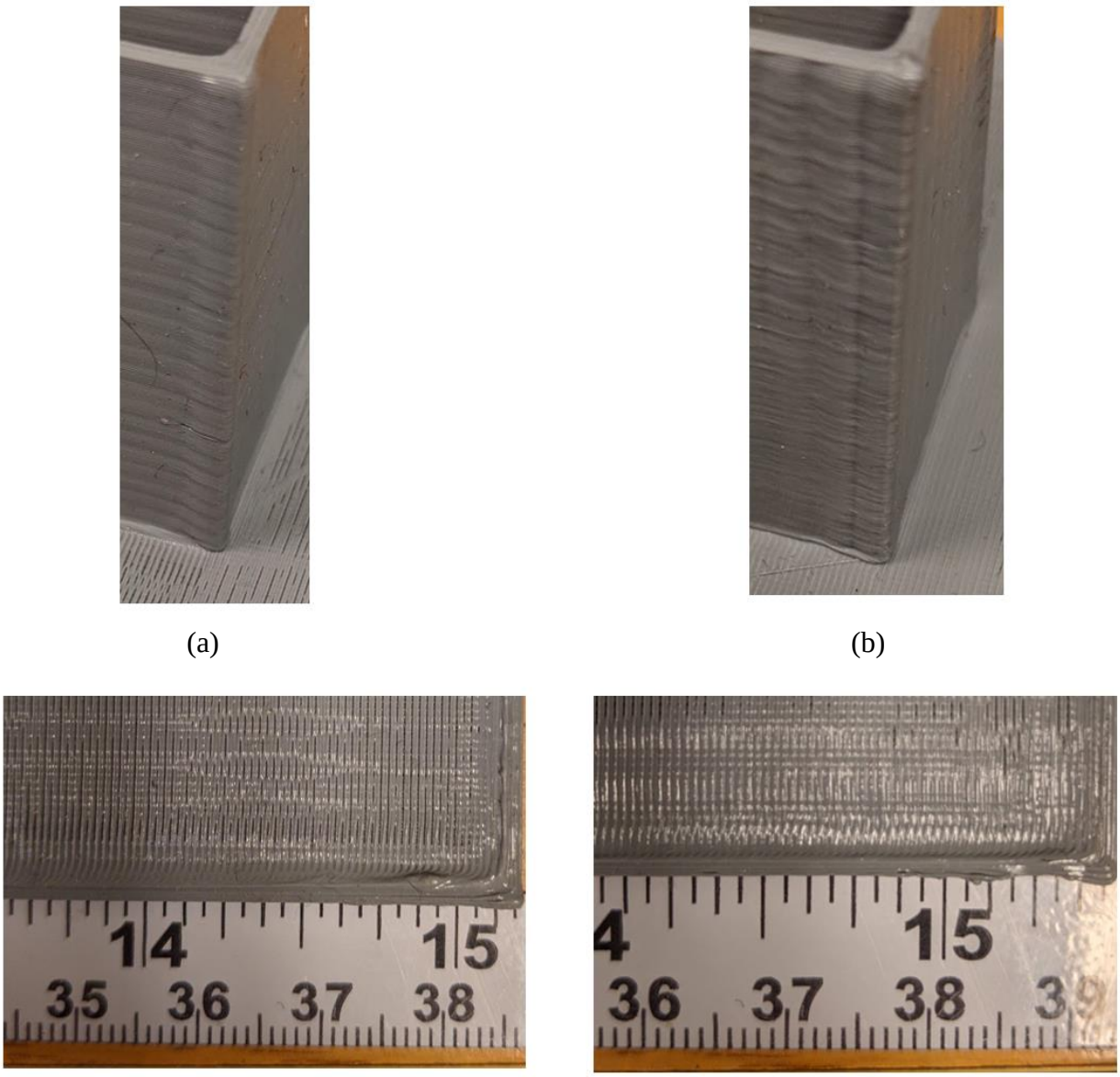

Figure 4.16: (a) A bulging tower corner of the test part without FECC and (b) the same corner on the test part with FECC where the bulging is no longer noticeable. (c) A zoomed-in region of the test part base without FECC where gaps in the material are seen and excess material is built up around the edges. (d) The same test part base region on the test part with FECC applied where the number of gaps and the material built up on the edges is reduced.

4.6. Conclusions and Future Work

The FECC was demonstrated to have a meaningful impact on the quality of DIW geometric features and parts. FECC included the CM model, trapezoidal motion planning, machine learning, and iLQR feedback control. The iLQR controller created a principled way of

deriving an optimal controller for the DIW system. While the machine significantly reduced the total computation time required by the iLQR controller.

FECC was able to reduce error at the junctions for a 90-degree corner, and U-turn from was 0.63±0.03 mm to 0.48±0.03 mm and 0.98±0.04 mm to 0.82±0.03 mm, respectively. This reduction in bulging resulted in an overall error reduction in 25-40% geometric features. Using the unique geometric definitions of the corrected geometric features a test part had the same two FECC corrections repeatedly applied throughout the part to save on processing time. With only two unique FECC corrections, the test part's bulging corners and edges were corrected, and a noticeable improvement in part quality resulted.

In the future, this process can be used to generate a library of corrected geometric features that can be applied to DIW parts without the need for lengthy simulation with the CM model. Additionally, this paper's work only focused on correcting the tool paths in the extrusion dimension for DIW. The authors expect controlling only the extrusion limits the total improvement due to the nonlinearity of transient fluid flow. Further research can be done to explore new motion control strategies for the DIW system's Cartesian tool path that synchronize with the extrusion tool paths, resulting in DIW systems that can increase their deposition rates without sacrificing quality.

Chapter 5. Major Contributions and Future Work

5.1. Major Contributions

Overall, this dissertation has contributed in three major ways: (1) AM can be used to improve the performance of static mixers, (2) CM modeling can be used to accurately characterize the transient behavior of DIW AM with static mixers, and (3) FECC can efficiently improve the quality of DIW parts. This research will improve the quality of DIW AM and enable the technology to be faster and more efficient.

This dissertation investigated the modeling and control transient fluid flow with mixing in DIW. The three studies covered are: (1) Pressure Drop Reduction of an Impeller Spiral Static Mixer Design Enabled by Additive Manufacturing, (2) Modeling of Transient Fluid Flow in Direct Ink Write Additive Manufacturing using the Characteristic Method, and (3) Feedforward Error Compensation Control of Direct Ink Writing Additive Manufacturing using the Characteristic Method.

In the Pressure Drop Reduction of an Impeller Spiral Static Mixer Design Enabled by Additive Manufacturing study, Chapter 2, a new SSM design to improve efficiency using AM was discussed. The ISSM reduced the pressure drop within the static mixer up to 18.2% compared to a standard SSM design. The key features of the ISSM design are taper inlet, release winglet, and the transfer angle created by the α, β, and γ angles inspired by centrifugal pump impellers. The taper inlet adds a sharp angle to the SSM helix edge, promotes the recombination of fluid flows at helix transition reducing regions of low fluid velocity. The release winglets

reduce drag by making the transition between each SSM helix more gradual. The transfer angle adds a sharp edge to the SSM helix reducing losses associated with the blunt edge of the SSM helix. This behavior was validated with both CFD models and experimental validation for five configurations of ISSM. All CFD analysis was done using Fluent^{TM} (v19.1) VOF multi-phase flow simulation and rheological data from a two-part alkoxysilicone data. The experimental analysis was performed using a progressive cavity pump and the same two-part alkoxysilicone with pressure sensors to measure experimental conditions for comparison with the CFD data. The results of this study are a more efficient SSM with CFD validated behavior.

The Modeling of Transient Fluid Flow in Direct Ink Write Additive Manufacturing using the Characteristic Method study in Chapter 2 developed a generalized model for deposition in DIW. The CM model characterized a DIW system's deposition for simple tool paths using new frictional models for non-Newtonian fluid, ISSM, and a tapered nozzle. The CM model's transient modeling is validated through transient response testing. Using a doppler volumetric flow sensor and two pressure sensors, the transient fluid flow and pressure is recorded and compared to the CM model, resulting in a strong agreement between experimental and model data. The CM model is also used to predict the size of the corner for a 90-degree turn created by a DIW system. The CM model was applied to a tool path for a 90-degree corner with an acceleration of 100, 250, 500, 1000, 1500, and 2000 mm/s^2. Measuring the same tool paths created on a DIW machine the size of the corner ranged from 0.76 to 0.37 mm for a line width of 0.25 mm and a height of 0.15 mm, which matched predictions from the CM model. The result of this study is that CM is an accurate process model for transient flow in a DIW system.

The last study of this dissertation is the Feedforward Error Compensation Control of Direct Ink Writing Additive Manufacturing using the Characteristic Method, Chapter 4, which uses feed

forward control to improve the quality of DIW parts. Using the validated CM model from Chapter 3, this study created the FECC process to simulate and correct for errors in DIW tool paths. The FECC process combines the CM model, machine learning, and iLQR to create modified extrusion tool paths that reduce the error between desired and actual output flow rate as measured by 2-norm error. For examples, FECC was applied to two toolpaths, a 90-degree corner and a U-turn, both tool paths were shown to have significant 2-norm error, 0.32 and 0.43 mL/min respectively. With FECC the 2-norm error for the 90-degree corner and U-turn was reduced to 0.16 and 0.18 mL/min respectively. Experimentally this 2-norm error reduction results in a 90-degree corner that has a bulge that has a diameter of 0.63±0.03 mm without FECC and a diameter of 0.48±0.03 mm with FECC. The U-turn's width was reduced from 0.98±0.04 mm to 0.82±0.03 mm with FECC as well. The FECC process was applied to a test part that had 5000 90-degree turns and 8500 U-turns, resulting in significant reductions in corner bulging, material build up, and gaps on the test part. This study demonstrates how FECC can be used to correct for errors in DIW deposition and be applied to improve part quality.

5.2. Future work

Future work in the development control of DIW will be controlling the system kinematics and the deposition together. This dissertation only focused on controlling the deposition of material in DIW by trying to match it with system kinematics using iLQR, a mathematically optimal controller. While significant quality improvements resulted from this approach, there are limits to how responsive the transient flow during DIW can be and adjustments to system kinematics are needed to reduce the error even further. The CM model can be used as a foundation for creating tool paths that respect both the transient deposition and kinematic limits of the DIW system, enabling faster DIW AM speeds.

Other research areas that can be established from this work involve further research into AM of static mixers and the CM model. The ISSM configurations tested in Chapter 2 were unoptimized and the optimal parameters for α, β, and γ were not found. Additionally, there is likely other modifications that can be made to static mixer designs that are now possible with AM that can be explored to improve both pressure drop and mixing length. The CM model used in this dissertation was used only for a DIW system that used a PDP which controls volumetric flow rate. However, other common DIW systems use pressure control instead. To adjust the CM model to the pressure-controlled system only a change in the boundary conditions is needed but could be worth exploring to see if new insights into system behavior can be determined. Another adjustment that can be made to the CM model is include curing kinetics that cause the rheological properties to change with time. The CM model as implemented in this dissertation assumed that the alkoxysilicone's properties were constant, which was acceptable for this system because the working time for the material was approximately 45 min and the expected dwell time of material in the system was approximately 1 min. In future work materials with faster curing kinetics could be used in DIW which will require additional considerations in the CM model.

Long term this dissertation could be the basis for new techniques for improving the speed of DIW so that the process can be comparable with plastic extrusion (FFF). Currently DIW is an about two order of magnitudes slower than the fastest FFF machines. With an understanding of transient deposition, it will be possible to quickly catch up. Additionally, in the future it could be possible to tailor materials with specific material properties, such as high acoustic wave speeds and extreme shear thinning, that improve their transient deposition for DIW.

Appendix A. Acoustic Wave Speed

A typical simplifying assumption for fluid dynamics is to assume that the flow is non-compressible, defined as the fluid density does not change with pressure [75]. The non-dimensional number used to determine if compressibility can be ignored in fluid flows is the Mach number, Equation (A.1), and if the Mach number is smaller than 0.2, the fluid can be considered incompressible [75].

$$Mach = \frac{Q}{Aa} \tag{A.1}$$

For DIW, the Mach number is on the order of 10^{-4}, so compression can be ignored in the DIW fluid models. However, some compression still occurs in the form of acoustic waves [100]. Acoustic waves adiabatically compress and/or decompress fluids at the speed of a and the existence of a is why fluid flows exhibit transients [101].

One way to determine the a for a fluid is to measure it directly using acoustic spectroscopy, which was done for this study [102,103]. However, acoustic spectroscopy can require the use of specialized equipment, so an alternative calculation using bulk modulus, K, which can be measured using a piston in a universal testing machine, is given below [100,104]

$$a = \sqrt{\frac{K}{\rho\left[1 + \left(K/E_y\right)\varphi\right]}} \tag{A.2}$$

where E_y is the Young's modulus of the pipe wall, and φ is the pipe parameter that adjusts for pipe wall thickness, e. The φ for a rigid pipe, Equation (A.3), a thin wall pipe fixed at one end, Equation (A.4), and a thin wall pipe with both ends fixed, Equation (A.5), can be seen as:

$$\varphi = 0 \tag{A.3}$$

$$\varphi = \frac{D}{e}(1 - \nu^2) \tag{A.4}$$

$$\varphi = \frac{D}{e}(1 - 0.5\nu) \tag{A.5}$$

where ν is the Poisson's ratio of the pipe wall.

Bibliography

[1] H.E. Quinlan, T. Hasan, J. Jaddou, A.J. Hart, Industrial and Consumer Uses of Additive Manufacturing: A Discussion of Capabilities, Trajectories, and Challenges, J. Ind. Ecol. 21 (2017) S15–S20. doi:10.1111/jiec.12609.

[2] A. 52900:2015, Standard Terminology for Additive Manufacturing – General Principles – Terminology, ASTM Int. i (2015) 1–9. doi:10.1520/F2792-12A.2.

[3] J.A. Lewis, G.M. Gratson, Direct writing in three dimensions, Mater. Today. 7 (2004) 32–39. doi:10.1016/S1369-7021(04)00344-X.

[4] E. Feilden, C. Ferraro, Q. Zhang, E. García-Tuñón, E. D'Elia, F. Giuliani, L. Vandeperre, E. Saiz, 3D Printing Bioinspired Ceramic Composites, Sci. Rep. 7 (2017) 1–9. doi:10.1038/s41598-017-14236-9.

[5] A. Corker, H.C.H. Ng, R.J. Poole, E. García-Tuñón, 3D printing with 2D colloids: Designing rheology protocols to predict "printability" of soft-materials, Soft Matter. 15 (2019) 1444–1456. doi:10.1039/c8sm01936c.

[6] S. V. Murphy, A. Atala, 3D bioprinting of tissues and organs, Nat. Biotechnol. 32 (2014) 773–785. doi:10.1038/nbt.2958.

[7] Y. Jin, J. Plott, A.J. Shih, Extrusion-based additive manufacturing of the moisture-cured silicone elastomer, Proc. Solid Free. Fabr. Symp. (2015) 308–318. doi:10.1017/CBO9781107415324.004.

[8] L. Hao, D. Tang, T. Sun, W. Xiong, Z. Feng, K.E. Evans, Y. Li, Direct Ink Writing of

Mineral Materials: A review, Int. J. Precis. Eng. Manuf. - Green Technol. (2020). doi:10.1007/s40684-020-00222-6.

[9] A.S. Wu, W. Small, T.M. Bryson, E. Cheng, T.R. Metz, S.E. Schulze, E.B. Duoss, T.S. Wilson, 3D Printed Silicones with Shape Memory, Sci. Rep. 7 (2017) 1–6. doi:10.1038/s41598-017-04663-z.

[10] J. Go, S.N. Schiffres, A.G. Stevens, A.J. Hart, Rate limits of additive manufacturing by fused filament fabrication and guidelines for high-throughput system design, Addit. Manuf. 16 (2017) 1–11. doi:10.1016/j.addma.2017.03.007.

[11] B.D. Dixon, J. Kazalski, F. Murch, S. Marongelli, Practical Issues Concerning Dispensing End Effectors, Circuits Assem. (1997) 36–40.

[12] P. Chesser, B. Post, A. Roschli, C. Carnal, R. Lind, M. Borish, L. Love, Extrusion control for high quality printing on Big Area Additive Manufacturing (BAAM)systems, Addit. Manuf. 28 (2019) 445–455. doi:10.1016/j.addma.2019.05.020.

[13] B. Thompson, H. Yoon, Additive Manufacturing Systems, 4 (2014) 1555–1563.

[14] R. Chella, orge Vjnals, Mixing of a two-phase fluid by cavity flow, Phys. Rev. E. 53 (1996) 3832–3840. https://journals.aps.org/pre/pdf/10.1103/PhysRevE.53.3832 (accessed August 1, 2019).

[15] V.G. Rocha, E. Saiz, I.S. Tirichenko, E. García-Tuñón, Direct ink writing advances in multi-material structures for a sustainable future, J. Mater. Chem. A. 8 (2020) 15646–15657. doi:10.1039/d0ta04181e.

[16] H. Yuk, X. Zhao, A New 3D Printing Strategy by Harnessing Deformation, Instability, and Fracture of Viscoelastic Inks, Adv. Mater. 30 (2018) 1–8. doi:10.1002/adma.201704028.

[17] S. Hong, D. Sycks, H.F. Chan, S. Lin, G.P. Lopez, F. Guilak, K.W. Leong, X. Zhao, 3D Printing of Highly Stretchable and Tough Hydrogels into Complex, Cellularized Structures, Adv. Mater. 27 (2015) 4035–4040. doi:10.1002/adma.201501099.

[18] A. Sydney Gladman, E.A. Matsumoto, R.G. Nuzzo, L. Mahadevan, J.A. Lewis, Biomimetic 4D printing, Nat. Mater. 15 (2016) 413–418. doi:10.1038/nmat4544.

[19] D.B. Kolesky, K.A. Homan, M.A. Skylar-Scott, J.A. Lewis, Three-dimensional bioprinting of thick vascularized tissues, Proc. Natl. Acad. Sci. U. S. A. 113 (2016) 3179–3184. doi:10.1073/pnas.1521342113.

[20] J. Plott, X. Tian, A. Shih, Measurement and Modeling of Forces in Extrusion-Based Additive Manufacturing of Flexible Silicone Elastomer With Thin Wall Structures, J. Manuf. Sci. Eng. 140 (2018) 091009. doi:10.1115/1.4040350.

[21] J.A. Lewis, Direct ink writing of 3D functional materials, Adv. Funct. Mater. 16 (2006) 2193–2204. doi:10.1002/adfm.200600434.

[22] D.J. Hoelzle, A.G. Alleyne, A.J. Wagoner Johnson, Micro-robotic deposition guidelines by a design of experiments approach to maximize fabrication reliability for the bone scaffold application, Acta Biomater. 4 (2008) 897–912. doi:10.1016/j.actbio.2008.02.018.

[23] J. Bałdyga, R. Pohorecki, 14th European Conference on Mixing Editorial, Chem. Eng. Res. Des. 91 (2013) 2071–2072. doi:10.1016/j.cherd.2013.10.021.

[24] E.L. Paul, V.A. Atiemo-Obeng, S.M. Kresta, Handbook of industrial mixing : science and practice, Wiley-Interscience, 2004.

[25] A. Ghanem, T. Lemenand, D. Della Valle, H. Peerhossaini, Static mixers: Mechanisms, applications, and characterization methods - A review, Chem. Eng. Res. Des. 92 (2014) 205–228. doi:10.1016/j.cherd.2013.07.013.

[26] R.K. Thakur, C. Vial, K.D.P. Nigam, E.B. Nauman, G. Djelveh, Static Mixers in the Process Industries—A Review, Chem. Eng. Res. Des. 81 (2003) 787–826. doi:10.1205/026387603322302968.

[27] J.C. Godfrey, Static mixers, in: Mix. Process Ind., Elsevier, 1992: pp. 225–249. doi:10.1016/b978-075063760-2/50033-0.

[28] W.L. Wilkinson, M.J. Cliff, An Investigation into the Performance of a Static In-Line Mixer, in: Second Eur. Conf. Mix., Cambridge, England, England, 1977.

[29] N.I. Heywood, L.J. Viney, I.W. Stewart, Mixing Efficiencies and Energy Requirements of Various Motionless Mixer Designs for Laminar Mixing Applications, in: IChemE Symp. Ser. No.89, Elsevier, Bradford UK, 1984: pp. 147–176. doi:10.1016/b978-0-85295-171-2.50013-x.

[30] J. [Sbreve]IR, Z. Lecjaks, Pressure drop and homogenization efficiency of a motionless mixer, Chem. Eng. Commun. 16 (1982) 325–334. doi:10.1080/00986448208911104.

[31] N.F.N. Shah, D.D. Kale, Pressure drop for laminar flow of non-Newtonian fluids in static mixers, Chem. Eng. Sci. 46 (1991) 2159–2161. doi:10.1016/0009-2509(91)80175-X.

[32] H.-S.S. Song, S.P. Han, A general correlation for pressure drop in a Kenics static mixer, Chem. Eng. Sci. 60 (2005) 5696–5704. doi:10.1016/j.ces.2005.04.084.

[33] H.E.H. Meijer, M.K. Singh, P.D. Anderson, On the performance of static mixers: A quantitative comparison, Prog. Polym. Sci. 37 (2012) 1333–1349. doi:10.1016/j.progpolymsci.2011.12.004.

[34] A. Bakker, R.D. Laroche, E.M. Marshall, Laminar Flow in Static Mixers with Helical Elements, Online CFM B. (2000) 1–11. http://www.bakker.org/cfm. (accessed July 4, 2019).

[35] S. Armbruster, O. Cheong, J. Lölsberg, S. Popovic, S. Yüce, Fouling mitigation in tubular membranes by 3D-printed turbulence promoters, J. Memb. Sci. 554 (2018) 156–163. doi:10.1016/j.memsci.2018.02.015.

[36] H. Murasiewicz, Z. Jaworski, Transient CFD simulations of turbulent liquid - Liquid flow in a Kenics static mixer. Radial and tangential velocities, Polish J. Chem. Technol. 11 (2009) 36–40. doi:10.2478/v10026-009-0021-2.

[37] A. Mahammedi, H. Ameur, A. Ariss, Numerical investigation of the performance of Kenics static mixers for the agitation of shear thinning fluids, J. Appl. Fluid Mech. 10 (2017) 989–999. doi:10.18869/acadpub.jafm.73.240.27314.

[38] D.M. Hobbs, F.J. Muzzio, Optimization of a static mixer using dynamical systems techniques, Chem. Eng. Sci. 53 (1998) 3199–3213. doi:10.1016/S0009-2509(98)00115-8.

[39] W. Cheng, J. Huang, J. Chen, Computational fluid dynamics simulation of mixing characteristics and light regime in tubular photobioreactors with novel static mixers, J. Chem. Technol. Biotechnol. 91 (2016) 327–335. doi:10.1002/jctb.4560.

[40] S. Soman, Study of effects of design modification in static mixer geometry and its applications, University of Waterloo, 2016. https://uwspace.uwaterloo.ca/bitstream/handle/10012/10802/Soman_Sudhanshu.pdf (accessed July 4, 2019).

[41] C. Zhang, A.R. Ferrell, K. Nandakumar, Study of a toroidal-helical pipe as an innovative static mixer in laminar flows, Chem. Eng. J. 359 (2019) 446–458. doi:10.1016/J.CEJ.2018.11.048.

[42] X. Li, F. Jiang, A.V. Ravindra, J. Zhou, A. Zhou, T. Le, J. Peng, S. Ju, Mixing processes in a 3D printed large-flow microstructured reactor: Finite element simulations and

experimental study, Chem. Eng. J. 370 (2019) 295–304. doi:10.1016/J.CEJ.2019.03.187.

[43] X. Nguyen, A. Carafa, C.H. Hornung, Process Intensification Hydrogenation of vinyl acetate using a continuous flow tubular reactor with catalytic static mixers, Chem. Eng. Process. Process Intensif. 124 (2018) 215–221. doi:10.1016/j.cep.2017.12.007.

[44] A. Bellini, S. Güçeri, M. Bertoldi, S. Gü, M. Bertoldi, Liquefier dynamics in fused deposition, J. Manuf. Sci. Eng. 126 (2004) 237–246. doi:10.1115/1.1688377.

[45] R. Comminal, M.P. Serdeczny, D.B. Pedersen, J. Spangenberg, Numerical modeling of the strand deposition flow in extrusion-based additive manufacturing, Addit. Manuf. 20 (2018) 68–76. doi:10.1016/j.addma.2017.12.013.

[46] D.S. Ertay, A. Yuen, Y. Altintas, D. Sera, A. Yuen, Y. Altintas, Synchronized material deposition rate control with path velocity on fused filament fabrication machines, Addit. Manuf. 19 (2018) 205–213. doi:10.1016/j.addma.2017.05.011.

[47] D.J. Hoelzle, A.G. Alleyne, A.J. Wagoner Johnson, Iterative learning control for robotic deposition using machine vision, Proc. Am. Control Conf. (2008) 4541–4547. doi:10.1109/ACC.2008.4587211.

[48] D.J. Hoelzle, S.R. Svientek, A.G. Alleyne, A.J. Wagoner Johnson, Design and manufacture of combinatorial calcium phosphate bone scaffolds, J. Biomech. Eng. 133 (2011) 1–8. doi:10.1115/1.4005173.

[49] M. Li, L. Tang, R.G. Landers, M.C. Leu, Extrusion process modeling for aqueous-based ceramic pastes-part 1: Constitutive model, J. Manuf. Sci. Eng. Trans. ASME. 135 (2013) 1–7. doi:10.1115/1.4025014.

[50] M. Li, L. Tang, R.G. Landers, M.C. Leu, Extrusion process modeling for aqueous-based ceramic pastes, part 2: Experimental verification, J. Manuf. Sci. Eng. Trans. ASME. 135

(2013) 1–7. doi:10.1115/1.4025015.

[51] A. Simeunović, D.J. Hoelzle, Nonlinear and linearized gray box models of direct-write printing dynamics, Rapid Prototyp. J. (2020). doi:10.1108/RPJ-12-2018-0303.

[52] X.B. Chen, G. Schoenau, W.J. Zhang, On the Flow Rate Dynamics in Time-Pressure Dispensing Processes, Trans. ASME. 124 (2002) 693–698. doi:10.1115/1.1514056.

[53] S.Z. Liu, J.Y. Peng, Y.B. Zhang, X.B. Chen, Modeling Rotary-Screw-Driven Dispensing Systems for Electronics Packaging, 4 (2014) 1359–1365.

[54] A. Razban, B.L. Davies, Analytical modelling of the automated dispensing of adhesive materials, J. Adhes. Sci. Technol. 9 (1995) 1435–1450. doi:10.1163/156856195X00112.

[55] X.B.B. Chen, J.G.G. Pharoah, B.W.W. Surgenor, Theoretical investigation into the performance of the positive-displacement dispensing process, in: 2003 ASME Int. Mech. Eng. Congr., Washington D.C., 2003: pp. 1–7. doi:10.1115/IMECE2003-42739.

[56] X.B. Chen, J. Kai, Modeling of Positive-Displacement Fluid Dispensing Processes, 27 (2004) 157–163.

[57] T.J. Hinton, Q. Jallerat, R.N. Palchesko, J.H. Park, M.S. Grodzicki, H.J. Shue, M.H. Ramadan, A.R. Hudson, A.W. Feinberg, Three-dimensional printing of complex biological structures by freeform reversible embedding of suspended hydrogels, Sci. Adv. 1 (2015). doi:10.1126/sciadv.1500758.

[58] German RepRap's Surprise: Silicone 3D Printing, Fabbaloo. (2017). https://www.fabbaloo.com/blog/2017/2/14/german-repraps-surprise-silicone-3d-printing (accessed April 24, 2019).

[59] R.K. Jensen, J.K. Larsen, K.L. Lassen, M. Mandø, A. Andreasen, Implementation and validation of a free open source 1D water hammer code, Fluids. 3 (2018) 1–49.

doi:10.3390/fluids3030064.

[60] A.S. Tijsseling, A. Anderson, The Joukowsky equation for fluids and solids, n.d. https://www.win.tue.nl/analysis/reports/rana06-08.pdf (accessed July 20, 2019).

[61] D.A. Mcinnis, A. Tb, D.H. Axworthy, M.S. Ghidaoui, M. Zhao, D.A. Mcinnis, D.H. Axworthy, A review of water hammer theory and practice, Appl. Mech. Rev. 58 (2005) 49–75. doi:10.1115/1.1828050.

[62] S. Zheng, M. Zlatin, P.R. Selvaganapathy, M.A. Brook, Multiple modulus silicone elastomers using 3D extrusion printing of low viscosity inks, (2018). doi:10.1016/j.addma.2018.09.011.

[63] S.C. Ligon, R. Liska, J. Stampfl, M. Gurr, R. Mülhaupt, Polymers for 3D Printing and Customized Additive Manufacturing, Chem. Rev. 117 (2017) 10212–10290. doi:10.1021/acs.chemrev.7b00074.

[64] L. Liu, S. Tian, D. Xue, T. Zhang, Y.Q. Chen, Industrial feedforward control technology: a review, J. Intell. Manuf. 30 (2019) 2819–2833. doi:10.1007/s10845-018-1399-6.

[65] S. Mokhatab, W.A. Poe, Process Control Fundamentals, in: Handb. Nat. Gas Transm. Process., 2012: pp. 473–509. doi:10.1016/b978-0-12-386914-2.00014-5.

[66] G.C. Goodwin, S.F. Graebe, M.E. Salgado, Control System Design, Prentice Hall, Upper Saddle River, N.J., 2001.

[67] Q. Wang, P. Pan, A.R. Nassar, E. Irwin, Y. Ren, C.B. Stutzman, Model-based feedforward control of laser powder bed fusion additive manufacturing, Addit. 34 (2020). doi:10.1016/j.addma.2019.100985.

[68] C.L. Druzgalski, A. Ashby, G. Guss, W.E. King, T.T. Roehling, M.J. Matthews, Process optimization of complex geometries using feed forward control for laser powder bed

fusion additive manufacturing, Addit. Manuf. 34 (2020) 101169. doi:10.1016/j.addma.2020.101169.

[69] S.A. Khairallah, A.A. Martin, J.R.I. Lee, G. Guss, N.P. Calta, J.A. Hammons, M.H. Nielsen, K. Chaput, E. Schwalbach, M.N. Shah, M.G. Chapman, T.M. Willey, A.M. Rubenchik, A.T. Anderson, Y.M. Wang, M.J. Matthews, W.E. King, Controlling interdependent meso-nanosecond dynamics and defect generation in metal 3D printing, 665 (2020) 660–665.

[70] W. Han, M.A. Jafari, S.C. Danforth, A. Safari, Tool path-based deposition planning in fused deposition processes, J. Manuf. Sci. Eng. Trans. ASME. 124 (2002) 462–472. doi:10.1115/1.1455026.

[71] R. Comminal, M.P. Serdeczny, D.B. Pedersen, J. Spangenberg, Numerical modeling of the material deposition and contouring precision in fused deposition modeling, in: Solid Free. Fabr. Symp., 2018: pp. 1855–1864. http://sffsymposium.engr.utexas.edu/sites/default/files/2018/NumericalModelingoftheMaterialDepositionand.pdf (accessed March 1, 2019).

[72] J.R. Broussard, M.J. O'brien, Feedforward Control to Track the Output of a Forced Model, IEEE Trans. Automat. Contr. 25 (1980) 851–853. doi:10.1109/TAC.1980.1102409.

[73] R.F. Fox, Construction of the Jordan basis for the Baker map, Chaos. 7 (1997) 254–269. doi:10.1063/1.166226.

[74] A. Jaya, K. Kolmetz, STATIC MIXER (ENGINEERING DESIGN GUIDELIN), KLM Technol. Gr. (2014).

[75] F. White, Fluid Mechanics, 7th ed., ata Mcgraw Hill Education, 2011.

[76] K. Aruna Prabha, P. Sai Rohit, S.C. Nitturi, B. Nithin, Manufacturing of 3 D Shrouded Impeller of a Centrifugal Compressor on 3D-Printing machine using FDM Technology, IOP Conf. Ser. Mater. Sci. Eng. 1012 (2021) 012039. doi:10.1088/1757-899x/1012/1/012039.

[77] ANSYS, ANSYS Meshing User's Guide, Canonsburg, PA, 2010.

[78] ANSYS, ANSYS Fluent User's Guide, Canonsburg, PA, 2013.

[79] J.F. Lea, H. V. Nickens, M.R. Wells, Progressing Cavity Pumps, in: Well Prod. Pract. Handb., 2008: pp. 383–403. doi:10.1016/b978-075068280-0.50014-7.

[80] Miniature Low Pressure Sensors 24PC Series, Uncompensated/Unamplified, 0.5 psi to 250 psi, (n.d.). https://sensing.honeywell.com/honeywell-sensing-board-mount-24pc-series-miniature-low-pressure-sensors-product-sheet-32302909-a-en.pdf (accessed June 17, 2019).

[81] M.H. Chaudhry, Applied Hydraulic Transients, 3rd ed., Springer, 2014. https://link.springer.com/content/pdf/10.1007%2F978-1-4614-8538-4.pdf%0Ahttps://drive.google.com/open?id=0ByoalPrGoNQvOG1VaUF0eENkV28&authuser=0.

[82] A.K. Mitra, W.T. Rouleau, Radial and axial variations in transient pressure waves transmitted through liquid transmission lines, J. Fluids Eng. Trans. ASME. 107 (1985) 105–111. doi:10.1115/1.3242479.

[83] A.R. Halliwell, Halliwell Velocity of a Waterhammer Wave in an Elastic Pipe, J. Hydraul. Div. 89 (1963) 1–21.

[84] M. Hildner, A. Shih, Pressure drop reduction of an impeller spiral static mixer design enabled by additive manufacturing, Manuscr. Submitt. Publ. (2020).

[85] H. Prashanth Reddy, W.F. Silva-Araya, M. Hanif Chaudhry, Estimation of Decay Coefficients for Unsteady Friction for Instantaneous, Acceleration-Based Models, J. Hydraul. Eng. 138 (2012) 260–271. doi:10.1061/(ASCE)HY.1943-7900.0000508.

[86] I. Moyer, CoreXY, (2012). http://corexy.com/theory.html.

[87] A.R. Avdeev, A.A. Shvets, I.S. Torubarov, Investigation of Kinematics of 3D Printer Print Head Moving Systems, Lect. Notes Mech. Eng. (2020) 461–471. doi:10.1007/978-3-030-22041-9_50.

[88] K.M.C. Tj, E. Tj, The use of Gompertz models in growth analyses , and new Gompertz-model approach : An addition to the Unified-Richards family, (2017) 1–17.

[89] M.N. Gibbs, D.J.C. Mackay, Variational Gaussian Process Classi ers, IEEE Trans. Neural Networks. (1997) 1–12.

[90] R. Comminal, M.P. Serdeczny, D.B. Pedersen, J. Spangenberg, Motion planning and numerical simulation of material deposition at corners in extrusion additive manufacturing, Addit. Manuf. 29 (2019) 100753. doi:10.1016/j.addma.2019.06.005.

[91] Marlin, What is Marlin? | Marlin Firmware, (n.d.). http://marlinfw.org/docs/basics/introduction.html (accessed May 1, 2019).

[92] I. Gibson, D. Rosen, B. Stucker, Additive Manufacturing Technologies: 3D Printing, Rapid Prototyping, and Direct Digital Manufacturing, Springer, 2015. doi:10.1007/978-1-4939-2113-3.

[93] K.M. Lynch, F.C. Park, K.M. Lynch, F.C. Park, Modern Robotics: Mechanics, Planning, and Control [Bookshelf], 2019. doi:10.1109/MCS.2019.2937265.

[94] M. Hildner, J. Lorenz, A.J. Shih, Modeling of Transient Fluid Flow in Direct Ink Writing Additive Manufacturing using the Characteristic Method, Submitt. Publ. (n.d.).

[95] W. Li, E. Todorov, Iterative Linear Quadratic Regulator Design for Nonlinear Biological Movement Systems, (2011) 222–229. doi:10.5220/0001143902220229.

[96] Yuval, iLQG/DDP trajectory optimization, MATLAB Cent. File Exch. (n.d.). Yuval (2021). iLQG/DDP trajectory optimization (https://www.mathworks.com/matlabcentral/fileexchange/52069-ilqg-ddp-trajectory-optimization), MATLAB Central File Exchange. Retrieved January 26, 2021. (accessed January 25, 2021).

[97] D. Ding, Z. Pan, D. Cuiuri, H. Li, S. van Duin, Advanced Design for Additive Manufacturing: 3D Slicing and 2D Path Planning, in: New Trends 3D Print., InTech, 2016. doi:10.5772/63042.

[98] Yuval, iLQG/DDP trajectory optimization, MATLAB Cent. File Exch. (n.d.).

[99] P. Lancaster, M. Tismenetsky, The Theory of Matrices: With Applications, 2nd ed., Academic Press, 1985.

[100] M.H. Chaudhry, Applied Hydraulic Transients, n.d.

[101] D. Ferras, P.A. Manso, A.J. Schleiss, D.I.C. Covas, One-dimensional fluid-structure Interaction models in pressurized fluid-filled pipes: A review, Appl. Sci. 8 (2018) 1–33. doi:10.3390/app8101844.

[102] G. Bonacucina, D.R. Perinelli, M. Cespi, L. Casettari, R. Cossi, P. Blasi, G.F. Palmieri, Acoustic spectroscopy: A powerful analytical method for the pharmaceutical field?, Int. J. Pharm. 503 (2016) 174–195. doi:10.1016/j.ijpharm.2016.03.009.

[103] J. Yu, E. Kojima, J. Yu, Methods for Measuring the Speed of Sound in the Flu Fluid Transmission Pipes, SAE Trans. Sect. 2 J. Commer. Veh. 109 (2000) 358–366.

[104] H. Yang, B. Feng, G. Gong, Measurement of effective fluid bulk modulus in hydraulic

system, J. Dyn. Syst. Meas. Control. Trans. ASME. 133 (2011) 4–9.

doi:10.1115/1.4004783.